

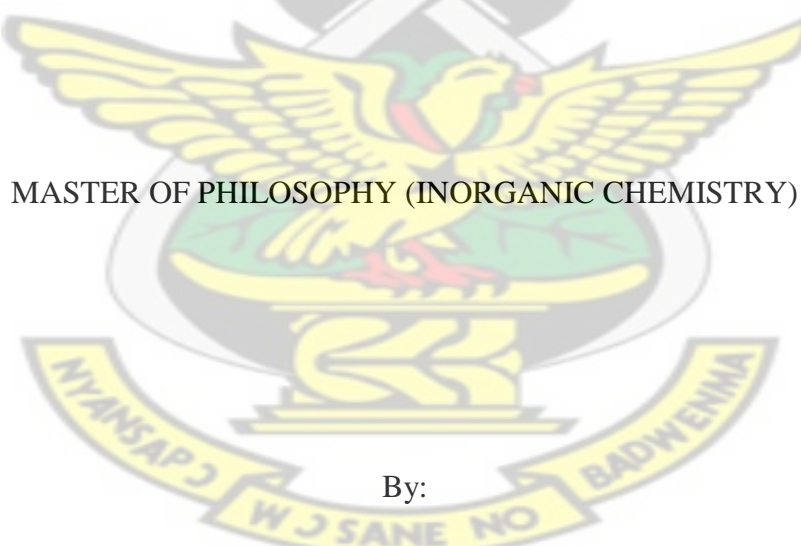
**DENSITY FUNCTIONAL THEORY STUDY OF THE GAS PHASE DECOMPOSITION  
OF SINGLE-SOURCE PRECURSORS FOR THE CHEMICAL VAPOUR DEPOSITION  
OF BINARY AND TERNARY METAL CHALCOGENIDES**

KNUST

A thesis submitted to the Department of Chemistry, College of Science, Kwame Nkrumah

University of Science and Technology, Kumasi

in partial fulfillment of the requirements for the degree of



MASTER OF PHILOSOPHY (INORGANIC CHEMISTRY)

By:

Francis Opoku, B.Sc. (Hons.)

July, 2013

CERTIFICATION

I hereby declare that this thesis is my own work towards the M.Phil. and that, to the best of my knowledge and belief, it contains no materials that has been accepted for the award of any other degree in any educational institution nor material previously published or written by another person, except where due acknowledgement has been made in the text.

KNUST

Francis Opoku (PG6148111)

Student Name and ID

.....

Signature

Date

Certified by:

Prof. Anthony A. Adimado

.....

Supervisor's Name

Signature

Date

Certified by:

Dr. Noah K. Asare-Donkor

.....

Co-supervisor's Name

Signature

Date

Certified by:

Dr. Ray Bright Voegborlo

.....

Head of Department, Chemistry

Signature

Date

## DEDICATION

To my brother, Gyamfi Eric

# KNUST



## ACKNOWLEDGEMENT

First of all, I would like to express my profound gratitude and thanks to the Almighty God for His divine grace, guidance, protection and provision that has seen me through this period of study and research.

My sincere thanks go to my supervisors, Prof. Anthony A. Adimado and Dr. Noah K. Asare-Donkor, not only for their patient and guidance, but also for their encouragement and support throughout my research.

I also express my sincere thanks to Dr. Evans Adei, for all the timely advice and constructive criticisms and contributions during the presentations.

I also would like to thank Dr. Richard Tia for providing helpful suggestions.

I would like to extend my gratitude to Jacob Amevor and all members of the group, for their friendship, encouragement and discussions.

Finally I would like to thank my family and, to Gloria Awuah for their unconditional love and support, all the other family members and all my friends, for their encouragement.

## SUMMARY

Chemical vapour deposition (CVD) method has been widely exploited to grow high quality thin films of metal chalcogenides. However, in some processes the formation of thin films in the gas phase at higher temperature can be a major obstacle to decreasing the deposition rate, thus the thin films formation reaction can compete with the surface deposition reaction and consume the gas phase reactants, before the vapour reaches the heated substrate surface. A variety of single source precursors have been developed for the deposition of thin films. However, few single source precursors have deposited good quality thin films. Hence it is important to design and develop single source precursors with appropriate physico-chemical properties. In this work, a series of novel metal (Pb, Zn, Cd) complexes of diphenyl- and diisopropyl-thioselenophosphate were studied. These organometallic complexes were employed as potential single source precursors for the deposition of metal chalcogenides thin films. Metal chalcogenides thin films have potential applications in photovoltaics, solar cells, microelectronics, displays and opto-electronic devices. Density functional theory (DFT) calculations have been shown to be valuable tools for elucidating the various decomposition processes of single source precursors and thus making their development more effective and less costly. The reaction mechanisms involved in the thermal decomposition of the precursors were explored by computing the activation barriers and reaction energies at the density functional theory MO6/LACVP\* level of theory.

This thesis is made up of the following chapters:

1. Chapter one presents a general introduction on metal chalcogenides, chemical vapour deposition process, single-source precursors and applications of metal chalcogenides.

Literature reports about thin films and their applications, and methods of fabrication of thin films are also presented.

2. Chapter two gives the general introduction on computational chemistry. The molecular mechanics method, semi empirical methods and *ab initio* methods are also discussed in addition to the hybrid methods and basis sets.
3. Chapters three to six describe the density functional theory at the MO6/LACVP\* level of theory for the thermal decompositions of  $\text{Pb}[(\text{C}_6\text{H}_5)_2\text{PSSe}]_2$ ,  $\text{Pb}[(^i\text{Pr})_2\text{PSSe}]_2$ ,  $\text{Zn}[(^i\text{Pr})_2\text{PSSe}]_2$  and  $\text{Cd}[(^i\text{Pr})_2\text{PSSe}]_2$  single-source precursors for the chemical vapour deposition of binary and ternary metal chalcogenides.
4. Chapter seven gives a general conclusion and recommendation for future studies.

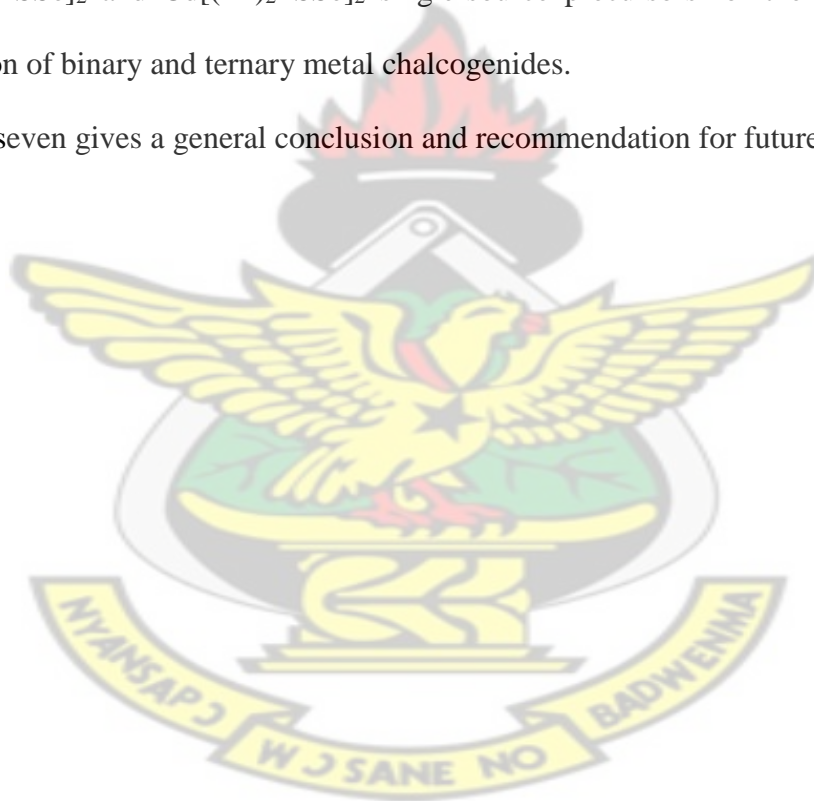


## TABLE OF CONTENTS

CERTIFICATION .....	i
DEDICATION .....	ii
ACKNOWLEDGEMENT .....	iii
SUMMARY .....	iv
LIST OF FIGURES .....	ix
LIST OF TABLES .....	xiii
LIST OF SCHEMES .....	xiv
LIST OF ABBREVIATIONS .....	xv
<b>CHAPTER ONE: GENERAL INTRODUCTION</b> .....	1
1.1 Introduction .....	1
1.2 Problem statement .....	3
1.3 Objectives .....	4
1.4 Justifications .....	4
1.5 Inorganic materials .....	5
1.5.1 Thin film technology .....	5
1.5.2 Fabrication of thin film semiconductor materials .....	5
1.5.3 Chemical vapour deposition (CVD) .....	6
1.5.3.1 Types of chemical vapour deposition .....	6
1.5.3.2 The process of chemical vapour deposition .....	8
1.5.4 Thin-Film Applications .....	9
1.5.5 Precursors for chemical vapour deposition .....	11
1.5.6 Issues in using conventional precursors for CVD .....	12
1.5.7 Advantages of single source precursors .....	12
References .....	14
<b>CHAPTER TWO: LITERATURE REVIEW ON THEORETICAL CHEMISTRY</b> .....	18
2.1 Introduction .....	18
2.1.1 Molecular Mechanics Method .....	20
2.1.2 Semi Empirical Methods .....	20
2.1.3 <i>Ab Initio</i> Methods .....	21
2.1.4 Density Functional Theory .....	21
2.1.5 Hartree-Fock theory .....	23
2.1.6 Hybrid Methods .....	23
2.1.7 Basis Sets .....	24
References .....	26
<b>CHAPTER THREE: DENSITY FUNCTIONAL THEORY (DFT) STUDY OF THE DECOMPOSITION OF Pb[(C<sub>6</sub>H<sub>5</sub>)<sub>2</sub>PSSe]<sub>2</sub> SINGLE-SOURCE PRECURSOR FOR THE CHEMICAL VAPOUR DEPOSITION OF BINARY AND TERNARY LEAD CHALCOGENIDES</b> .....	29
3.1 Introduction .....	29
3.2 Details of calculations .....	33

3.3 Mechanistic considerations .....	38
3.4 Results and discussion .....	39
3.4.1 Optimized Geometry of $\text{Pb}[(\text{C}_6\text{H}_5)_2\text{PSSe}]_2$ precursor .....	39
3.4.2 Overall Decomposition of $\text{Pb}[(\text{C}_6\text{H}_5)_2\text{PSSe}]_2$ precursor .....	41
3.5 Conclusion .....	59
References .....	61

**CHAPTER FOUR: DENSITY FUNCTIONAL THEORY (DFT) STUDY OF THE DECOMPOSITION OF  $\text{Pb}[(^i\text{Pr})_2\text{PSSe}]_2$  SINGLE-SOURCE PRECURSOR FOR THE CHEMICAL VAPOUR DEPOSITION OF BINARY AND TERNARY LEAD CHALCOGENIDES .....**

4.1 Introduction .....	66
4.2 Details of calculations .....	67
4.3 Mechanistic considerations .....	67
4.4 Results and Discussion .....	71
4.4.1 Optimized Geometry of $\text{Pb}[(^i\text{Pr})_2\text{PSSe}]_2$ precursor .....	71
4.4.2 Overall Decomposition of $\text{Pb}[(^i\text{Pr})_2\text{PSSe}]_2$ precursor .....	73
4.5 Conclusion .....	90
References .....	92

**CHAPTER FIVE: DENSITY FUNCTIONAL THEORY (DFT) STUDY OF THE DECOMPOSITION OF  $\text{Zn}[(^i\text{Pr})_2\text{PSSe}]_2$  SINGLE-SOURCE PRECURSOR FOR THE CHEMICAL VAPOUR DEPOSITION OF BINARY AND TERNARY ZINC CHALCOGENIDES .....**

5.1 Introduction .....	94
5.2 Details of calculations .....	95
5.3 Mechanistic considerations .....	95
5.4 Results and discussion .....	99
5.4.1 Optimized Geometry of $\text{Zn}[(^i\text{Pr})_2\text{PSSe}]_2$ precursors .....	99
5.4.2: Overall Decomposition of $\text{Zn}[(^i\text{Pr})_2\text{PSSe}]_2$ precursor .....	100
5.5 Conclusion .....	117
References .....	119

**CHAPTER SIX: DENSITY FUNCTIONAL THEORY (DFT) STUDY OF THE DECOMPOSITION OF  $\text{Cd}[(^i\text{Pr})_2\text{PSSe}]_2$  SINGLE-SOURCE PRECURSOR FOR THE CHEMICAL VAPOUR DEPOSITION OF BINARY AND TERNARY CADMIUM CHALCOGENIDES .....**

6.1 Introduction .....	121
6.2 Details of calculations .....	122
6.4 Results and discussion .....	127
6.4.1 Optimized Geometry of $\text{Cd}[(^i\text{Pr})_2\text{PSSe}]_2$ precursor .....	127
6.4.2 Overall Decomposition of $\text{Cd}[(^i\text{Pr})_2\text{PSSe}]_2$ precursor .....	128
6.5 Conclusion .....	145
References .....	147

**CHAPTER SEVEN: Conclusion and Recommendation** ..... 149  
7.1 Conclusion ..... 149  
7.2 Recommendation ..... 151

# KNUST



## LIST OF FIGURES

### Chapter one

Figure 1.1: Schematic representation of the basic steps in Chemical Vapour Deposition process 8

Figure 1.2: Some common ligands used to prepare single-source precursor ..... 13

### Chapter three

Figure 3.1: Optimized geometry of..... 40

Figure 3.2: Energetics of the unimolecular decomposition pathway (1, 2) at 298.15 K. The relative free energies are in kcal/mol and bond distances in Å..... 44

Figure 3.3: Energetics of the unimolecular decomposition pathway (1, 2) at 800 K. The relative free energies are in kcal/mol and bond distances in Å..... 45

Figure 3.4: Optimized geometrical parameters of the main stationary points involved in the unimolecular decomposition pathway (1, 2). Bond distances in Å and bond angles in degrees ..... 46

Figure 3.5: Energetics of the unimolecular decomposition pathway (3, 4) at 298.15 K. The relative free energies are in kcal/mol and bond distances in Å..... 49

Figure 3.6: Energetics of the unimolecular decomposition pathway (3, 4) at 800 K. The relative free energies are in kcal/mol and bond distances in Å..... 50

Figure 3.7: Optimized geometrical parameters of the main stationary points involved in the unimolecular decomposition pathway (3, 4). Bond distances in Å and bond angles in degrees ..... 51

Figure 3.8: Energetics of the unimolecular decomposition pathway (5, 6) at 298.15 K. The relative free energies are in kcal/mol and bond distances in Å..... 54

Figure 3.9: Energetics of the unimolecular decomposition pathway (5, 6) at 800 K. The relative free energies are in kcal/mol and bond distances in Å..... 55

Figure 3.10: Optimized geometrical parameters of the main stationary points involved in the unimolecular decomposition pathway (5, 6). Bond distances in Å and bond angles in degrees ..... 56

### Chapter four

Figure 4.1: Optimized geometry of  $\text{Pb}[(^1\text{Pr})_2\text{PSSe}]_2$  single-source precursor ..... 72

Figure 4.2: Energetics of the unimolecular decomposition pathway (1, 2) at 298.15 K. The relative free energies are in kcal/mol and bond distances in Å.....	76
Figure 4.3: Energetics of the unimolecular decomposition pathway (1, 2) at 800 K. The relative free energies are in kcal/mol and bond distances in Å.....	77
Figure 4.4: Optimized geometrical parameters of the main stationary points involved in the unimolecular decomposition pathway (1, 2). Bond distances in Å and bond angles in degrees .....	78
Figure 4.5: Energetics of the unimolecular decomposition pathway (3, 4) at 298.15 K. The relative free energies are in kcal/mol and bond distances in Å.....	81
Figure 4.6: Energetics of the unimolecular decomposition pathway (3, 4) at 800 K. The relative free energies are in kcal/mol and bond distances in Å.....	82
Figure 4.7: Optimized geometrical parameters of the main stationary points involved in the unimolecular decomposition pathway (3, 4). Bond distances in Å and bond angles in degrees .....	83
Figure 4.8: Energetics of the unimolecular decomposition pathway (5, 6) at 298.15 K. The relative free energies are in kcal/mol and bond distances in Å.....	86
Figure 4.9: Energetics of the unimolecular decomposition pathway (5, 6) at 800 K. The relative free energies are in kcal/mol and bond distances in Å.....	87
Figure 4.10: Optimized geometrical parameters of the main stationary points involved in the unimolecular decomposition pathway (5, 6). Bond distances in Å and bond angles in degrees .....	88

## Chapter five

Figure 5.1: Optimized geometry of Zn[( <sup>4</sup> Pr) <sub>2</sub> PSSe] <sub>2</sub> single-source precursor.....	99
Figure 5.2: Energetics of the unimolecular decomposition pathway (1, 2) at 298.15 K. The relative free energies are in kcal/mol and bond distances in Å.....	103
Figure 5.3: Energetics of the unimolecular decomposition pathway (1, 2) at 800 K. The relative free energies are in kcal/mol and bond distances in Å.....	104
Figure 5.4: Optimized geometrical parameters of the main stationary points involved in the unimolecular decomposition pathway (1, 2). Bond distances in Å and bond angles in degrees .....	105
Figure 5.5: Energetics of the unimolecular decomposition pathway (3, 4) at 298.15 K. The relative free energies are in kcal/mol and bond distances in Å.....	108

Figure 5.6: Energetics of the unimolecular decomposition pathway (3, 4) at 800 K. The relative free energies are in kcal/mol and bond distances in Å.....	109
Figure 5.7: Optimized geometrical parameters of the main stationary points involved in the unimolecular decomposition pathway (3, 4). Bond distances in Å and bond angles in degrees .....	110
Figure 5.8: Energetics of the unimolecular decomposition pathway (5, 6) at 298.15 K. The relative free energies are in kcal/mol and bond distances in Å.....	113
Figure 5.9: Energetics of the unimolecular decomposition pathway (5, 6) at 800 K. The relative free energies are in kcal/mol and bond distances in Å.....	114
Figure 5.10: Optimized geometrical parameters of the main stationary points involved in the unimolecular decomposition pathway (5, 6). Bond distances in Å and bond angles in degrees .....	115
 <b>Chapter six</b>	
Figure 6.1: Optimized geometry of [Cd{(iPr) <sub>2</sub> PSSe} <sub>2</sub> ] precursor .....	127
Figure 6.2: Energetics of the unimolecular decomposition pathway (1, 2) at 298.15 K. The relative free energies are in kcal/mol and bond distances in Å.....	131
Figure 6.3: Energetics of the unimolecular decomposition pathway (1, 2) at 800 K. The relative free energies are in kcal/mol and bond distances in Å.....	132
Figure 6.4: Optimized geometrical parameters of the main stationary points involved in the unimolecular decomposition pathway (1, 2). Bond distances in Å and bond angles in degrees .....	133
Figure 6.5: Energetics of the unimolecular decomposition pathway (3, 4) at 298.15 K. The relative free energies are in kcal/mol and bond distances in Å.....	136
Figure 6.6: Energetics of the unimolecular decomposition pathway (3, 4) at 800 K. The relative free energies are in kcal/mol and bond distances in Å.....	137
Figure 6.7: Optimized geometrical parameters of the main stationary points involved in the unimolecular decomposition pathway (3, 4). Bond distances in Å and bond angles in degrees .....	138
Figure 6.8: Energetics of the unimolecular decomposition pathway (5, 6) at 298.15 K. The relative free energies are in kcal/mol and bond distances in Å.....	141
Figure 6.9: Energetics of the unimolecular decomposition pathway (5, 6) at 800 K. The relative free energies are in kcal/mol and bond distances in Å.....	142

Figure 6.10: Optimized geometrical parameters of the main stationary points involved in the unimolecular decomposition pathway (3, 4). Bond distances in Å and bond angles in degrees ..... 143

KNUST

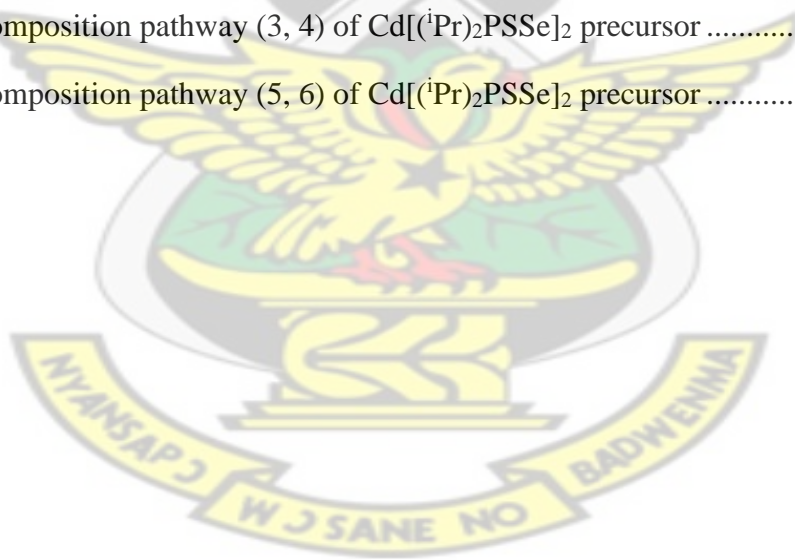


## LIST OF TABLES

Table 2.1: Comparison of theoretical methods .....	25
Table 3.1: Selected bond lengths (Å) and bond angles (°) of experimental and optimised (calculate) Pb[(C <sub>6</sub> H <sub>5</sub> ) <sub>2</sub> PSSe] <sub>2</sub> precursor.....	40
Figure 3.1: Optimized geometry of Pb[(C <sub>6</sub> H <sub>5</sub> ) <sub>2</sub> PSSe] <sub>2</sub> single-source precursor .....	40
Table 3.2: Calculated rate constants for selected individual steps in the decomposition of Pb[(C <sub>6</sub> H <sub>5</sub> ) <sub>2</sub> PSSe] <sub>2</sub> precursor both at room temperature (298.15 K) and at an elevated temperature (800 K).....	57
Table 3.3: Position of the transition state structures ( <i>n<sub>T</sub></i> ) for selected individual steps.....	58
Table 4.1: Selected bond lengths (Å) and bond angles (°) of Pb[( <sup>i</sup> Pr) <sub>2</sub> PSSe] <sub>2</sub> precursor .....	72
Table 4.2: Calculated rate constants for selected individual steps in the decomposition of Pb[( <sup>i</sup> Pr) <sub>2</sub> PSSe] <sub>2</sub> precursor both at room temperature (298.15 K) and at an elevated temperature (800 K).....	89
Table 4.3: Position of the transition state structures ( <i>n<sub>T</sub></i> ) for selected individual steps.....	90
Table 5.1: Selected bond lengths (Å) and bond angles (°) of Zn[( <sup>i</sup> Pr) <sub>2</sub> PSSe] <sub>2</sub> precursor .....	100
Table 5.2: Calculated rate constants for selected individual steps involve in the decomposition of Zn[( <sup>i</sup> Pr) <sub>2</sub> PSSe] <sub>2</sub> precursor at room temperature (298.15 K) and at an elevated temperature (800 K).....	116
Table 5.3: Position of the transition structures ( <i>n<sub>T</sub></i> ) for selected individual steps .....	117
Table 6.1: Selected bond lengths (Å) and bond angles (°) of [Cd{( <sup>i</sup> Pr) <sub>2</sub> PSSe} <sub>2</sub> ] precursor .....	128
Table 6.2: Calculated rate constants for selected individual steps in the decomposition of Cd[( <sup>i</sup> Pr) <sub>2</sub> PSSe] <sub>2</sub> precursor at room temperature (298.15 K) and at an elevated temperature (800 K).....	144
Table 6.3: Position of the transition structures ( <i>n<sub>T</sub></i> ) for selected individual steps .....	145

## LIST OF SCHEMES

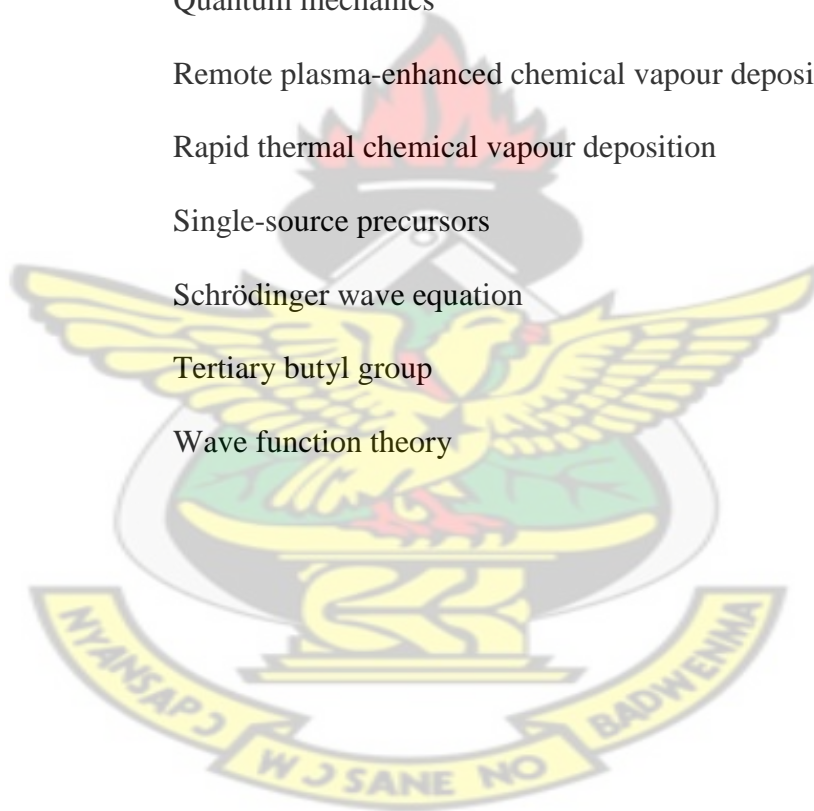
Scheme 3.1: Decomposition pathway (1, 2) of $\text{Pb}[(\text{C}_6\text{H}_5)_2\text{PSSe}]_2$ precursor.....	35
Scheme 3.2: Decomposition pathway (3, 4) of $\text{Pb}[(\text{C}_6\text{H}_5)_2\text{PSSe}]_2$ precursor.....	36
Scheme 3.3: Decomposition pathway (5, 6) of $\text{Pb}[(\text{C}_6\text{H}_5)_2\text{PSSe}]_2$ precursor.....	37
Scheme 4.1: Decomposition pathway (1, 2) of $\text{Pb}[(^i\text{Pr})_2\text{PSSe}]_2$ precursor.....	68
Scheme 4.2: Decomposition pathway (3, 4) of $\text{Pb}[(i\text{Pr})_2\text{PSSe}]_2$ precursor.....	69
Scheme 4.3: Decomposition pathway (5, 6) of $\text{Pb}[(^i\text{Pr})_2\text{PSSe}]_2$ precursor.....	70
Scheme 5.1: Decomposition pathway (1, 2) of $\text{Zn}[(^i\text{Pr})_2\text{PSSe}]_2$ precursor.....	96
Scheme 5.2: Decomposition pathway (3, 4) of $\text{Zn}[(i\text{Pr})_2\text{PSSe}]_2$ precursor.....	97
Scheme 5.3: Decomposition pathway (5, 6) of $\text{Zn}[(^i\text{Pr})_2\text{PSSe}]_2$ precursor.....	98
Scheme 6.1: Decomposition pathway (1, 2) of $\text{Cd}[(^i\text{Pr})_2\text{PSSe}]_2$ precursor.....	124
Scheme 6.2: Decomposition pathway (3, 4) of $\text{Cd}[(^i\text{Pr})_2\text{PSSe}]_2$ precursor.....	125
Scheme 6.3: Decomposition pathway (5, 6) of $\text{Cd}[(^i\text{Pr})_2\text{PSSe}]_2$ precursor.....	126



## LIST OF ABBREVIATIONS

AACVD	Aerosol assisted chemical vapour deposition
ALCVD	Atomic layer chemical vapour deposition
ALD	Atomic layer deposition
APCVD	Atmospheric pressure chemical vapour deposition
Bu	Butyl group
CVD	Chemical vapour deposition
DFT	Density functional theory
DLICVD	Direct liquid injection chemical vapour deposition
ECD	Electro chemical deposition
ECP	Effective core potential
Et	Ethyl group
GGA	Generalized gradient approximation
HF	Hartree Fock
HPCVD	Hybrid physical chemical vapour deposition
HWCVD	Hot wire chemical vapour deposition
<sup>i</sup> Bu	Isobutyl group
<sup>i</sup> Pr	Isopropyl group
LDA	Local density approximation
LEDs	Light-emitting diodes
LPCVD	Low-pressure chemical vapour deposition
MBE	Molecular beam epitaxy
Me	Methyl group

MM	Molecular mechanics
MOCVD	Metal-organic chemical vapour deposition
ONIOM	Our n-layered integrated molecular orbital + molecular mechanics
PECVD	Plasma-enhanced chemical vapour deposition
PES	Potential energy surface
Ph	Phenyl group
PVD	Physical vapour deposition
QM	Quantum mechanics
RPECVD	Remote plasma-enhanced chemical vapour deposition
RTCVD	Rapid thermal chemical vapour deposition
SSPs	Single-source precursors
SWE	Schrödinger wave equation
t-Bu	Tertiary butyl group
WFT	Wave function theory



## CHAPTER ONE

### 1. GENERAL INTRODUCTION

In this chapter, the general introduction on metal chalcogenides, chemical vapour deposition process, single-source precursors and applications of metal chalcogenides is described. Literature reports about thin films and their applications, and methods of fabrication of thin films is also presented.

KNUST

#### 1.1 Introduction

For many years metal-organic compounds are extensively been used as molecular precursors for the chemical vapour deposition process (CVD). The success of this technique is mainly due to its versatility and the increasing interest for the low temperature deposition processes. Correlatively, the increasing demand of various thin film materials for new industrial applications is also a substantial reason for the rapid development of CVD.

Quantum mechanical calculations are useful to provide thermodynamic and kinetic data of possible molecules involved. Using statistical methods to average over large systems can provide estimates of thermodynamic quantities such as reaction free energy. Additionally, activation free energies can be obtained and most probable reaction pathways located. Through this theoretical studies, the precursor design strategy can be explored prior to experiment or in conjunction with nominal preliminary screening of precursors.

There is considerable current interest in metal chalcogenides (sulphides, selenides or tellurides) stemming from their useful properties as thin films or in highly dispersed form (Afzaal and O'Brien, 2006). Potential applications of these materials are in devices such as solar cells (II–

VI and III–VI), infrared detectors (IV–VI) and in room-temperature thermoelectric generators (V–VI). Binary transition and main group metal chalcogenides, of the formulae ME or ME<sub>2</sub> (E = S, Se or Te), have varied technological uses and the most extensive use of metal chalcogenides stems from their wide range of semi-conducting properties (Lopez and Ortiz, 1994). Metal chalcogenides, in general, are isolated as non-volatile, insoluble or sparingly soluble oligomeric species, therefore limiting their utility as molecular precursors. Lead and cadmium chalcogenide compounds have been the focus of a significant number of investigations for various types of applications.

The synthesis of novel metal-molecular precursors to deposit binary (O'Brien *et al.*, 2003) or ternary alloys (Shahid *et al.*, 2009) of inorganic materials with critical dimensions of the order of nanometers have received considerable attention in the last three decades. To date, a large number of molecular precursors have been synthesized and used to grow metal sulphide, selenide, and telluride materials (Malik *et al.*, 2010). Metal dithiocarbamates and xanthates are the most commonly used single-source precursors for thin films and nanoparticles (Clark *et al.*, 2011).

Many potential single-molecular precursors have been described in the literature and were originally intended for use in the growth of semiconductor thin films from CVD techniques, but proved problematic because of their low volatility and lack of stoichiometric control. Some compounds used by others include the preparation of II-V nanoparticles of Cd<sub>3</sub>P<sub>2</sub> from [MeCdP(<sup>t</sup>Bu)<sub>2</sub>]<sub>3</sub> (O'Brien and Green, 1998; Green and O'Brien, 1999). Onicha *et al.* (2012) used bis(imido(selenodiisopropylphosphinato) lead(II)) [Pb((SePiPr<sub>2</sub>)<sub>2</sub>N)<sub>2</sub>] and bis(diethyldithiocarbamato) lead(II) [Pb(S<sub>2</sub>CNEt<sub>2</sub>)<sub>2</sub>] as single source precursors for the growth of

ternary  $\text{PbSe}_x\text{S}_{1-x}$  (where  $x = 0.23, 0.39, 0.49, 0.68, 0.90$ ) as well as binary PbSe and PbS nanowires (NWs).

A series of metal precursor of bis(di-alkylselenophosphinyl)selenide  $[(\text{R}_2\text{PSe}_2)\text{-Se}]$  with the general formula  $[\text{M}(\text{R}_2\text{PSe}_2)_n]$  ( $\text{M} = \text{Zn, Cd, Pb, In, Ga, Cu, Bi, Ni}$ ;  $\text{R} = \text{iPr, Ph}$ ) and  $[\text{MoV}_2\text{O}_2\text{Se}_2(\text{Se}_2\text{-P}^i\text{Pr}_2)_2]$  have subsequently been synthesized and used for the deposition of metal selenide thin films by the CVD method (Hagihara and Watanabe, 1968; Zhu *et al.*, 2002). Other classes of molecule, which have proved useful for the deposition of thin films, include coordination precursor such as dialkyl dichalcogenocarbamates or dithiophosphinates (Byrom *et al.*, 2000; Hurthouse *et al.*, 1992). Various groups have studied simple  $[\text{M}(\text{S}_2\text{CNET}_2)_2]$  ( $\text{M} = \text{Cd}^{\text{II}}, \text{Zn}^{\text{II}}$ ) precursor and deposited CdS or ZnS films by different deposition techniques (Motevalli *et al.*, 1996).

Relatively few single-source precursors have been used for deposition of metal sulphide films through CVD, including bis(diethyldithiocarbamate)zinc and cadmium precursor (Frigo *et al.*, 1989; Hursthouse *et al.*, 1992) and their alkyl substituted derivatives,  $[\text{RM}(\text{E}_2\text{CNET}_2)_2]$ , ( $\text{M} = \text{Zn, Cd}$ ;  $\text{E} = \text{S, Se}$ ;  $\text{R} = \text{Me, Et, t-Bu}$  and neopentyl) (Hursthouse *et al.*, 1991; Malik and O'Brien, 1991).

## 1.2 Problem statement

Although thermodynamic calculations are important in estimating the "chemical driving force", energy balance and relative stability of the intermediates and products of deposition, in most CVD processes occur at conditions which are far from thermodynamic equilibrium (Akhtar *et al.*, 2011). While the mechanism behind the decomposition of these single-source precursors is

not fully understood, their use empirically results in the growth of homogeneous thin films (Onicha *et al.*, 2012). The film structure and composition are governed by other factors: chemical kinetics, surface and gas diffusion and mass transfer. A better understanding of probable growth reactions will assist in the design of experiments.

### 1.3 Objectives

This work is primarily aimed at studying the mechanisms involved in the thermal decomposition of  $M[(R)_2PSSe]_2$  (Where  $M=Pb, Zn, Cd$ ;  $R=Ph, iPr$ ) single-source precursors for the chemical vapour deposition of binary and ternary metal chalcogenides. The geometries and relative free energies of the reactants, transition states, relevant intermediates and products at both room temperature (298.15 K) and elevated temperature (800 K) will be computed in order to provide insight into the design of experimental procedures for the efficient deposition of semiconductor thin films from single source-source precursors.

### 1.4 Justifications

The general interest in the thermal decomposition of single source precursors by means of depositing binary or ternary alloys of metal chalcogenides on the surface has prompted a lot of study in this field.

An understanding of the detailed mechanistic pathways involved in the decomposition of single-source precursors to deposit ternary alloys will drastically increase the ability to design and fine tune material's composition rather than size and this gives researchers access to a new class of nanomaterials, possessing both size and composition dependent properties.

## 1.5 Inorganic materials

### 1.5.1 Thin film technology

The thin films technology has attracted much attention because of its unique size-dependent properties and applications in the optoelectronic devices, solar cells, sensors, and laser materials. Thin film and devices play an important role in the development of modern science. The thin film is a two dimensional form of solid material, whose one dimension, called the thickness, is much smaller than the other two dimensions. The thin film is formed by atom to atom or molecule to molecule condensation process. At the initial stages, investigations on the thin films were made out of scientific curiosity, particularly for their significantly different properties from those of the same material in bulk form. However the acquired capability of controlling properties of the thin films in subsequent years, helps immensely the use of thin films in electronic, optoelectronic and other devices and as a result, the electronic industry has become the greatest beneficiary of thin film technology. On the other hand, the thin film technology contributes to the development of microelectronics, by reducing the sizes of semiconductor devices to two dimensions. The use of thin films in making active and passive electronic components made it possible to produce VLSI and microcomputer. Because of compactness, better performance and reliability and low production cost thin film devices and components are preferred over their bulk counterparts.

### 1.5.2 Fabrication of thin film semiconductor materials

Semiconductor materials can be fabricated by various techniques which fall into four general categories: deposition, removal, patterning and modification of electrical properties.

Deposition: Deposition is a process that grows, coats or transfers a material onto the substrate: e.g, Physical Vapour Deposition (PVD), Chemical Vapour Deposition (CVD), Electro Chemical Deposition (ECD), Molecular Beam Epitaxy (MBE) and Atomic Layer Deposition (ALD).

Removal: The process that remove material from the wafer either in bulk or in selective form. These include etching and chemical-mechanical planarization among others.

Patterning: The series of processes that shape or alter the existing shape of deposited materials and are generally referred to as lithography.

Modification of electrical properties: The process consisting of doping transistor sources and drains originally by diffusion furnaces and later by ion implantation.

### 1.5.3 Chemical vapour deposition (CVD)

Chemical vapour deposition is a chemical process used to produce high purity and high performance thin film materials. In a typical CVD process the substrate is exposed to one or more volatile precursors which react and/or decompose on the substrate to produce the desired deposit.

#### 1.5.3.1 Types of chemical vapour deposition

A number of forms of CVD are in wide use and are frequently referenced. These processes differ in the means by which chemical reactions are initiated (activation process) and process condition. The types of CVD include:

Atmospheric pressure CVD (APCVD) - CVD process at atmospheric pressure.

Low-pressure CVD (LPCVD) - CVD process at sub-atmospheric pressures. Reduced pressure tends to reduce unwanted gas-phase reactions and improves film uniformity across the wafer.

Aerosol assisted CVD (AACVD) - CVD process in which the precursors are transported to the substrate by means of a liquid/gas aerosol, which can be generated ultrasonically. This technique is suitable for use with involatile precursors.

Direct liquid injection CVD (DLICVD) - CVD process in which the precursors are in liquid form. Liquid solutions are injected in a vapourization chamber towards reactors. Then the precursor vapours are transported to the substrate as in classical CVD process. This technique is suitable for use on liquid or solid precursors. High growth rates can be reached using this technique.

Plasma - Enhanced CVD (PECVD) - CVD process that utilizes plasma to enhance chemical reaction rates of the precursors. PECVD processing allows deposition at lower temperatures, which is often critical in the manufacture of semiconductors.

Remote plasma-enhanced CVD (RPECVD) - CVD process similar to PECVD except that the wafer substrate is not directly in the plasma discharge region. Removing the wafer from the plasma region allows processing temperatures down to room temperature.

Atomic layer CVD (ALCVD) - Deposits successive layers of different substances to produce layered crystalline films.

Hot wire CVD (HWCVD) - Also known as Catalytic CVD or hot filament CVD (HWCVD) uses a hot filament to chemically decompose the source gases.

Metal-organic chemical vapour deposition (MOCVD) - CVD process based on metal organic precursors.

Hybrid physical chemical vapour deposition (HPCVD) - Vapour deposition process, which involve chemical decomposition of precursor gas and vapourization of solid source.

Rapid thermal CVD (RTCVD) - CVD process that uses heating lamps or other methods to rapidly heat the wafer substrate. Heating only the substrate rather than the gas or chamber walls helps reduce unwanted gas phase reactions that can lead to particle formation.

### 1.5.3.2 The process of chemical vapour deposition

CVD processes are extremely complex and involve a series of gas phase and surface reactions. The basic steps in an overall CVD reaction are shown in Figure 1.1.

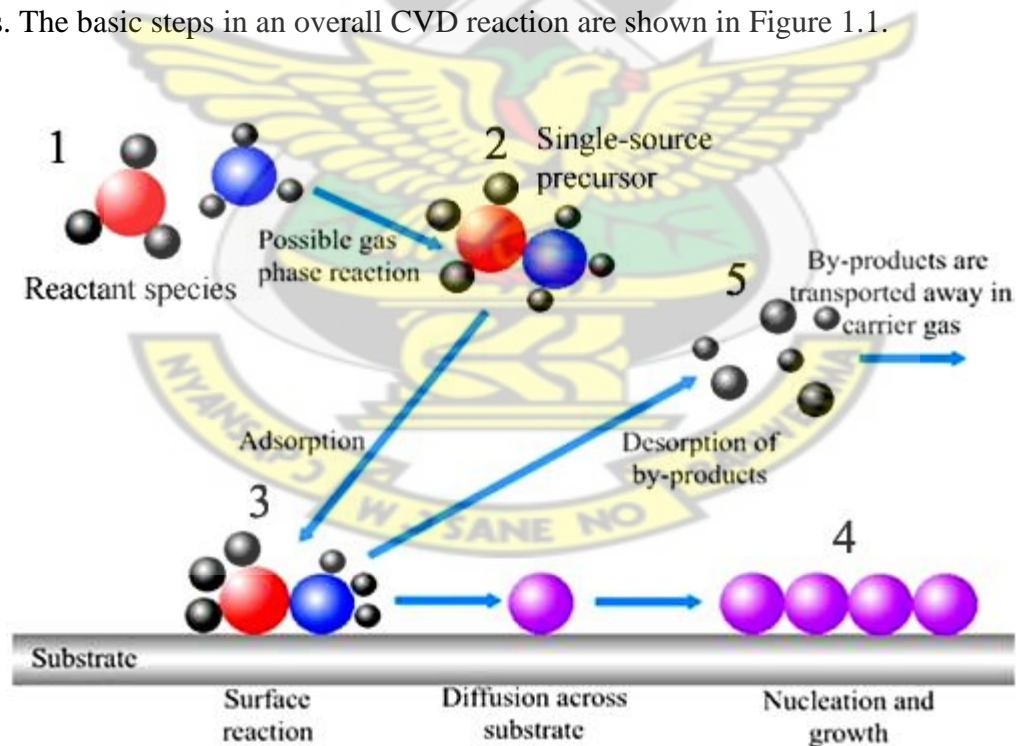


Figure 1.1: Schematic representation of the basic steps in Chemical Vapour Deposition process

Step 1: Generation of active gaseous reactant species and transport of the gaseous species into the reaction chamber.

Step 2: Gas phase reactions of precursors in the reaction zone to produce intermediates.

Step 3: Adsorption of gaseous reactants onto the heated substrate, and the heterogeneous reaction occurs at the gas–solid interface (i.e. heated substrate) which produces the deposit and by-product species.

Step 4: The deposits will diffuse along the heated substrate surface forming the crystallization centre and growth of the film.

Step 5: Mass transport of remaining fragments of the decomposition away from the reaction zone

#### 1.5.4 Thin-Film Applications

In considering the different applications of deposited thin films, the following generic categories can be identified.

**Electronic Components:** The fabrications of electronic components, especially solid-state devices and microelectronic integrated circuits, have undoubtedly found the widest and most demanding applications for thin film depositions. These films typically consist of semiconductor materials, dielectric and insulating materials, and metal or refractory metal silicide conductors.

**Electronic Displays:** Electronic displays are used for interfacing electronic equipment with human operators. Different components and device structures are required, such as: liquid-crystal displays, light-emitting diodes (LEDs), electroluminescent displays, plasma and fluorescent

displays, electrochromic displays. The fabrication of these displays requires transparent and conductive films, luminescent or fluorescent films as well as dielectric and insulating layers.

**Optical Coatings:** Optical coatings are applied for anti-reflection purposes, as interference filters on solar panels, as plate glass infrared solar reflectors, and for laser optics. In the fabrication of filter optics, thin films with refractive index gradients are deposited on preforms from which the optical fibers are drawn. These coatings require dielectric materials with precisely defined indices of refraction and absorption coefficients. Laser optics requires metal reflective coatings which can withstand high radiation intensities without degradation. Infrared reflecting coatings are applied to filament lamps to increase the luminous flux intensity.

**Magnetic Films for Data Storage:** Thin films of magnetic materials have found wide commercial applications for data storage in computers and control systems. The substrates can be metal, glass or plastic polymeric materials. Thin film deposition processes for magnetic materials and for materials with a high degree of hardness are required.

**Optical Data Storage Devices:** Thin films are finding increasing commercial use for optical data storage devices in compact disks and computer memory applications. Processes for the deposition of organic polymer materials as storage media and as protective overcoats are required for this technology.

**Antistatic Coatings:** Thin films of conductive or semiconductive materials are deposited to provide protection from electrostatic discharges.

**Hard Surface Coatings:** Thin film coatings of carbides, silicides, nitrides, and borides are finding increased uses to improve the wear characteristics of metal surfaces for tools, bearings, and

machine parts. Of particularly great current interest are films of diamond-like carbon because of this material's heat dissipation properties, electrical insulation, hardness, and resistance to high-temperature and high-energy radiation.

#### 1.5.5 Precursors for chemical vapour deposition

A major part of tailoring material properties resides in the proper choice of the molecular precursors, whose nature strongly affects the nature and morphology of the final product. It is most important to design the precursors that have a combination of certain characteristics that make them suitable precursor for preparation of high quality thin films. Single source approach involves the use of an organometallic or metal-organic molecule as a source for the elements required in the growth of the target compound at the desired stoichiometry (O'Brien and Nomura, 1995). Single-molecule precursor approach provides several key advantages over other routes (Arif *et al.*, 1988; Cowley and Jones, 1989). In CVD, the presence of only one precursor molecule in the supply stream reduces the likelihood of pre-reaction and the associated contamination of the deposited film and permits intrinsic control of film stoichiometry. Other advantages of CVD include growth of high purity films and the ability to fabricate abrupt junctions. The characteristics of an ideal CVD precursor can be explained as follows:

1. The main requirement of any precursor is that it should be readily volatile at a temperature well below that of its decomposition temperature.
2. Good thermal stability during evaporation and transport in the gas phase to avoid premature decomposition.
3. The precursors should be easily available and preparation should be cost effective.
4. Clean decomposition without the incorporation of residual impurities.

5. Compatibility with other precursors or solvents during the growth of complex materials.
6. Precursor should be non-toxic to reduce the environmental effects during the CVD process.

#### 1.5.6 Issues in using conventional precursors for CVD

The uses of conventional precursors for the CVD process involve some issues which include:

1. The highly pyrophoric nature of metal alkyls and the high toxicity of hydride gases such as  $\text{H}_2\text{S}$ ,  $\text{H}_2\text{Se}$ ,  $\text{NH}_3$ ,  $\text{PH}_3$ ,  $\text{AsH}_3$ ,  $\text{SiH}_4$  etc. In addition, the reactivity of the metal alkyls means that trace amounts of air and moisture may lead to the formation of alkoxides and result in the incorporation of oxygen impurities on the films
2. Prereactions within the reactant molecules in MOCVD reactor. Such reactions affect the morphology and stoichiometries of the final product
3. A large imbalance in the mole ratios of the precursors in the feed gas is usually needed with conventional precursors to control and maintain the stoichiometry of the thin films

#### 1.5.8 Advantages of single source precursors

The uses of single source precursors for the CVD process have advantages over the conventional precursors which are:

1. Single source is insensitive to air and moisture since synthesis are normally carried out under anaerobic conditions.
2. Use of single source precursors can minimise the use of toxic gases.
3. Prereactions may be limited.

4. Easy to maintain the stoichiometries of metal and ligand compositions by monitoring flow rates of precursors.
5. Low temperature deposition routes are possible.
6. It may also overcome the problem of incompatibility between the different precursors occasionally found in the conventional multiple source methods

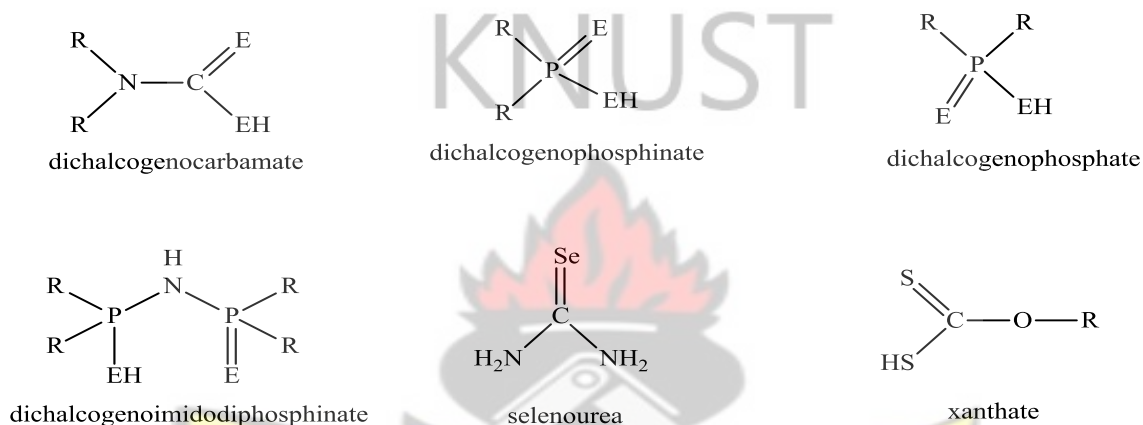


Figure 1.2: Some common ligands used to prepare single-source precursor

## References

- Afzaal, M. and O'Brien P. (2006). "Recent developments in II-VI and III-VI semiconductors and their applications in solar cells". *Journal of Materials Chemistry*, 16: 1597-1602.
- Akhtar, J., Afzaal, M., Vincent, M., Burton, N., Raftery, J., Hillier, I. and O'Brien, P. (2011). "Understanding the Decomposition Pathways of Mixed Sulphur/Selenium Lead Phosphinato Precursor Explaining the Formation of Lead Selenide". *J. Phys. Chem. C*, 115: 16904-16909.
- Arif, A. M., Benac, B. L., Cowley, A. H., Jones, R. A., Kidd, K. B. and Nunn, C. M. (1988). "Phosphido and Arsenido Derivatives of Aluminum, Gallium, and Indium: Synthesis of the Binary Compounds  $M(t\text{-Bu}_2\text{E})_3$ , (  $M = \text{Ga, In ; E = P, As}$  ) and the Homodinuclear Compounds  $[\text{Me}_2\text{M}(\mu\text{-}t\text{-Bu}_2\text{E})]_2$  (  $M = \text{Al, Ga, In ; E = P, As}$  )". *New J. Chem.*, 12: 553-557.
- Byrom, C., Malik, M. A., O'Brien, P. White, A. J. P. and Williams, D. J. (2000). "Synthesis and X-ray single crystal structures of bis(diisobutyldithiophosphinato) cadmium(II) or zinc(II): Potential single-source precursors for II/VI materials". *Polyhedron*, 19: 211-215.
- Clark, J. M., Kociok-Köhn, G., Harnett, N. J., Hill, M. S., Molloy, K. C., Saponia, H., Stanton, D. and Sudlow, A. J. (2011). "Formation of PbS materials from lead xanthate precursors". *Dalton Trans.*, 40: 6893-6900.

- Cowley, A. H. and Jones, R. A. (1989). "Single Source III/V Precursors: A New Approach to Gallium Arsenide and Related Semiconductors". *Angew. Chem., Int. Ed. Engl.*, 28(9): 1208-1215.
- Frigo, D. M., Khan, O. F. Z. and O'Brien, P. (1989). "Growth of epitaxial and highly oriented thin films of cadmium and cadmium zinc sulphide by low-pressure metal organic chemical vapour deposition using diethyldithiocarbamates". *J. Cryst. Growth*, 96: 989-992.
- Green, M. and O'Brien, P. (1999). "The synthesis of cadmium phosphide nanoparticles using cadmium diorganophosphide precursors". *J. Mater. Chem.*, 9: 243-247.
- Hagihara, H., Watanabe, Y. and Yamashita, S. (1968). The crystal structure of lead *n*-butylxanthate. I. Disordered structure. *Acta Cryst. B*, 24: 960.
- Hursthouse, M. B., Malik, M. A., Motevalli, M. and O'Brien, P. (1991). "The crystal and molecular structure of N,N-diethyldiselenocarbamatocadmium(II): cadmium and zinc diethyldiselenocarbamates as precursors for selenides". *Polyhedron*, 11: 45-48.
- Hursthouse, M. B., Malik, M. A., Motevalli, M. and O'Brien, P. (1992). "Mixed alkyl dialkylthiocarbamates of zinc and cadmium: potential precursors for II/VI materials. X-ray crystal structure of [MeZnS<sub>2</sub>CNEt<sub>2</sub>]<sub>2</sub>". *Organometallics*, 10: 730-732.
- Lopez, A. and Ortiz, A. (1994). "Spray pyrolysis deposition of Sn<sub>x</sub>S<sub>y</sub> thin films". *Semicond. Sci. Technol.*, 9: 2130-2133.
- Malik, M. A. and O'Brien, P. (1991). "Mixed methyl- and ethylzinc precursor with diethylselenocarbamate: Novel precursors for ZnSe". *Chem. Mater.*, 3: 999-1000.

- Malik, M. A., Afzaal, M. and O'Brien, P. (2010). "Precursor Chemistry for Main Group Elements in Semiconducting Materials". *Chem. Rev.*, 110: 4417-4446;
- Motevalli, M., O'Brien, P., Walsh, J. R., and Watson, I. M. (1996). "X-ray crystal structures and thermal behaviour of two volatile bis(1,1,1,5,5,5-hexafluoropentane-2,4-dionato)barium-(azapolyether) precursor". *Polyhedron*, 15: 2801-2808.
- O'Brien P. and Nomura R. (1995). "Single-molecule precursor chemistry for the deposition of chalcogenide (S or Se)-containing compound semiconductors by MOCVD and related methods. *J. Mater. Chem.*, 5: 1761-1773.
- O'Brien, P., Park, J. H. and Waters, J. (2003). "A single-source approach to deposition of nickel sulphide thin films by LP-MOCVD". *Thin Solid Films*, 502: 431-432.
- O'Brien, P. and Green, M. (1998). "A novel synthesis of cadmium phosphide nanoparticles using the single source precursor  $[\text{MeCdP}^t\text{Bu}_2]_3$ ". *Adv. Mater.*, 1998, 10: 527-528.
- Onicha, A. C., Petchsang, N., Kosel, T. H. and Kuno, M. (2012). "Controlled synthesis of compositionally tunable ternary  $\text{PbSe}_x\text{S}_{1-x}$  as well as binary  $\text{PbSe}$  and  $\text{PbS}$  nanowires". *ACS Nano.*, 6(3): 2833-2843.
- Shahid, M., Mazhar, M., Hamid, M., O'Brien, P., Malik, M., Helliwell, M. and Raftery, J. (2009). "Aerosol assisted chemical vapour deposition of Cu-ZnO composite from single source precursors". *Dalton Trans.*, 28: 5487-5494.

Zhu, J.-J., Wang, H., Xu, S. and Chen, H.-Y. (2002). “Sonochemical method for the preparation of monodisperse spherical and rectangular lead selenide nanoparticles”. *Langmuir*, 18: 3306-3310.

# KNUST



## CHAPTER TWO

### 2. LITERATURE REVIEW ON THEORETICAL CHEMISTRY

This Chapter gives the general introduction on computational chemistry. The molecular mechanics method, semi empirical methods and *ab initio* methods is discussed in addition to the hybrid methods and basis sets.

#### 2.1 Introduction

The application of quantum-mechanical principles to chemical problems has revolutionized the field of chemistry. Today our understanding of chemical bonding, spectral phenomena, molecular reactivities, and various other fundamental chemical problems rests heavily on our knowledge of the detailed behavior of electrons in atoms and molecules. Computational chemistry (molecular modeling) is the application of computer-based models to the simulation of chemical processes and the computation of chemical properties. The term computational chemistry is used when the mathematical method is sufficiently developed that it can be automated for implementation on a computer (Jensen, 2007; Helgaker *et al.*, 2000; Cramer, 2004; Leach, 2001). Computational chemistry is the application of chemical, mathematical and computing skills to the solution of interesting chemical problems. It uses computers to generate information such as properties of molecule or simulated experimental results (Tia, 2009).

Computational chemistry is critical in basic and applied molecular science research in areas which are relevant to the chemical, pharmaceutical, polymer and petroleum industries, and in nanotechnology and the environment. Molecular modelling methods are now routinely used to investigate the structure, dynamics and thermodynamics of inorganic, biological, and polymeric

systems, encompassing such areas as protein folding, enzyme catalysis, protein stability, conformational changes associated with biomolecular function, molecular recognition of proteins, DNA, membrane precursor, materials science and catalysis, and rational drug design (Tia, 2009).

The key to theoretical chemistry is molecular quantum mechanics. Soon after its formulation (Schrödinger, 1926), it became clear that solution of the time-independent Schrödinger equation

$$H(\mathbf{r}; \mathbf{R}) \Psi(\mathbf{r}; \mathbf{R}) = E(\mathbf{R}) \Psi(\mathbf{r}; \mathbf{R})$$

could, in principle, lead to direct quantitative prediction of most, if not all, chemical phenomena (Dirac, 1929; Lewis, 1933). In the above equation  $\Psi(\mathbf{r}; \mathbf{R})$  is the molecular wave function, which depends explicitly on the  $3N$  coordinates of all  $N$  electrons, and implicitly on the nuclear coordinates.  $E(\mathbf{R})$  is the molecular energy, which depends parametrically on the nuclear positions. Hence,  $E(\mathbf{R})$  defines the potential energy surface (PES) obtained from solution of the Schrödinger equation subject to the Born-Oppenheimer approximation.  $H(\mathbf{r}; \mathbf{R})$  is the molecular electronic Hamiltonian operator, subject to frozen nuclei, consisting of kinetic energy, electron-nuclear attraction, electron-electron repulsion and nuclear-nuclear repulsion terms. In atomic units,  $H$  has the explicit form

$$H(\mathbf{r}; \mathbf{R}) = -\frac{1}{2} \sum_i^n \left( \frac{\partial^2}{\partial x_i^2} + \frac{\partial^2}{\partial y_i^2} + \frac{\partial^2}{\partial z_i^2} \right) - \sum_i^n \sum_A^A \frac{Z_A}{|\mathbf{r}_i - \mathbf{R}_A|} + \frac{1}{2} \sum_i^n \sum_j^n \frac{1}{|\mathbf{r}_i - \mathbf{r}_j|} + \frac{1}{2} \sum_A^A \sum_B^A \frac{Z_A Z_B}{|\mathbf{R}_A - \mathbf{R}_B|}$$

Applying the principles of quantum mechanics to molecular properties is challenging in terms of exactly solving the Schrödinger wave equation (SWE). To solve the SWE approximately, various theoretical models have been developed. Understanding the strengths and weakness of

these methods is the key for applications on target molecule. Determining factors in the choice of method include the size of the molecule under study, and available computational resources (Tia, 2009).

### 2.1.1 Molecular Mechanics Method

In molecular mechanics methods, Newtonian mechanics (classical physics) is used to predict the structures and properties of molecules. Since the theory is not based on quantum mechanics, electrons are not treated explicitly in molecular mechanics. Molecular mechanics (MM) calculates properties of target species as a function of nuclear position (Leach, 1992). By neglecting the momentum and position of the electrons, the atoms' motion can be described by classical physics. These approximations make calculations with MM much faster and less expensive than quantum mechanics (QM) based methods.

In MM, parameters are precisely defined for each type of atom based on its hybridization and coordination number. Force field parameters are used to calculate the total energy of the molecule as a sum of bond stretching, bond torsion, angle bending, electrostatic, and van der Waals interactions.

### 2.1.2 Semi Empirical Methods

Semi empirical methods are quantum mechanical methods that use less number of parameters than MM methods. Moreover, Semi empirical methods consider only valence electrons and neglect many electron-electron interaction integrals deemed to be small in magnitude. Because of these reasons, Semi empirical methods are much faster than *ab initio* levels of theory (including

DFT), but slower than MM techniques. The expected computational trade-off is greater accuracy for Semi empirical versus MM techniques.

The PM3 (tm) method uses a minimal valence basis set of Slater type orbitals (Thiel and Voityuk, 1992). Initially, Stewart developed PM3 parameters for most elements except the transition metals (Stewart, 1992), and later the parameters were extended to transition metals and this method termed PM3(tm) (Hehre and Yu, 2002).

### 2.1.3 *Ab Initio* Methods

*Ab initio* electronic structure methods employ the laws of quantum mechanics to solve the Schrödinger wave equation. Although many mathematical approximations are applied, finding an exact solution for the SWE equation is computationally impossible for most systems. Hartree-Fock (HF) and Quantum Monte Carlo (QMC) are the two common wave-function based an ignition calculations. Density functional theory is another of *ab initio* calculation that is based on total electron density rather than wave functions.

### 2.1.4 Density Functional Theory

Density functional theory (DFT) describes the electronic states of atoms, molecules and materials in terms of the three dimensional electronic density of the system, which is a great simplification over wave function theory (WFT), which involves a 3N-dimensional antisymmetric wave function for a system with N electrons. In density functional theory (DFT), the total energy is expressed in terms of the total electron density, rather than the wave function. The theoretical foundations of DFT rest on the Hohenberg-Kohn theorem which establishes the existence of a one-to-one correlation between any ground state property of a molecule and its electron density

(Hohenberg and Kohn, 1964) and the Kohn-Sham equations which defines self-consistent equations that must be solved for a set of orbitals whose density is defined to be exactly that of the real system (Kohn and Sham, 1965). In this type of calculation, there is an approximate Hamiltonian and an approximate expression for the total electron density (Cramer and Truhlar, 2009; Young, 1998). Density functional theory (DFT) (Kohn *et al.*, 1996; Parr and Yang., 1989) is currently the most widely utilized approach in electronic structure theory of transition metals. Hohenberg and Kohn originally developed this theory (Hohenber, 1964). The applications and advantages of DFT methods are numerous (Kohn *et al.*, 1996; Parr and Yang., 1989). The accuracy achieved by DFT calculations is often comparable to more expensive post-Hartree-Fock methods. It depends on the system being studied and the functional. An LDA calculations will not come close to a coupled cluster calculations.

Although the DFT has many strengths and diverse applications, but DFT are limited by a number of short comings which in many cases lead to qualitatively incorrect predictions of chemical structure and reactivity. First, they under estimate the barriers of chemical reactions, the band gaps of materials, the energies of dissociating molecular ions, and charge transfer excitation energies. They also overestimate the binding energies of charge transfer complexes and the response to an electric field in molecules and materials. These entire diverse issues share the same root - the delocalization error of approximate functionals, due to the dominating Coulomb term that pushes electrons apart. This error can be understood from a perspective that invokes fractional charges. Furthermore, typical DFT calculations fail to describe degenerate or near-degenerate states, such as a rise in transition metal systems, the breaking of chemical bonds, and strongly correlated materials. All these problems are merely manifestations of another common error; the

static correlation error of approximate functionals. This problem arises because of the difficulty in using the electron density to describe the interaction of degenerate states and can be understood in another perspective; that of fractional spins (Cohen *et al.*, 2008).

#### 2.1.5 Hartree-Fock theory

Hartree-Fock theory is one of the simplest approximate theories for solving the many-body Hamiltonian. It is based on a simple approximation to the true many-body wavefunction: that the wavefunction is given by a single Slater determinant of  $N$  spin-orbitals. It is the basis of molecular orbital (MO) theory, which posits that each electron's motion can be described by a single-particle function (orbital) which does not depend explicitly on the instantaneous motions of the other electrons. Hartree-Fock theory often provides a good starting point for more elaborate theoretical methods which are better approximations to the electronic Schrödinger equation (e.g., many-body perturbation theory, single-reference configuration interaction).

#### 2.1.6 Hybrid Methods

Hybrid methods combine two or more disparate levels of theory, each applied to specific regions of the chemical species of interest. Bulky molecules with many atoms are investigated using QM/MM methods. The ONIOM (Svensson, 1996) (our n-layered integrated molecular orbital + molecular mechanics) QM/MM methodology are normally employed. The central transition metals, atoms attached to the metal, or atoms in conjugation with these are modeled with QM techniques. The remaining atoms in the precursor, typically far from the transition metal (or reaction centre), are treated with MM force fields.

### 2.1.7 Basis Sets

Basis sets are mathematical functions that describe the motion and position of electrons. In modern computational chemistry, quantum chemical calculations are typically performed with a finite set of basis functions, centered at each atomic nucleus within the molecule.

To make transition metal calculations less expensive, an approach whereby the core electrons are replaced by an average potential, the effective core potential (ECP) (Krauss and Stevens, 1984), has been utilized. Since the core electrons are minimally affected by changes in chemical bonding, ECPs reduce the number of electrons to be included in the calculations without sacrificing much chemical accuracy. Additionally, by replacing core electrons with an ECP, scalar relativistic effects can be incorporated by replacing the electrons with an analytical functions that would reasonably, accurately and much more represents the combined nuclear-electron core to the remaining valence electrons. The ECP-31G (Krauss and Stevens, 1984) valence basis set uses a double-zeta description for hydrogen and main group elements; single-zeta for outer core orbitals ( $ns$  and  $np$  orbitals) of a transition metal and is triple-zeta for the metal's valence orbitals (i.e.,  $nd$ ,  $(n+1)s$  and  $(n+1)p$  orbitals).

Table 2.1: Comparison of theoretical methods

Method Type	Features	Advantages	Disadvantages	Best for
Molecular Mechanics	<ul style="list-style-type: none"> <li>• Uses classical physics</li> <li>• Relies on force-field with embedded empirical parameters</li> <li>• Computationally least intensive-fast and useful with limited computer resources</li> <li>• Can be used for Molecules as large as enzymes</li> </ul>	<ul style="list-style-type: none"> <li>• Molecular Mechanics can be used to model very large system such DNA or proteins because the applications markedly simplify calculations.</li> </ul>	<ul style="list-style-type: none"> <li>• Particular force field, applicable only for a limited class of molecules</li> <li>• Does not calculate Electronic properties</li> <li>• Requires experimental data (or data from <i>ab initio</i> calculations)</li> </ul>	<ul style="list-style-type: none"> <li>• Large systems (~1000 of atoms)</li> <li>• Systems or processes with no breaking or forming of bonds</li> </ul>
Semi-Empirical	<ul style="list-style-type: none"> <li>• Uses quantum physics</li> <li>• Uses experimentally derived empirical parameters</li> <li>• Uses many approximation</li> </ul>	<ul style="list-style-type: none"> <li>• Less demanding computationally than <i>ab initio</i> methods</li> <li>• Capable of calculating transition states and excited states</li> </ul>	<ul style="list-style-type: none"> <li>• Requires experimental data (or data from <i>ab initio</i>) for parameters</li> <li>• Less rigorous than <i>ab initio</i> methods</li> </ul>	<ul style="list-style-type: none"> <li>• Medium-sized systems (hundreds of atoms)</li> <li>• Systems involving electronic transition</li> </ul>
<i>Ab Initio</i> (Hartre-Fock, Density functional theory and Quantum monte Carlo)	<ul style="list-style-type: none"> <li>• Uses quantum physics</li> <li>• Mathematically rigorous, no empirical parameters</li> <li>• Uses approximation extensively</li> </ul>	<ul style="list-style-type: none"> <li>• Useful for a broad range of systems</li> <li>• does not depend on experimental data</li> <li>• Capable of calculating transition states and excited states</li> </ul>	<ul style="list-style-type: none"> <li>• Computationally expensive</li> </ul>	<ul style="list-style-type: none"> <li>• Small systems (tens of atoms)</li> <li>• Systems involving electronic transition</li> <li>• Molecules without available experimental data</li> <li>• Systems requiring rigorous accuracy</li> </ul>

## References

- Cohen, A. J., Mori-Sanchez, P. and Yang, W. (2008). "Insights into current limitations of density functional theory". *Science*, 321: 792-794.
- Cramer, C. J. (2004). *Essentials of Computational Chemistry. Theories and Models*, 2nd ed.; John Willey and Sons, Ltd., Chichester.
- Dirac, P. A. M. (1929). "Quantum Mechanics of Many-Electron Systems". *Proc. Roy. Soc.*, 123: 714-733.
- Hehre, W. J. and Yu, J. (2002). *Book of Abstracts, 224th ACA National Meeting*, Boston, MA, August 18-22.
- Helgaker, T., Jørgensen, P. and Olsen, J. (2000). *Molecular Electronic-Structure Theory*; John Willey and Sons, Ltd., Chichester.
- Hohenberg, P. and Kohn, W. (1964). "Inhomogeneous Electron Gas". *Phys. Rev. B*, 136: 864-871.
- Jensen, F. (2007). *Introduction to Computational Chemistry*, 2nd ed., John Willey and Sons, Ltd., Chichester.
- Kohn, W., Becke, A. D., Oarr, R. G. (1996). "Density Functional Theory of Electronic Structure". *J. Phys. Chem.*, 100: 12974-12980.
- Krauss, M. and Stevens, W. (1984). "Effective core potentials and accurate energy curves for Cs<sub>2</sub> and other alkali diatomics". *J. Annu. Rev. Phys. Chem.*, 35: 357.

Leach, A. R. (1992). *Molecular modeling - Principles and Applications* Longman, Harlow, UK.

Thiel, W.; Voityuk, A. *Theor. Chim. Acta.*, 81: 391.

Leach, A. R. (2001). *Molecular Modelling. Principles and Applications*, 2nd ed., Prentice Hall, Harlow, England.

Lewis, G. N. (1933). "The Chemical Bond". *J. Chem. Phys.*, 1: 17-28.

Parr, R. G. and Yang, W. (1989). *Density functional theory of Atoms and Molecule*; Oxford: New York.

Schrödinger, E. (1926). "Quantisation as an eigenvalue problem (Part 1)". *Ann. Phys.*, 79: 361-376.

Stewart, J. J. P. (1989). "Optimization of parameters for semi-empirical methods I. Method". *J. Comput. Chem.*, 10(2): 209-220.

Svensson, M., Humbel, S., Froese, R. D. J., Matsubara, T., Sieber, S. and Morokuma, K. (1996). "ONIOM: a multilayered integrated MO + MM method for geometry optimizations and single point energy predictions. A test for Diels–Alder reactions and  $\text{Pt}(\text{P}(\text{t-Bu})_3)_2 + \text{H}_2$  oxidative addition". *J. Phys. Chem.*, 100: 19357-19363.

Thiel, W. and Voityuk, A. (1992). "Extension of the MNDO Formalism to d orbitals: Integral Approximations and Preliminary Numerical Results". *Theor. Chim. Acta.*, 81: 391-404.

Tia, R. (2009). Quantum mechanical studies of the mechanisms of some transition metal organometallic reactions. A thesis submitted to the Department of Chemistry, College of

Science, Kwame Nkrumah University of Science and Technology, Kumasi in partial fulfilment of the requirements for the degree of Doctor of Philosophy in Chemistry.

Young, D. (1998). "Introduction to Computational Chemistry". *Chem. Aust.*, 11: 5.

# KNUST



## CHAPTER THREE

# DENSITY FUNCTIONAL THEORY (DFT) STUDY OF THE DECOMPOSITION OF Pb[(C<sub>6</sub>H<sub>5</sub>)<sub>2</sub>PSSe]<sub>2</sub> SINGLE-SOURCE PRECURSOR FOR THE CHEMICAL VAPOUR DEPOSITION OF BINARY AND TERNARY LEAD CHALCOGENIDES

### Abstract

The reaction mechanisms involved in the thermal decomposition of Pb[(C<sub>6</sub>H<sub>5</sub>)<sub>2</sub>PSSe]<sub>2</sub> precursor have been explored by computing the activation barriers and reaction energies using the density functional theory at the MO6/LACVP\* level of theory. The results indicate that, the steps that lead to PbSe formation on the singlet potential energy surface is favoured kinetically and thermodynamically over those that lead to PbS and ternary PbSe<sub>x</sub>S<sub>1-x</sub> thin films. On the doublet PES, the steps that lead to PbSe formation are somewhat more favourable on kinetic grounds while the steps that lead to ternary PbSe<sub>x</sub>S<sub>1-x</sub> formation are somewhat more favourable on thermodynamic grounds. Density functional theory calculations of the formation of PbSe are consistent with a dominant role on kinetic and thermodynamic grounds in controlling the material formed during the deposition process.

**Keywords:** Precursor, density functional theory, thermal decomposition, thin films, deposition process

### 3.1 Introduction

The thermal decomposition of single-source precursors have been of considerable practical and theoretical interest. The homogeneous thermal decomposition of single-source precursors is

potentially important in the high temperature chemical vapour deposition (CVD) because it can produce reactive species that can contribute to film growth with much higher probability. However, the rate and dominant reaction pathway for the decomposition remain uncertain.

Lead(II) precursors with sulphur, selenium or tellurium donor atom ligands have been studied widely during the last few decades (Davidovich *et al.*, 2010). The reason for the sustained interest in these compounds lies in their significant structural diversity and potential for applications (Claudio *et al.*, 2003). Lead(II) can bind as few as two and as many as ten ligands, with preferred coordination numbers of four and six (Shimoni-Livny *et al.*, 1998). Lead(II) forms stable precursors with both soft and hard donor atom ligands. In similar coordination environments, the affinity of lead(II) towards sulphur-based ligands tends to be higher than for harder oxygen- or nitrogen-donor groups. Despite considerable study of the coordination chemistry of lead(II) with S- or Se-donor atom ligands the rational design of precursor still remains a challenge (Davidovich *et al.*, 2010). Tuning of the structure of the ligands to satisfy the coordination preferences and requirements of the lead(II) atom is still not that well understood (Claudio *et al.*, 2003); the same is true in design of precursors for chalcogenides.

Lead selenide is a promising material in many other applications including lasers (Cui *et al.*, 2006), thermoelectric devices (Harman *et al.*, 2002; Murray *et al.*, 2001) and near-infrared (near-IR) luminescence emitters (Schaller *et al.*, 2003). The selenides and tellurides are potentially superior materials for thermoelectric cooling and electric power generation (Shchennikov and Ovsyannikov, 2003).

The initial use of precursors for the deposition of semiconductor materials by chemical vapour deposition (CVD) (Afzaal *et al.*, 2004; Trindade *et al.*, 1999) include mixing of metal alkyls

and a chalcogenide source in the vapour phase which often resulted in the growth of material before the vapour reaches the heated substrate. To overcome the problem of pre-reaction, high volatility, and reduce toxic hazard, single-source precursors (SSPs) were developed for deposition of thin films and nanoparticles. They have abundant advantages over conventional dual source methods, including air and moisture stability, ease of handling, comparatively low toxicity and lower deposition temperatures. The presence of only one precursor molecule in the supply stream reduces the likelihood and extent of pre-reaction and the associated contamination of deposited materials.

Co-ordination chemistry and deposition studies of a number of metal chalcogenides using phosphinate based metal precursors (Ni, Cd, Cu, Mo, Bi, Pb) (Nguyen *et al.*, 2007) have been explored. Bis(di-phenylthioselenophosphinato) lead(II)  $[\text{Pb}\{(\text{C}_6\text{H}_5)_2\text{PSSe}\}_2]$  has been synthesised (Nguyen *et al.*, 2006) and recently has been used to deposit PbSe thin films and nanoparticles (Akhtar *et al.*, 2011).

A number of precursors containing S- and Se-donor atoms have been proposed as single-source precursors for thin films of PbS or PbSe (Zhang *et al.*, 2005; Afzaal *et al.*, 2004; Boudjouk *et al.*, 1998). Dichalcogenoimidodiphosphinato precursors of  $[\text{Pb}[(\text{E}^i\text{Pr}_2)_2\text{N}]_2]$  (E = S, Se, Te) have been used to deposit lead chalcogenide thin films (Afzaal *et al.*, 2004; Ritch *et al.*, 2010). All the precursors are air-stable except  $[\text{Pb}[(\text{Te}^i\text{Pr}_2)_2\text{N}]_2]$  which is highly unstable. Many of these precursors have been used to deposit PbS or PbSe thin films or nanoparticles (Ritch *et al.*, 2010; Trindade *et al.*, 1999; Acharya *et al.*, 2008).

Mixed compositions are of interest mainly because they allow tuning of the semiconductor properties. Alloyed semiconductor nanomaterials provide a wealth of opportunities for the

controlled development of new materials which may lead to the improvement of new devices. There is little work reported on the preparation and properties of ternary lead chalcogenides ( $\text{PbSe}_x\text{S}_{1-x}$ ) thin films as compared to their binary counterparts (PbS, PbSe and PbTe) (Rogach *et al.*, 2007; Wang *et al.*, 2008).

An experimental observation of labile and reactive intermediates on the surface is ultimately challenging and difficult. Due to the difficulty of assessing such a reaction mechanism by experiment, theoretical calculations can be an excellent means of exploring these processes on a molecular scale. In particular, Akhtar *et al.* (2011) included chemical kinetics, partly based on thermodynamic results of density functional theory (DFT) calculations involved in the gas phase decomposition of  $\text{Pb}[(\text{C}_6\text{H}_5)_2\text{PSSe}]_2$  precursor. However, a differentiation between the reaction mechanisms is hampered by the fact that transition states for the corresponding pathways were not considered in their work.

Computational thermochemistry is an alternative tool to investigate the decomposition mechanism of metal-organic precursors when direct experimental measurements are not available. In this study, density functional theory (DFT) approach was used to report thermodynamic and kinetic parameters for a variety of underlying reaction mechanisms involved in the decomposition process. More specifically, relative free energies and activation free energy barrier of reactants, products, intermediates and transition states involved in all suggested pathways were computed. Reaction rate was also calculated using transition state theory to determine the dominant reaction route of crucial steps involved in the decomposition process.

### 3.2 Details of calculations

All calculations were carried out with Spartan '10 v1.1.0 Molecular Modeling programs (Wavefunction, 2010) at the DFT MO6/LACVP\* level of theory. The LACVP\* basis set is a relativistic effective core-potential that describes the atoms H-Ar with the 6-31G\* basis while heavier atoms are modeled with the LANL2DZ basis set which uses the all-electron valence double zeta basis set (D95V), developed by Dunning, for first row elements (Dunning and Hay, 1976) and the Alamos ECP plus double zeta basis set developed by Wadt and Hay for the atoms Na-La, Hf-Bi (Hay and Wadt, 1985a; 1985b; Wadt and Hay, 1985).

The starting geometries of the molecular systems were constructed using Spartan's graphical model builder and minimized interactively using the sybyl force field (Clarks *et al.*, 1989). All geometries were fully optimized without any symmetry constraints. A normal mode of analysis was performed to verify the nature of the stationary point and equilibrium geometries were characterized by the absence of imaginary frequencies.

The transition state structures were located by a series of constrained geometry optimization in which the breaking bonds are fixed at various lengths while the remaining internal co-ordinates were optimized. The approximate stationary points located from such a procedure were then fully optimized using the standard transition state optimization procedure in Spartan. All first-order saddle-point were shown to have a Hessian matrix with a single negative eigenvalue, characterized by an imaginary vibrational frequency along the reaction coordinate.

The rate constants were calculated using the transition state theory for all elementary steps of the pathways discussed in this section. The unimolecular rate constant,  $k_{\text{uni}}$  and equilibrium

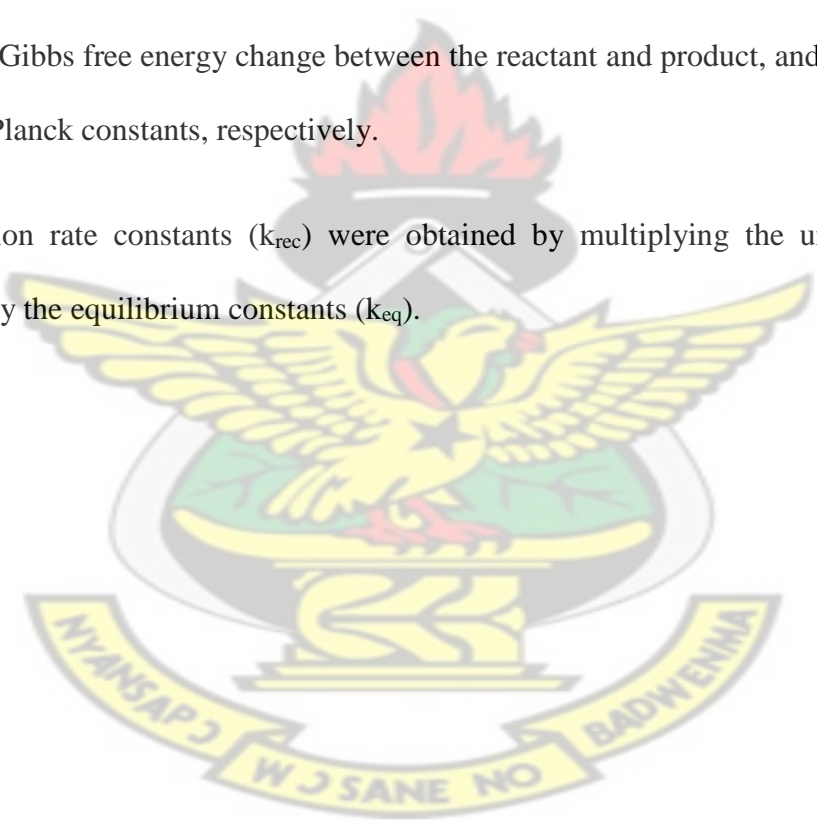
constants,  $K_{eq}$  were computed using Eqs. (3.1) and (3.2), respectively, which were derived from the transition state theory (Benson, 1960; Glasstone *et al.*, 1941) and assuming that the transmission coefficient,  $\kappa$  is equal to 1.

$$k_{uni} = \left( \frac{\kappa k_B T}{h} \right) \exp\left( -\frac{\Delta G^\ddagger}{RT} \right) \quad (3.1)$$

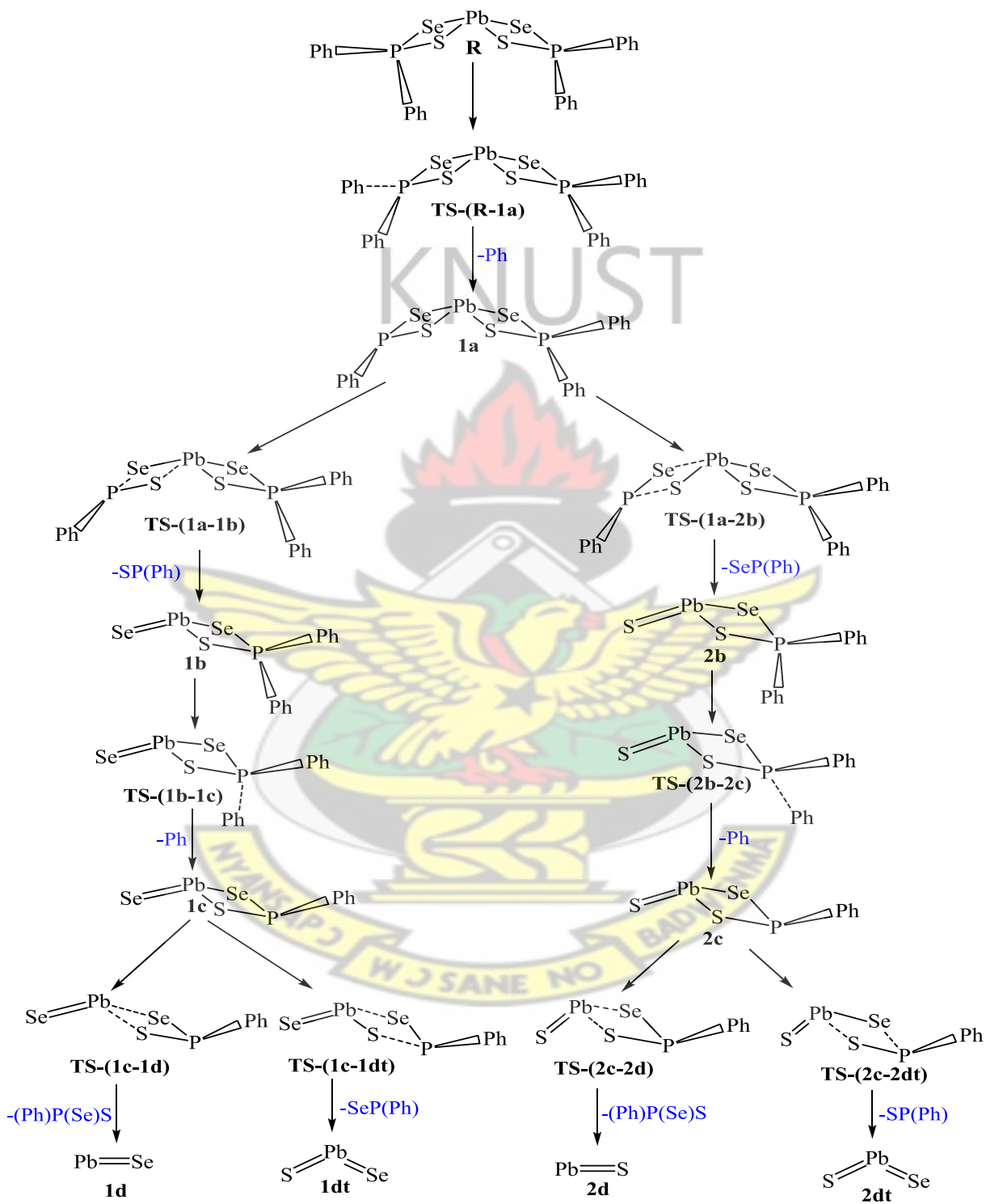
$$k_{eq} = \exp(-\Delta G^0/RT) \quad (3.2)$$

where  $\Delta G^\ddagger$  is the Gibbs free energy change between the reactant and its corresponding transition state,  $\Delta G^0$  is the Gibbs free energy change between the reactant and product, and  $k_B$  and  $h$  are the Boltzmann and Planck constants, respectively.

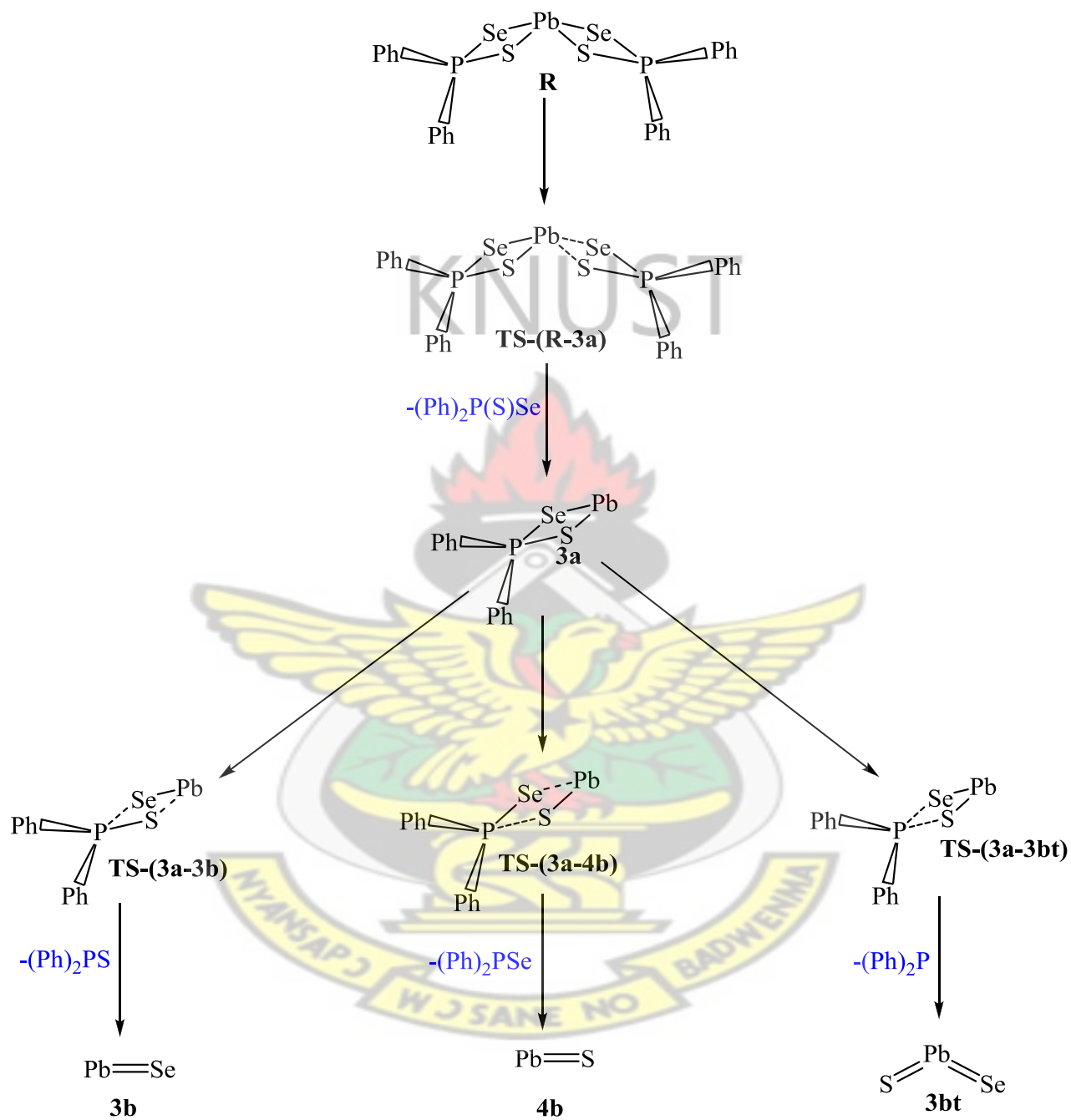
The recombination rate constants ( $k_{rec}$ ) were obtained by multiplying the unimolecular rate constants ( $k_{uni}$ ) by the equilibrium constants ( $k_{eq}$ ).



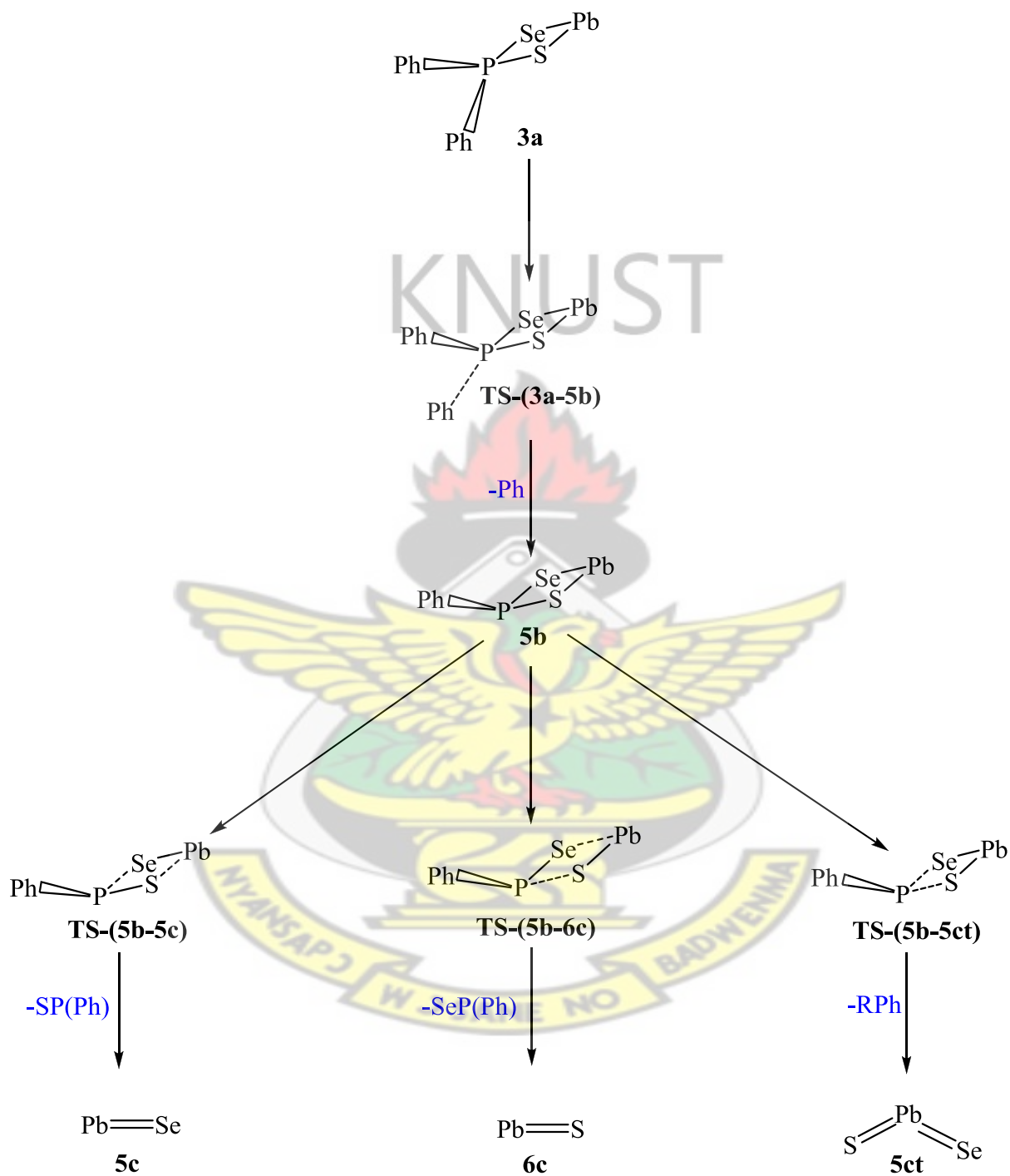
Scheme 3.1: Decomposition pathway (1, 2) of  $\text{Pb}[(\text{C}_6\text{H}_5)_2\text{PSSe}]_2$  precursor



Scheme 3.2: Decomposition pathway (3, 4) of  $\text{Pb}[(\text{C}_6\text{H}_5)_2\text{PSSe}]_2$  precursor



Scheme 3.3: Decomposition pathway (5, 6) of  $\text{Pb}[(\text{C}_6\text{H}_5)_2\text{PSSe}]_2$  precursor



### 3.3 Mechanistic considerations

A number of different thermal decomposition pathways as suggested by Akhtar *et al.* (2011) were investigated for  $[\text{Pb}\{(\text{C}_6\text{H}_5)_2\text{PSSe}\}_2]$  precursor and their corresponding reaction free energies,  $\Delta G^\circ$  were calculated, both at room temperature (298.15 K) and elevated temperature (800 K) (Schemes 3.1, 3.2 and 3.3). The first two mechanisms considered (**1**, **2**) involved the initial loss of phenyl radical to form **1a** on the doublet potential energy surface. The next step is either the loss of  $\text{SP}(\text{C}_6\text{H}_5)$  or  $\text{SeP}(\text{C}_6\text{H}_5)$  from **1a** to form **1b** or **2b** on the doublet PES. The **1b** and **2b** intermediates further decompose to form  $(\text{C}_6\text{H}_5)_2\text{PSSe-Pb-Se}$  **1c** and  $(\text{C}_6\text{H}_5)_2\text{PSSe-Pb-S}$  **2c** on the singlet PES, followed by the subsequent decomposition of  $(\text{C}_6\text{H}_5)\text{PSSe-Pb-Se}$  **1c** to give  $\text{PbSe}$  **1d** or  $\text{PbSe}_x\text{S}_{1-x}$  **1dt**, and  $(\text{C}_6\text{H}_5)\text{PSSe-Pb-S}$  **2c** to give  $\text{PbS}$  **2d** or  $\text{PbSe}_x\text{S}_{1-x}$  **2dt** on the singlet PES. In the second set of possible mechanisms (**3**, **4**) that was studied, the initial step involved the loss of  $\text{SeSP}(\text{C}_6\text{H}_5)_2$  entity to form  $(\text{C}_6\text{H}_5)_2\text{PSSe-Pb}$  **3b** intermediate on the doublet PES. The subsequent step could be the loss of  $\text{PbS}$  **4b**,  $\text{PbSe}$  **3b** or  $\text{PbSe}_x\text{S}_{1-x}$  **3bt** from **3b** on the doublet PES. An alternative route (**5**, **6**) were also investigated, involving first the loss phenyl radical to form  $(\text{C}_6\text{H}_5)\text{PSSe-Pb}$  **5b** on the singlet PES, and the subsequent step involves the decomposition of **5b** to give  $\text{PbSe}$  **5c**,  $\text{PbS}$  **6c** or  $\text{PbSe}_x\text{S}_{1-x}$  **5ct** on the singlet PES. The singlet and the doublet species were computed as neutral structures.

### 3.4 Results and discussion

#### 3.4.1 Optimized Geometry of Pb[(C<sub>6</sub>H<sub>5</sub>)<sub>2</sub>PSSe]<sub>2</sub> precursor

The optimized geometry for Pb[(C<sub>6</sub>H<sub>5</sub>)<sub>2</sub>PSSe]<sub>2</sub> precursor is shown in Table 3.1. The six membered rings made up from the chelating ligands and the metal centre is distorted from planarity. The metal centre adopts a distorted square pyramidal geometry with two sulphur and two selenium atoms forming the base of the pyramid with ligand bond angles of 74.58° and 75.90° which are slightly smaller than the perfect square planar angle. The two sulphur and two selenium atoms form the base of the pyramid with lone pair occupying the axial position. The density functional theory (DFT) geometry optimization of the precursor on a singlet potential energy surface (PES) has an average bond length of 2.76 Å (Pb-S), as expected, shorter than the bond length of Pb-Se (2.99 Å). The significant disparity in the Pb–Se bond distance at 3.01 Å suggests a stereochemical influence from the lone pair on the metal centre. The non-coordinating S and Se atoms are each proximate to the Pb(II) atom, giving rise to distortions from the ideal geometry as evident in the wide S-Pb-Se bond angle of 153.04°.

The average bond angle around S/Se-Pb-S/Se is 95.45°, which are similar to the values in related lead dithiocarbamates (Afzaal *et al.*, 2004). The geometrical parameters are in reasonable agreement with experimentally determined X-ray data on Pb[(C<sub>6</sub>H<sub>5</sub>)<sub>2</sub>PSSe]<sub>2</sub> precursor (Akhtar *et al.*, 2011). Minor differences in bond lengths and angles can be attributed, at least in part, to crystal packing forces that are not present in gas phase.

Table 3.1: Selected bond lengths (Å) and bond angles (°) of experimental and optimised (calculate)

Pb[(C<sub>6</sub>H<sub>5</sub>)<sub>2</sub>PSSe]<sub>2</sub> precursor

Bonds	length(Å)	length(Å)	bonds	angles (°)	angles (°)
		X-ray			X-ray
		crystallography <sup>a</sup>			crystallography <sup>a</sup>
P-S	2.0154	2.190(3)	P-Se-Pb	90.22	89.10(3)
P-Se	2.2243	2.151(6)	P-S-Pb	83.07	84.00(18)
S-P	2.0517	-	S-Pb-Se	74.58	94.10(7)
Se-P	2.1867	-	Se-Pb-S	75.90	75.62(19)
Pb-S	2.9727	2.903(6)	Se-Pb-Se	88.89	89.10(3)
Pb-Se	2.8052	3.017(5)	S-Pb-S	84.58	84.00(18)
Se-Pb	3.0186	3.044(2)	S-Pb-Se	153.04	154.40(2)
S-Pb	2.7162	2.812(8)	Se-Pb-S	95.76	94.40(2)

<sup>a</sup> (Akhtar *et al.*, 2011)

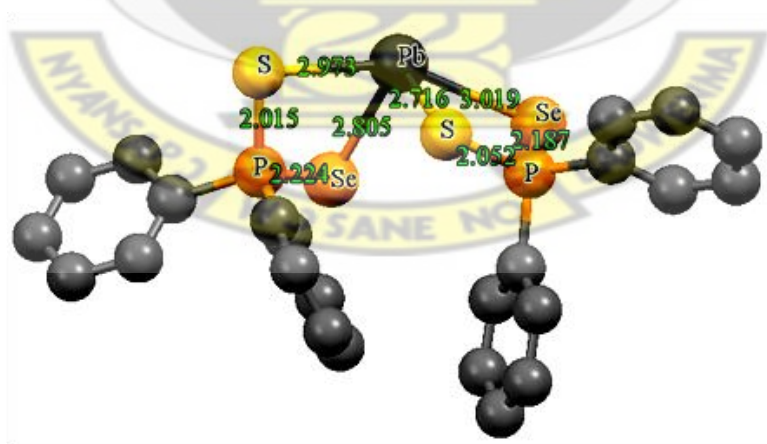


Figure 3.1: Optimized geometry of Pb[(C<sub>6</sub>H<sub>5</sub>)<sub>2</sub>PSSe]<sub>2</sub> single-source precursor

### 3.4.2 Overall Decomposition of $\text{Pb}[(\text{C}_6\text{H}_5)_2\text{PSSe}]_2$ precursor

The reaction mechanisms involved in the decomposition pathway (1, 2) were studied by considering the energetics of the reactants, intermediates and products (Scheme 3.1). Relevant transition state structures,  $\Delta G^\circ$  (298.15 K and 800 K) for each intermediate at infinite separation and  $\Delta G^\ddagger$  (298.15 K and 800 K) for each individual step relative to the reactants, intermediates and products for the various reaction mechanism at the MO6/LACVP\* level of theory are given in Figures 3.2 and 3.3.

The activation free energy barrier involved in the formation of **1a** intermediate through a transition state **TS-(R-1a)** was calculated as +88.68 kcal/mol (298.15 K) and +88.03 kcal/mol (800 K) with a reaction free energy of +67.05 kcal/mol (298.15 K) and +44.80 kcal/mol (800 K) on the doublet PES.

The subsequent step is either the loss of  $\text{SP}(\text{C}_6\text{H}_5)$  or  $\text{SeP}(\text{C}_6\text{H}_5)$  and conversion of **1a** intermediate forms either  $(\text{C}_6\text{H}_5)_2\text{PSSe-Pb-Se}$  **1b** or  $(\text{C}_6\text{H}_5)_2\text{PSSe-Pb-S}$  **2b** through the transition state **TS-(1a-1b)** or **TS-(2a-2b)** on the doublet PES. The activation free energy barrier involved in the process was +8.61 kcal/mol (298.15 K) and +30.95 kcal/mol (800 K) for **1b**, and +12.35 kcal/mol (298.15 K) and +34.33 kcal/mol (800 K) for **2b**. The reaction free energy for these processes was -46.28 kcal/mol (298.15 K) and -40.93 kcal/mol (800 K) for **1b**, and -36.40 kcal/mol (298.15 K) and -35.18 kcal/mol (800 K) for **2b**.

The intermediates  $(\text{C}_6\text{H}_5)_2\text{PSSe-Pb-Se}$  **1b** and  $(\text{C}_6\text{H}_5)_2\text{PSSe-Pb-S}$  **2b** were further decomposed to form  $(\text{C}_6\text{H}_5)\text{PSSe-Pb-Se}$  intermediate **1c** and  $(\text{C}_6\text{H}_5)\text{PSSe-Pb-S}$  intermediate **2c** respectively through the transition state **TS-(1b-1c)** and **TS-(2b-2c)** after a loss of a second phenyl

radical on the singlet PES. The activation free energy barrier was calculated as +52.62 kcal/mol (298.15 K) and +59.84 kcal/mol (800 K) for **1c**, and +39.17 kcal/mol (298.15 K) and +70.34 kcal/mol (800 K) for **2c**. The reaction free energy was +44.84 kcal/mol (298.15 K) and +33.08 kcal/mol (800 K) for **1c**, and +28.77 kcal/mol (298.15 K) and +16.43 kcal/mol (800 K) for **2c**.

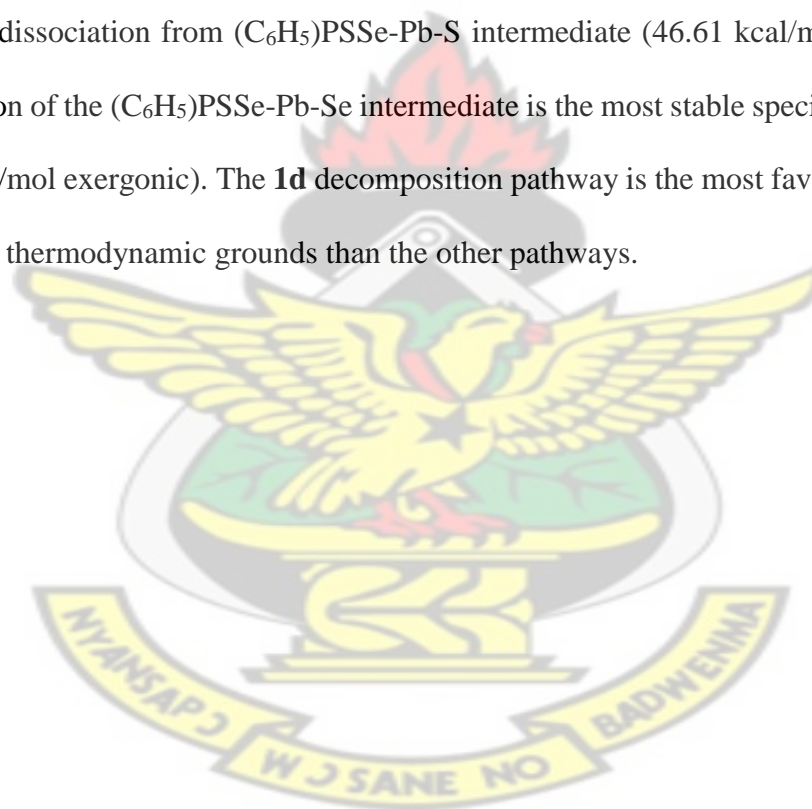
The (C<sub>6</sub>H<sub>5</sub>)PSSe-Pb-Se **1c** intermediate can go through two different pathways to form either PbSe **1d** or ternary PbSe<sub>x</sub>S<sub>1-x</sub> **1dt** on the singlet PES. The decomposition of (C<sub>6</sub>H<sub>5</sub>)PSSe-Pb-Se **1c** intermediate to form PbSe **1d** along the transition state **TS-(1c-1d)** has an activation free energy barrier of +1.98 kcal/mol (298.15 K) and +34.33 kcal/mol (800 K), and reaction free energy of -68.70 kcal/mol (298.15 K) and -57.17 kcal/mol (800 K). The optimized geometry of **TS-(1c-1d)** further reveals the elongation of Pb-Se bond length from 2.973 to 3.524 Å and Pb-S bond length from 2.757 to 3.711 Å. The activation free energy barrier involved in the formation of ternary PbSe<sub>x</sub>S<sub>1-x</sub> **1dt** along the transition state **TS-(1c-1dt)** was +9.24 kcal/mol (298.15 K) and +38.86 kcal/mol (800 K) and exergonic by 43.40 kcal/mol (298.15) and 45.28 kcal/mol (800 K). The optimized geometry of **TS-(1c-1dt)** further reveals the elongation of Pb-Se bond length from 2.973 to 3.252 Å and Pb-S bond length from 2.253 to 3.911 Å.

The (C<sub>6</sub>H<sub>5</sub>)PSSe-Pb-S **2c** intermediate can also decompose through a transition state **TS-(2c-2d)** to form PbS **2d** with activation free energy barrier of +13.36 kcal/mol (298.15 K) and +46.61 kcal/mol (800 K) and exergonic by 61.51 kcal/mol (298.15 K) and 45.29 kcal/mol (800 K) on the singlet PES. The optimized geometry of **TS-(2c-2d)** further reveals the elongation of Pb-Se bond length from 2.838 to 3.380 Å and Pb-S bond length from 2.746 to 3.853 Å.

The transition state **TS-(2c-2dt)** along the **2c** pathway to form ternary PbSe<sub>x</sub>S<sub>1-x</sub> **2dt** has an activation free energy barrier of +7.46 kcal/mol (298.15 K) and +40.81 kcal/mol (800 K), and

exergonic by 40.55 kcal/mol (298.15 K) and 36.72 kcal/mol (800 K) on the singlet PES. The optimized geometry of **TS-(2c-2dt)** further reveals the elongation of Pb-S bond length from 2.746 to 2.953 Å and P-Se bond length from 2.282 to 2.910 Å.

On the singlet PES, the decomposition of (C<sub>6</sub>H<sub>5</sub>)PSSe-Pb-Se/-S intermediates reveal that, the **[1d]** dissociation of (C<sub>6</sub>H<sub>5</sub>)P(Se)S from (C<sub>6</sub>H<sub>5</sub>)PSSe-Pb-Se intermediate to form PbSe has the lowest barrier (34.33 kcal/mol) compared to **[1dt]** dissociation from (C<sub>6</sub>H<sub>5</sub>)PSSe-Pb-Se intermediate (38.86 kcal/mol), **[2dt]** dissociation from (C<sub>6</sub>H<sub>5</sub>)PSSe-Pb-S intermediate (40.81 kcal/mol), **[2d]** dissociation from (C<sub>6</sub>H<sub>5</sub>)PSSe-Pb-S intermediate (46.61 kcal/mol). PbSe formed from optimization of the (C<sub>6</sub>H<sub>5</sub>)PSSe-Pb-Se intermediate is the most stable species on the reaction PES (57.17 kcal/mol exergonic). The **1d** decomposition pathway is the most favoured pathway on both kinetic and thermodynamic grounds than the other pathways.



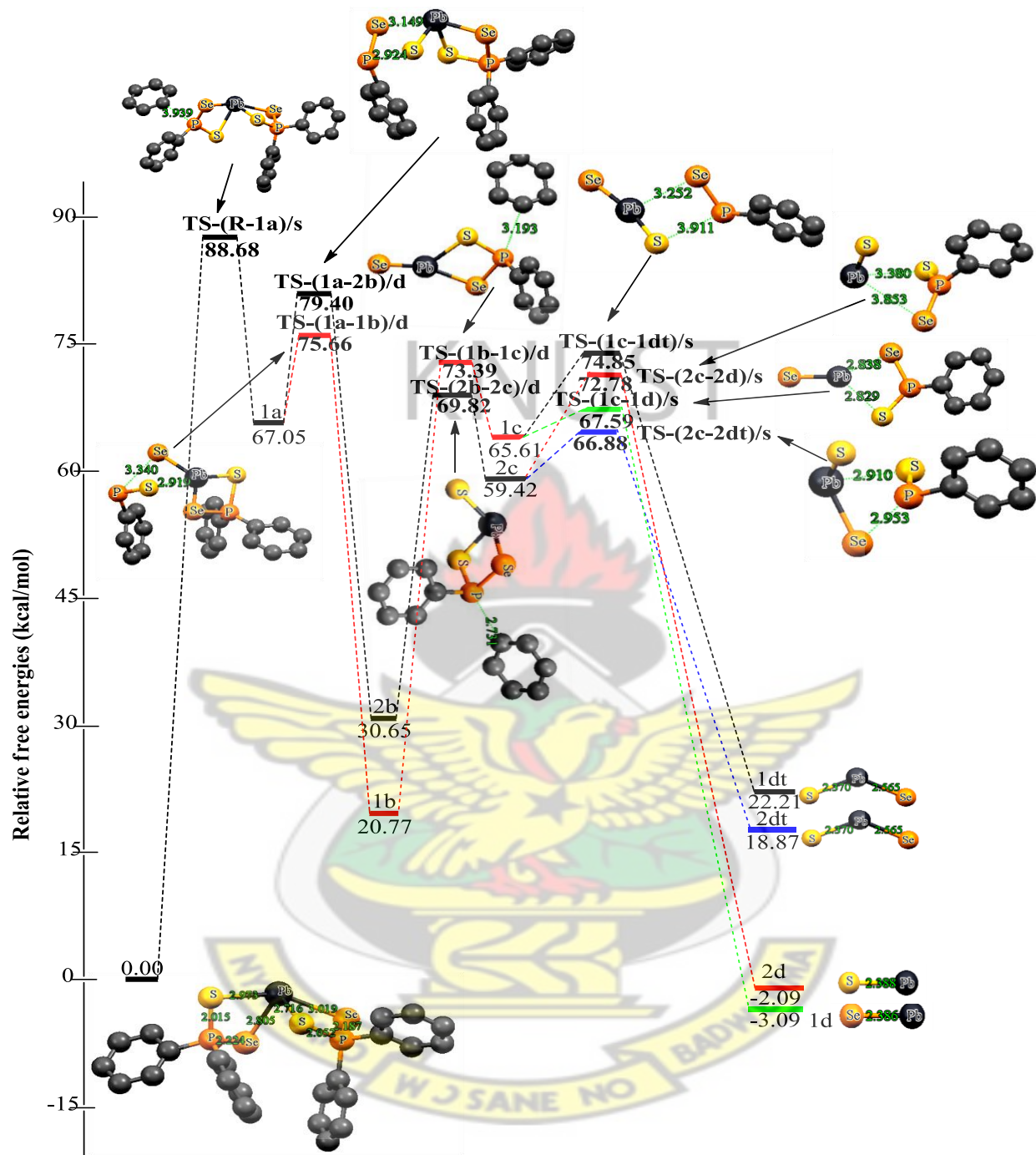


Figure 3.2: Energetics of the unimolecular decomposition pathway (1, 2) at 298.15 K. The relative free energies are in kcal/mol and bond distances in Å

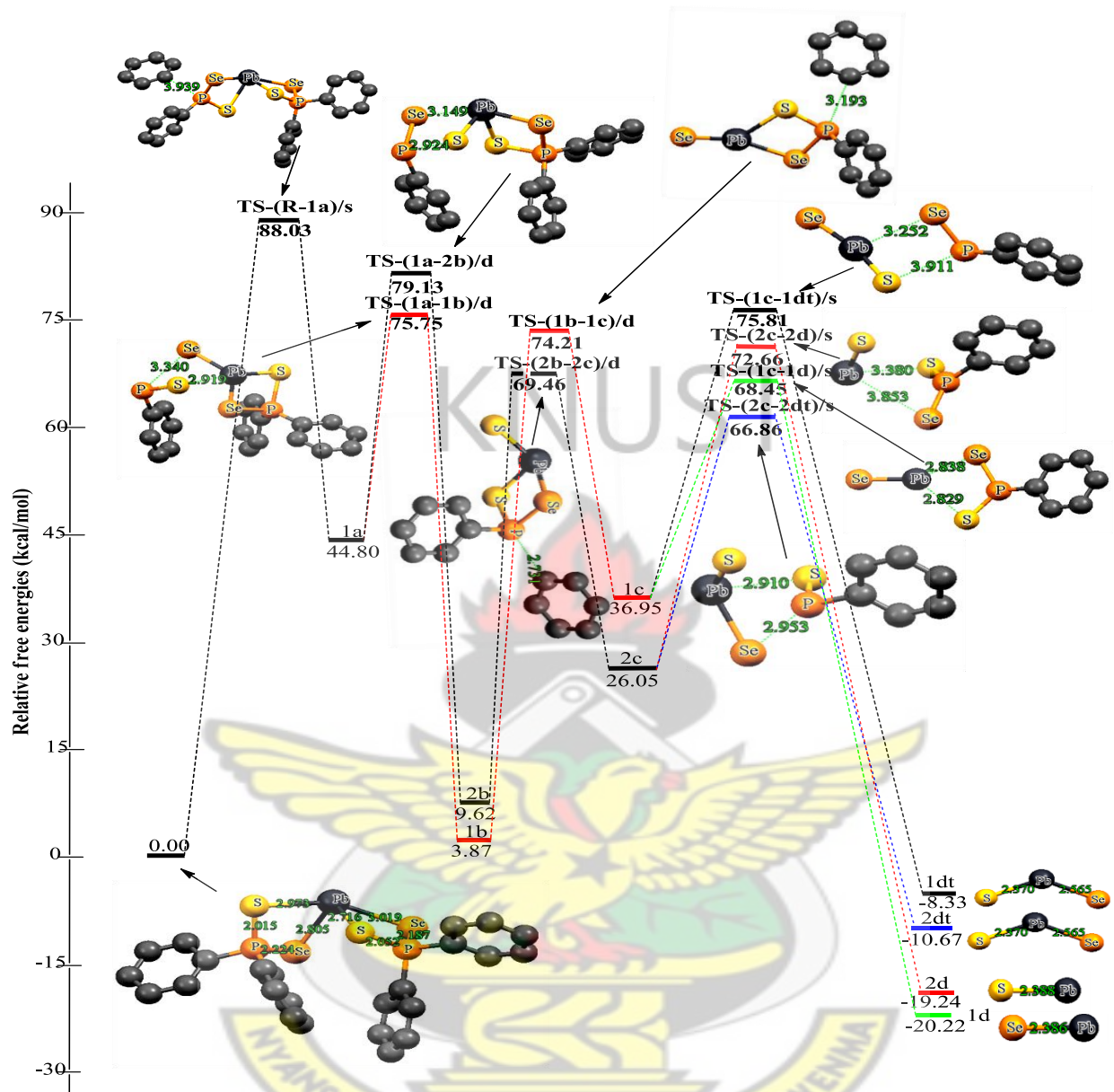


Figure 3.3: Energetics of the unimolecular decomposition pathway (1, 2) at 800 K. The relative free energies are in kcal/mol and bond distances in Å

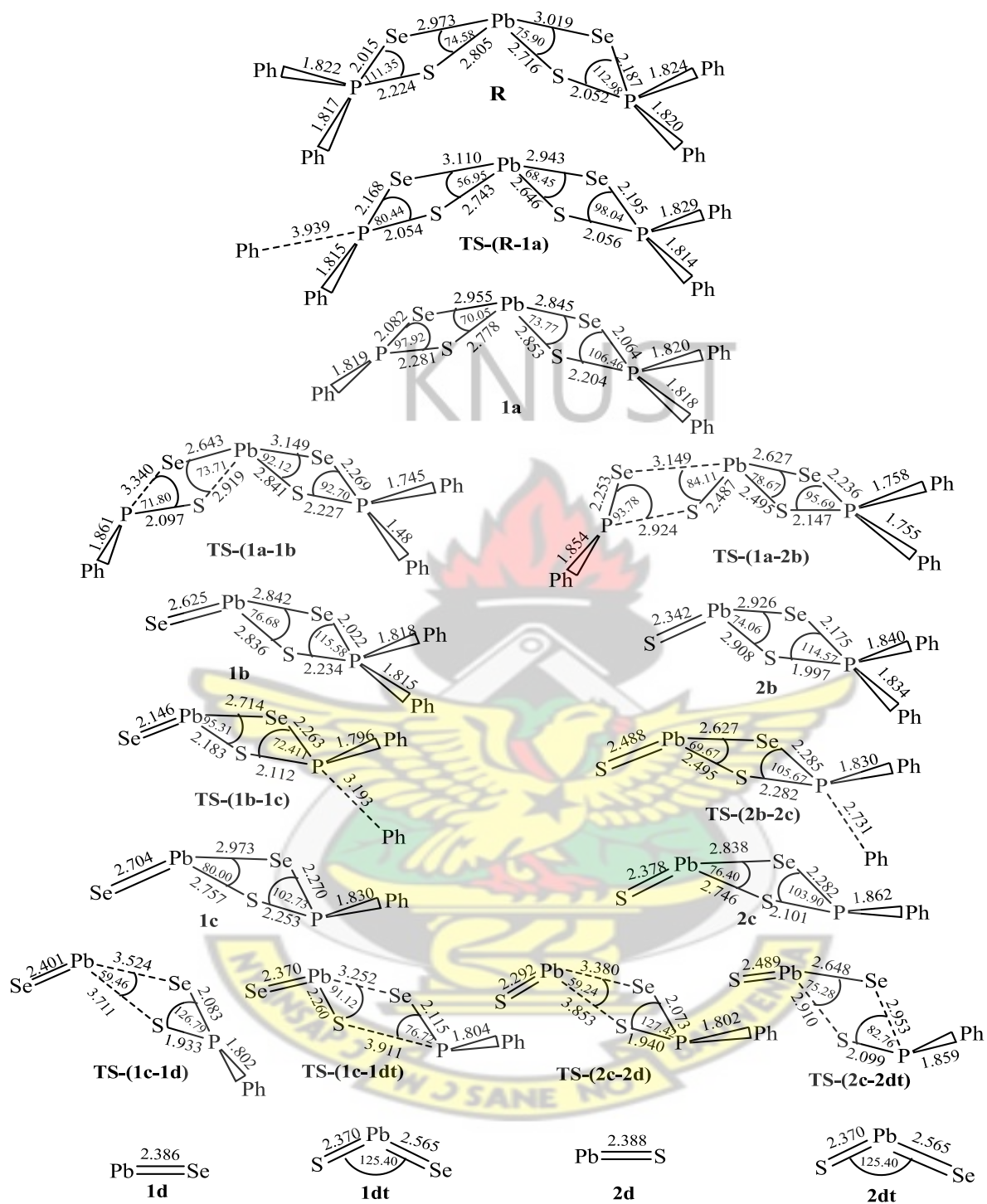


Figure 3.4: Optimized geometrical parameters of the main stationary points involved in the unimolecular decomposition pathway (1, 2). Bond distances in Å and bond angles in degrees

The reaction mechanisms involved in the decomposition of  $(\text{C}_6\text{H}_5)_2\text{PSSe-Pb}$  radical were studied by considering the energetics of reactants, intermediates and products (Scheme 3.2). The computed potential energy surfaces for all the possible unimolecular pathways accessible to the  $(\text{C}_6\text{H}_5)_2\text{PSSe-Pb}$  radical are given in Figures 3.5 and 3.6. The activation free energy barrier involved in the decomposition of  $\text{Pb}[(\text{C}_6\text{H}_5)_2\text{PSSe}]_2$  precursor to form  $(\text{C}_6\text{H}_5)_2\text{PSSe-Pb}$  **3a** intermediate was +65.34 kcal/mol (298.15 K) and +65.27 kcal/mol (800 K) with a reaction free energy of -59.42 kcal/mol (298.15 K) and -24.05 kcal/mol (800 K) on the doublet PES.

The formation of PbSe on the doublet PES through a transition state **TS-(3a-3b)** has an activation free energy barrier of -11.97 kcal/mol (298.15 K) and +23.28 kcal/mol (800 K) and reaction free energy of -42.21 kcal/mol (298.15 K) and -24.08 kcal/mol (800 K). This unimolecular decomposition, however, has the lowest activation free energy barrier and will proceed very fast with a unimolecular and bimolecular recombination rate constants of  $1.96 \times 10^6 \text{ s}^{-1} \text{ K}$  and  $2.06 \times 10^6 \text{ s}^{-1}$  at  $T = 800 \text{ K}$  respectively. The optimized geometry of **TS-(3a-3b)** further reveals the elongation of Pb-S bond length from 2.593 to 3.150 Å and P-Se bond length from 2.244 to 3.050 Å.

Also, the activation free energy barrier involved in the formation of PbS **4b** through a transition state **TS-(3a-4b)** was -3.73 kcal/mol (298.15 K) and +31.48 kcal/mol (800 K) with a reaction free energy of -40.01 kcal/mol (298.15 K) and -22.36 kcal/mol (800 K) on the doublet PES. The optimized geometry of **TS-(3a-4b)** further reveals the elongation of Pb-Se bond length from 2.683 to 3.134 Å and P-S bond length from 2.074 to 3.366 Å. The transition state energies involved in the decomposition of  $(\text{C}_6\text{H}_5)_2\text{PSSe-Pb}$  intermediate to form either PbS or PbSe was lower than the free energy of the intermediate molecule at  $T = 298.15 \text{ K}$ . Thus these calculations

predict that in the gas phase, PbSe or PbS decomposition pathway is likely to occur without a barrier at T = 298.15 K.

Decomposition of  $(\text{C}_6\text{H}_5)_2\text{PSSe-Pb}$  **3b** intermediate was further explored to access the ternary nature of  $(\text{C}_6\text{H}_5)_2\text{PSSe-Pb}$  intermediate. The activation barrier involved in the formation of ternary  $\text{PbSe}_x\text{S}_{1-x}$  **3bt** through a transition state **TS-(3a-3bt)** has been computed as +15.4 kcal/mol (298.15 K) and +50.68 kcal/mol (800 K) with reaction free energy of -53.39 kcal/mol (298.15 K) and -50.05 kcal/mol (800 K). The optimized geometry of **TS-(3a-3bt)** further reveals the elongation of P-Se bond length from 2.244 to 2.932 Å and P-S bond length from 2.074 to 3.107 Å.

In terms of kinetic, the most favourable pathway along the  $(\text{C}_6\text{H}_5)_2\text{PSSe-Pb}$  intermediate involves the dissociation of  $(\text{C}_6\text{H}_5)_2\text{PS}$  to form PbSe [**3b**]. The barrier along this pathway is 23.28 kcal/mol lower than the barrier along the [**4b**] dissociation route (31.48 kcal/mol) and [**3bt**] dissociation route (50.68 kcal/mol). Ternary  $\text{PbSe}_x\text{S}_{1-x}$  [**3bt**] formed from optimization of the  $(\text{C}_6\text{H}_5)_2\text{PSSe-Pb}$  intermediate is the most stable species on the reaction PES (50.05 kcal/mol exergonic). Thermodynamically the most favoured pathway is the **3bt** dissociation pathway. The rate constants for the **3bt** pathway was calculated as  $8.84 \times 10^{-43} \text{ s}^{-1}$  (298.15 K) and  $6.41 \times 10^{-8} \text{ s}^{-1}$  (800 K).

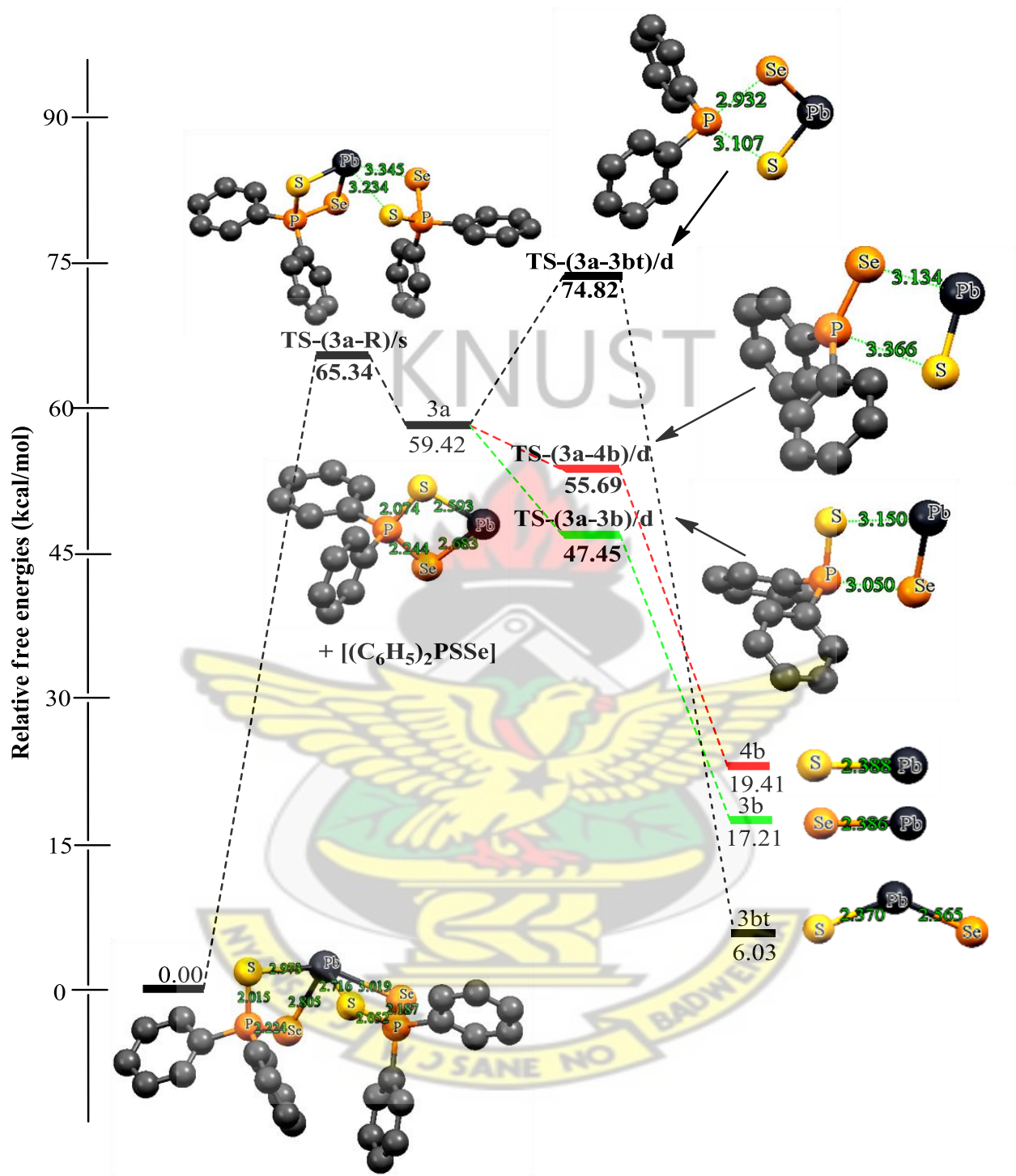


Figure 3.5: Energetics of the unimolecular decomposition pathway (3, 4) at 298.15 K. The relative free energies are in kcal/mol and bond distances in Å

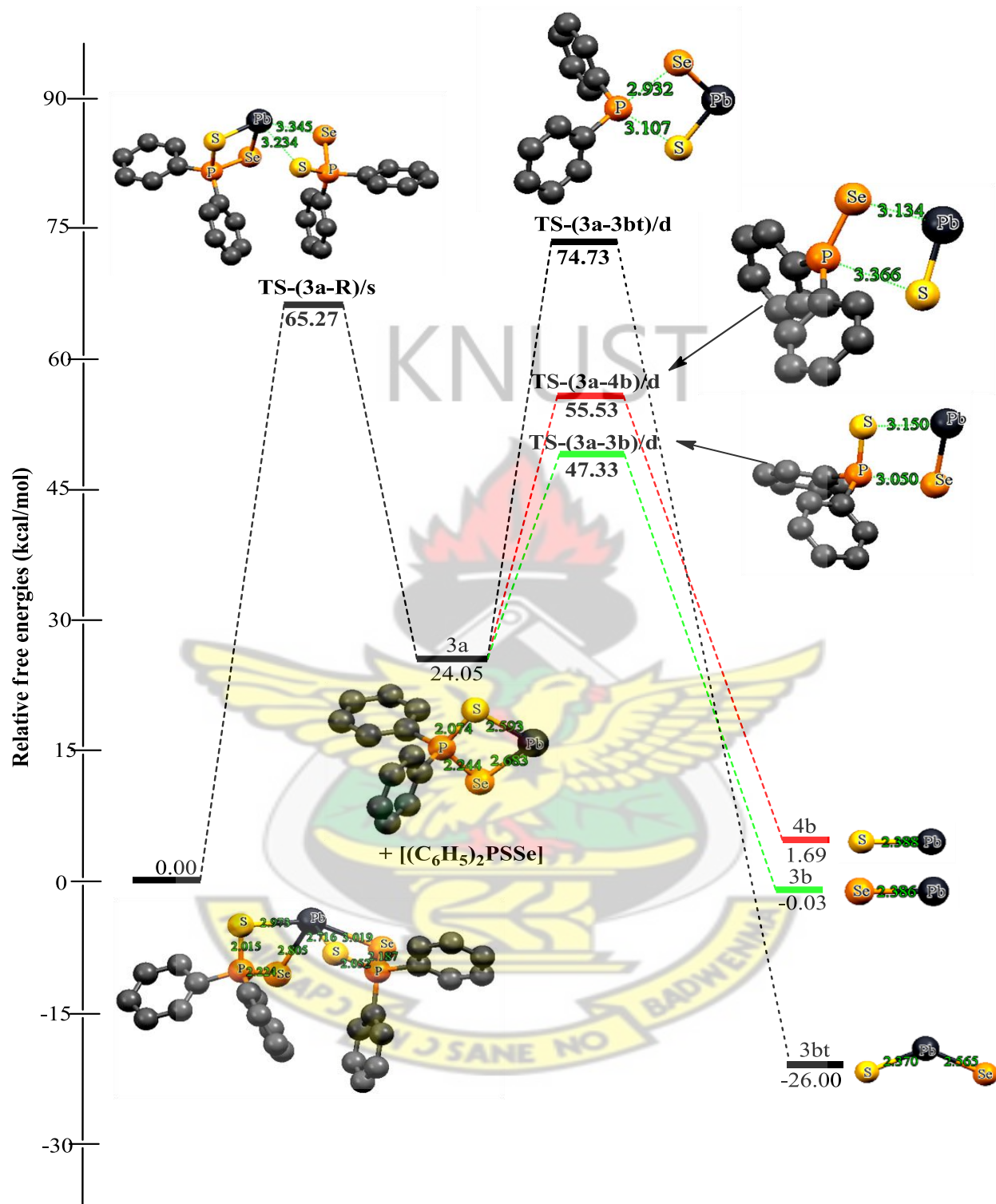


Figure 3.6: Energetics of the unimolecular decomposition pathway (3, 4) at 800 K. The relative free energies are in kcal/mol and bond distances in Å

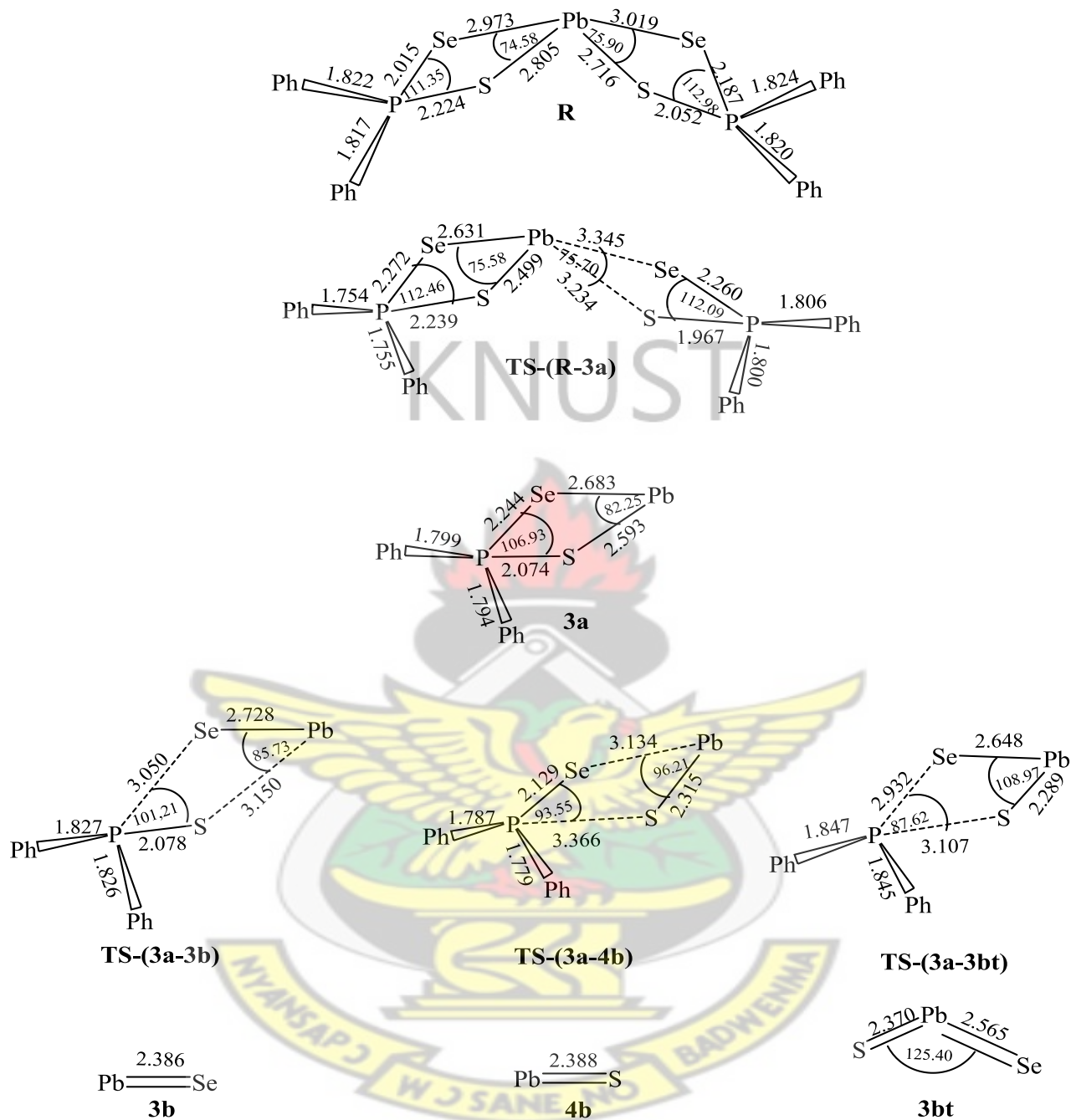


Figure 3.7: Optimized geometrical parameters of the main stationary points involved in the unimolecular decomposition pathway (3, 4). Bond distances in Å and bond angles in degrees

The reaction mechanisms involved in the decomposition of  $(\text{C}_6\text{H}_5)\text{PSSe-Pb}$  intermediate were studied by considering the energetics of reactants, intermediates and products (Scheme 3.3). The computed potential energy surfaces for all the possible unimolecular pathways accessible to the  $(\text{C}_6\text{H}_5)\text{PSSe-Pb}$  intermediate are given in Figures 3.8 and 3.9.

The decomposition of  $(\text{C}_6\text{H}_5)_2\text{PSSe-Pb}$  **3a** intermediate was further explored by abstracting isopropyl radical to form  $(\text{C}_6\text{H}_5)\text{PSSe-Pb}$  **5b** intermediate on the singlet PES. The activation free energy barrier was calculated as +15.38 kcal/mol (298.15 K) and +53.40 kcal/mol (800 K) with a reaction free energy of -31.14 kcal/mol (298.15 K) and -14.13 kcal/mol (800 K).

The formation of  $\text{PbSe}$  **5c** from the intermediate **5b** through the transition state **TS-(5b-5c)** has an activation free energy barrier of +14.40 kcal/mol (298.15 K) and +47.94 kcal/mol (800 K) and reaction free energy of -7.12 kcal/mol (298.15 K) and -3.66 kcal/mol (800 K) on the singlet PES. The optimized geometry of **TS-(5b-5c)** further reveals the elongation of Pb-S bond length from 2.531 to 2.841 Å and P-Se bond length from 2.321 to 4.700 Å.

The activation free energy barrier and reaction energy for the loss of  $(\text{C}_6\text{H}_5)\text{PSe}$  through the transition state **TS-(5b-6c)** to form  $\text{PbS}$  **6c** were +19.54 kcal/mol (298.15 K) and +36.33 kcal/mol (800 K), and -1.79 kcal/mol (298.15 K) and -2.61 kcal/mol (800 K) respectively on the singlet PES. The optimized geometry of **TS-(5b-6c)** further reveals the elongation of Pb-Se bond length from 2.637 to 2.786 Å and P-S bond length from 2.157 to 3.482 Å.

The decomposition of  $(\text{C}_6\text{H}_5)\text{PSSe-Pb}$  **5b** intermediate to form ternary  $\text{PbSe}_x\text{S}_{1-x}$  **5ct** through transition state **TS-(5b-5ct)** has a barrier of +7.09 kcal/mol (298.15 K) and +23.92 kcal/mol (800 K) and exergonic by 4.86 kcal/mol (298.15 K) and 4.23 kcal/mol (800 K) on the

singlet PES. The optimized geometry of **TS-(5b-5ct)** further reveals the elongation of P-Se bond length from 2.321 to 3.189 Å and P-S bond length from 2.157 to 3.344 Å.

The activation energies involved in the main mechanistic steps - PbS (46.30 kcal/mol), PbSe (33.95 kcal/mol) and ternary PbSe<sub>x</sub>S<sub>1-x</sub> (33.85 kcal/mol) are all in the narrow range of 33 to 46 kcal/mol (Figure 3.9). The results suggest that PbSe **5c** and PbSe<sub>x</sub>S<sub>1-x</sub> **5ct** reaction pathways should be competitive in the temperature range used for CVD.

In terms of kinetic, the **5ct** dissociation pathway to form ternary PbSeS<sub>1-x</sub> is slightly favourable than the **[5c]** and **[6c]** dissociation pathways. The barrier along this pathway is 23.92 kcal/mol lower than the barrier along the **[5c]** dissociation route (24.02 kcal/mol) and **[6c]** dissociation route (36.33 kcal/mol). Ternary PbSeS<sub>1-x</sub> **[5ct]** formed from optimization of the (C<sub>6</sub>H<sub>5</sub>)PSSe-Pb intermediate is the most stable species on the reaction PES (4.23 kcal/mol exergonic). In terms of equilibrium thermodynamic, the **5ct** dissociation pathway is the most favourable pathway. The rate constant along this pathway was  $9.54 \times 10^{-13} \text{ s}^{-1}$  (298.15 K) and  $9.21 \times 10^3 \text{ s}^{-1}$  (800 K).

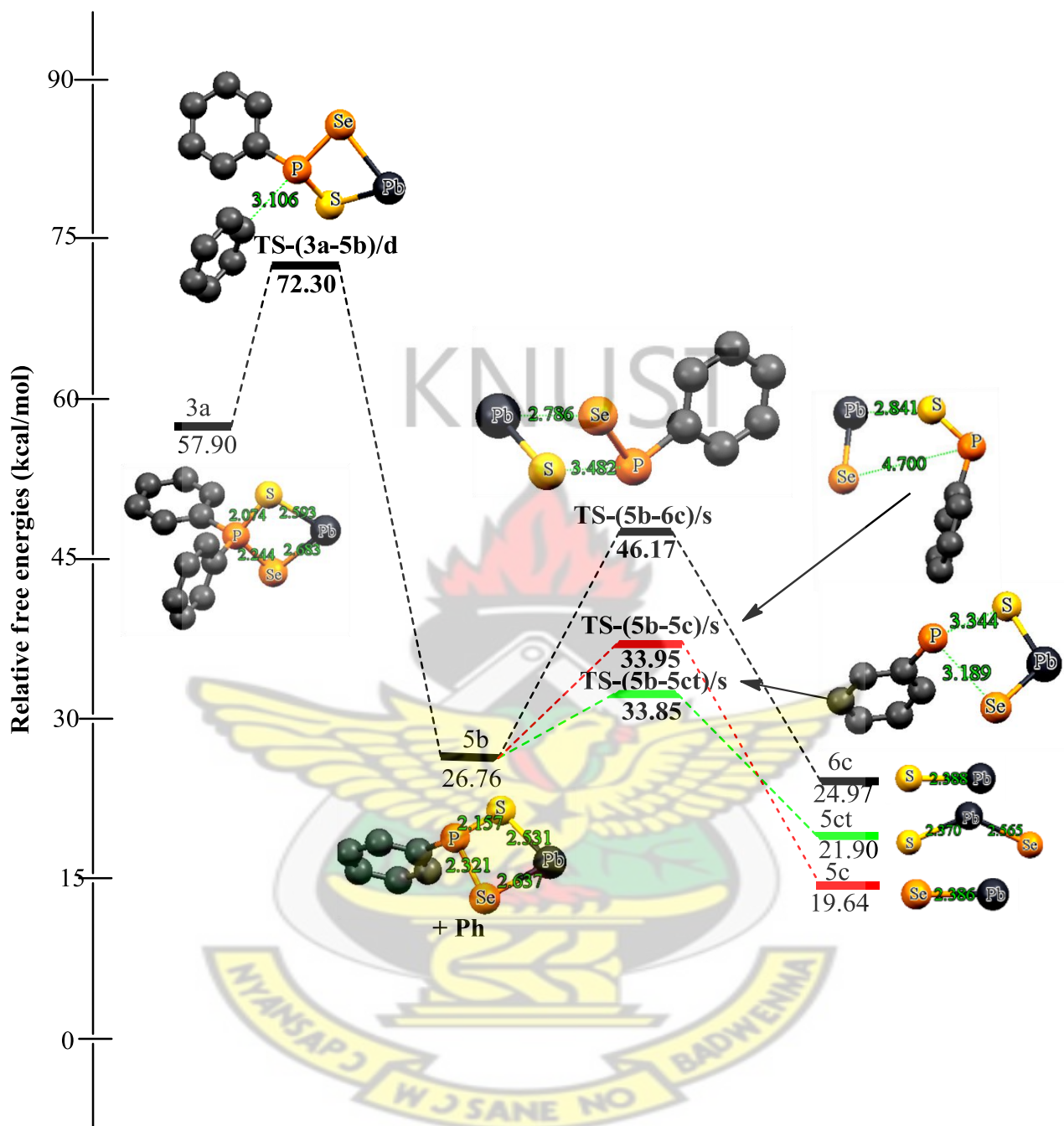


Figure 3.8: Energetics of the unimolecular decomposition pathway (5, 6) at 298.15 K. The relative free energies are in kcal/mol and bond distances in Å

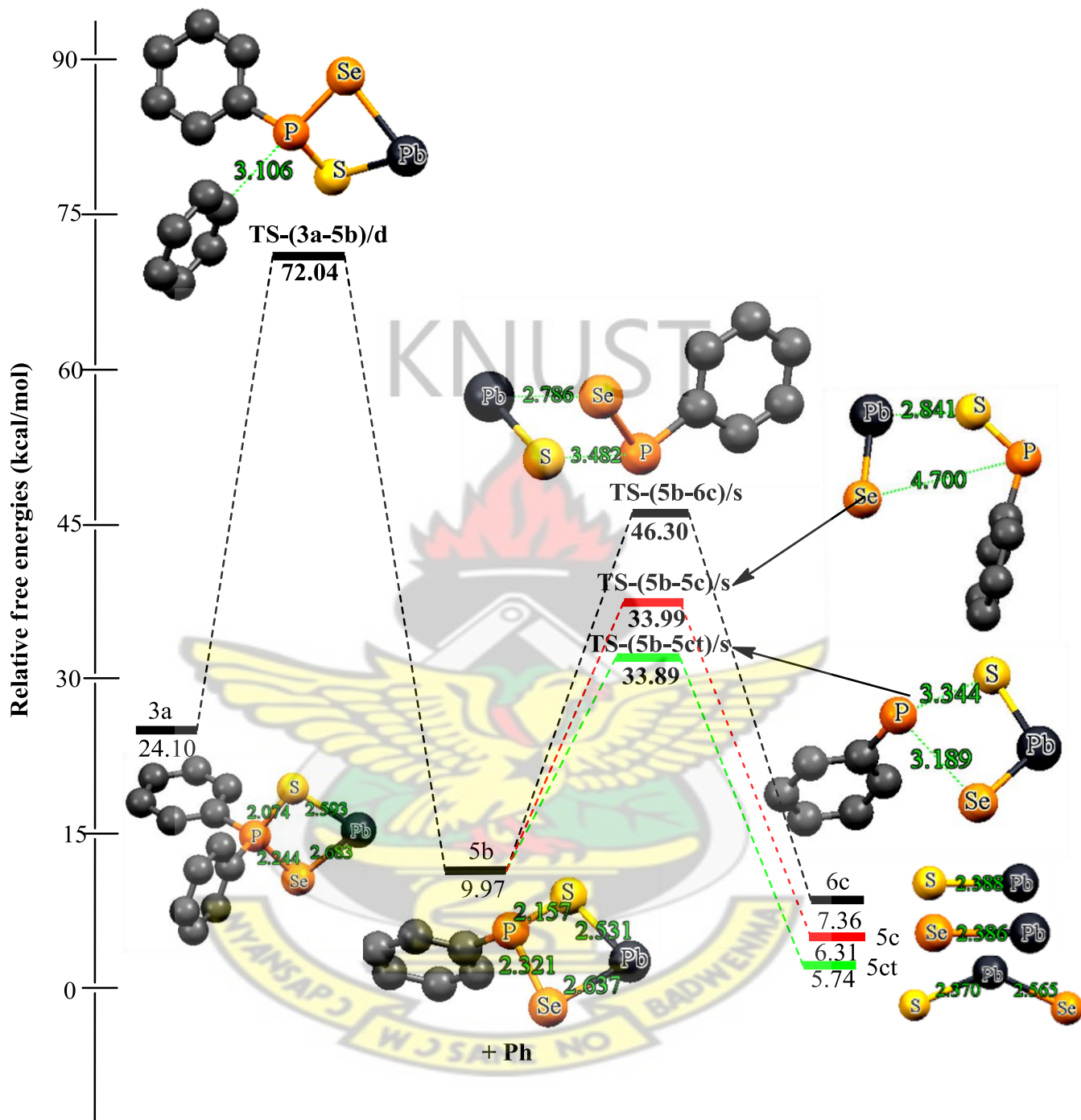


Figure 3.9: Energetics of the unimolecular decomposition pathway (5, 6) at 800 K. The relative free energies are in kcal/mol and bond distances in Å

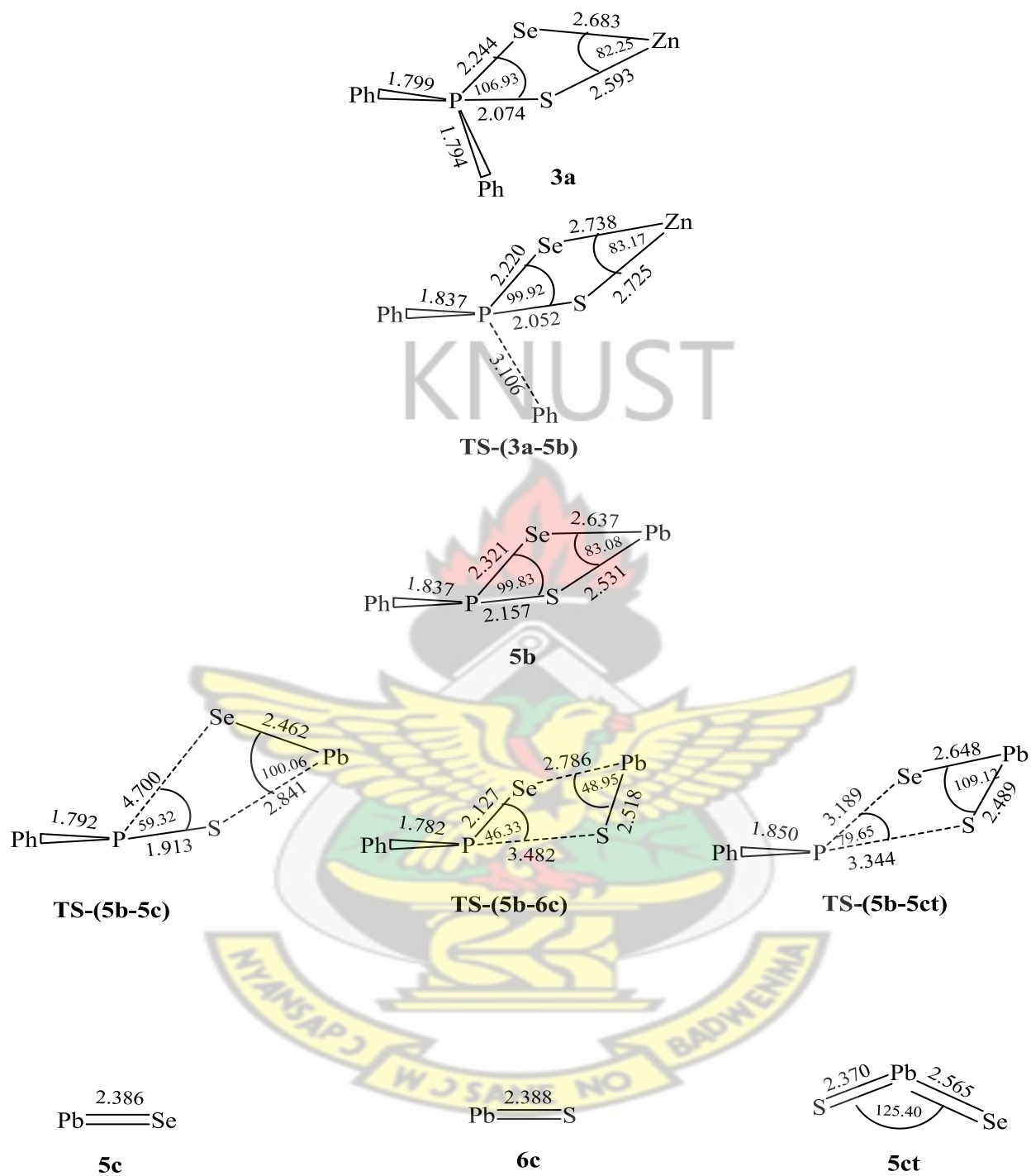


Figure 3.10: Optimized geometrical parameters of the main stationary points involved in the unimolecular decomposition pathway (5, 6). Bond distances in Å and bond angles in degrees

Table 3.2: Calculated rate constants for selected individual steps in the decomposition of Pb[(C<sub>6</sub>H<sub>5</sub>)<sub>2</sub>PSSe]<sub>2</sub> precursor both at room temperature (298.15 K) and at an elevated temperature (800 K)

Reaction pathway	k <sub>uni</sub> (s <sup>-1</sup> )		k <sub>eq</sub>		k <sub>rec</sub> (M s <sup>-1</sup> )	
	298.15 K	800 K	298.15 K	800 K	298.15 K	800 K
1c → 1d	1.76 x 10 <sup>-37</sup>	3.33 x 10 <sup>-6</sup>	1.84 x 10 <sup>2</sup>	6.64 x 10 <sup>14</sup>	3.24 x 10 <sup>-35</sup>	2.21 x 10 <sup>9</sup>
2c → 2d	2.77 x 10 <sup>-41</sup>	2.36 x 10 <sup>-7</sup>	3.40 x 10 <sup>1</sup>	1.27 x 10 <sup>14</sup>	9.42 x 10 <sup>-40</sup>	3.00 x 10 <sup>7</sup>
1c → 1dt	8.41 x 10 <sup>-43</sup>	3.25 x 10 <sup>-8</sup>	5.24 x 10 <sup>-17</sup>	1.28 x 10 <sup>6</sup>	4.41 x 10 <sup>-59</sup>	4.16 x 10 <sup>-2</sup>
2c → 2dt	5.85 x 10 <sup>-37</sup>	9.05 x 10 <sup>-6</sup>	1.47 x 10 <sup>-14</sup>	6.63 x 10 <sup>7</sup>	8.60 x 10 <sup>-51</sup>	6.00 x 10 <sup>2</sup>
3a → 3b	1.02 x 10 <sup>-22</sup>	1.96 x 10 <sup>6</sup>	2.42 x 10 <sup>-13</sup>	1.05	2.47 x 10 <sup>-35</sup>	2.06 x 10 <sup>6</sup>
3a → 4b	9.33 x 10 <sup>-29</sup>	1.13 x 10 <sup>-2</sup>	5.91 x 10 <sup>-15</sup>	5.77 x 10 <sup>-2</sup>	5.51 x 10 <sup>-43</sup>	6.52 x 10 <sup>-4</sup>
3a → 3bt	8.84 x 10 <sup>-43</sup>	6.41 x 10 <sup>-8</sup>	3.80 x 10 <sup>-5</sup>	1.15 x 10 <sup>19</sup>	3.36 x 10 <sup>-47</sup>	7.37 x 10 <sup>11</sup>
5b → 5c	8.06 x 10 <sup>-13</sup>	8.64 x 10 <sup>3</sup>	4.01 x 10 <sup>-15</sup>	2.37 x 10 <sup>-5</sup>	3.23 x 10 <sup>-27</sup>	2.05 x 10 <sup>-1</sup>
5b → 6c	8.88 x 10 <sup>-22</sup>	3.75	4.96 x 10 <sup>-19</sup>	4.03 x 10 <sup>-6</sup>	4.40 x 10 <sup>-40</sup>	1.51 x 10 <sup>-5</sup>
5b → 5ct	9.54 x 10 <sup>-13</sup>	9.21 x 10 <sup>3</sup>	8.84 x 10 <sup>-17</sup>	6.20 x 10 <sup>-5</sup>	8.43 x 10 <sup>-29</sup>	5.71 x 10 <sup>-1</sup>

Hammond's postulate can be interpreted in terms of the position of transition state along the reaction coordinate,  $n_T$ , (Eq. 3.3) as defined by Agmon (Serrano *et al.*, 2008);

$$n_T = \frac{1}{2 - \left(\frac{\Delta G^\ddagger}{\Delta G^\circ}\right)} \quad (3.3)$$

The magnitude of  $n_T$ , indicates the degree of similarity between the transition state and the product (Serrano *et al.*, 2008). According to this equation, the position of the transition state along the reaction coordinate is determined by  $\Delta G^\circ$  (a thermodynamic quantity) and  $\Delta G^\ddagger$  (a kinetic quantity).

The values of  $n_T$  for the thermal decomposition of Pb[(C<sub>6</sub>H<sub>5</sub>)<sub>2</sub>PSSe]<sub>2</sub> precursor is shown in Table

3.3. In fact, the similarity between the reactants, intermediates, and products increases with respect to the reaction in the order of  $5ct > 5c > 6c > 4b > 3b > 1dt-2dt > 3bt > 2d-1d$ , and  $5c > 5ct-6c > 4b > 3b > 1dt > 2dt > 3bt > 2d > 1d$  at  $T = 298.15$  K and 800 K respectively. Therefore, transition state is more closely related to product compare to reactant in energy level and the transition state resembles the product. The results imply that the transition state structures involved in the formation of ternary  $PbSe_xS_{1-x}$  **5ct** and  $PbSe$  **5c** have a larger similarity to the product than the endothermic reactions, the energy level of the transition state is closer to the product compare to reactants, therefore both show resemblance in their structures and such type of transition state are known as late transition state other reactions pathway at  $T = 298.15$  K and 800 K respectively.

Table 3.3: Position of the transition state structures ( $n_T$ ) for selected individual steps

Reaction pathway	298.15 K	800 K
$1c \rightarrow 1d$	0.488826	0.435654
$2c \rightarrow 2d$	0.492922	0.441541
$1c \rightarrow 1dt$	0.587105	0.473961
$2c \rightarrow 2dt$	0.582122	0.463051
$3a \rightarrow 3b$	0.610761	0.499842
$3a \rightarrow 4b$	0.605524	0.507726
$3a \rightarrow 3bt$	0.520994	0.425909
$5b \rightarrow 5c$	0.703481	0.551159
$5b \rightarrow 6c$	0.685320	0.543172
$5b \rightarrow 5ct$	0.739083	0.546260

### 3.5 Conclusion

A number of possible CVD decomposition reactions pathway of  $[\text{Pb}\{(\text{C}_6\text{H}_5)_2\text{PSSe}\}_2]$  single-source precursor was studied using DFT calculations, both at room temperature and elevated temperature. The following conclusions are drawn from the results presented.

1. On the singlet PES, the decomposition of  $(\text{C}_6\text{H}_5)\text{PSSe-Pb-Se}$  intermediate leading to the formation of  $\text{PbSe}$  was thermodynamically favoured, but the reaction is kinetically slow by the highest activation barrier. The unimolecular and bimolecular recombination rate constants were calculated as  $3.33 \times 10^{-6} \text{ s}^{-1}$  and  $2.21 \times 10^9 \text{ s}^{-1}$  at  $T = 800 \text{ K}$  respectively.
2. The calculation indicate that on the singlet PES, the decomposition of  $(\text{C}_6\text{H}_5)\text{PSSe-Pb}$  intermediate leading to  $\text{PbSe}$  formation, is the most plausible pathway. The rate constants were calculated as  $8.06 \times 10^{-13}$  (298.15 K) and  $8.64 \times 10^3 \text{ s}^{-1}$  (800 K).
3. This preferred pathway lends support to both the experimental and theoretical work of Akhtar *et al.* (2011), though their computational prediction of the reaction pathway was based only on thermodynamic considerations.
4. On the doublet PES, the decomposition of  $(\text{C}_6\text{H}_5)_2\text{PSSe-Pb}$  intermediate leading to ternary  $\text{PbSe}_x\text{S}_{1-x}$  formation was thermodynamically favoured, but the reaction is kinetically blocked by the very high activation barrier. This probably explains why experimentally no ternary  $\text{PbSe}_x\text{S}_{1-x}$  products have been observed in the CVD decomposition of  $[\text{Pb}\{(\text{C}_6\text{H}_5)_2\text{PSSe}\}_2]$  single-source precursor (Akhtar *et al.*, 2011). The most plausible pathway leads to the formation of  $\text{PbSe}$ .

5. The value of  $n_T$  for the decomposition of  $(C_6H_5)PSSe-Pb$  reveals that the transition state structure involved in the formation  $PbSe$  has a larger similarity to the product than the other pathways at  $T = 800\text{ K}$ .

KNUST



## References

- Acharya, S., Gautam, U. J., Sasaki, T., Bando, Y., Golan, Y. and Ariga, K. (2008). "Ultrannarrow PbS nanorods with intense fluorescence". *J. Am. Chem. Soc.*, 130: 4594–4595.
- Afzaal, M., Ellwood, K., Pickett, N. L., O'Brien, P., Raftery, J. and Waters, J. (2004). "Growth of lead chalcogenide thin films using single-source precursors". *J. Mater. Chem.*, 14: 1310-1315.
- Akhtar, J., Afzaal, M., Vincent, M., Burton, N., Raftery, J., Hillier, I. and O'Brien, P. (2011). "Understanding the Decomposition Pathways of Mixed Sulphur/Selenium Lead Phosphinato Precursor Explaining the Formation of Lead Selenide". *J. Phys. Chem. C*, 115(34): 16904-16909.
- Benson, S. W. (1960). *The Foundations of Chemical Kinetics*, McGraw-Hill, New York.
- Boudjouk, P., Jarabek, B. R., Simonson, D. L., Seidler, D. J., Grier, D. G., McCarthy, G. J. and Keller, L. P. (1998). "Metal bis(benzylthiolates) - efficient single-source precursors to solid-solutions and nanoparticles of metal sulphides". *Chem. Mater.*, 10: 2358-2364.
- Clark, M., Cramer, R. D. and Opdenbosch, N. V. (1989). "Validation of the general purpose tripos 5.2 force field". *J. Comp. Chem.*, 10: 982-1012.
- Claudio, E. S., Godwin, H. A. and Magyar, J. S. (2003). "Fundamental coordination chemistry, environmental chemistry, and biochemistry of lead(II)," *Prog. Inorg. Chem.*, 51: 1-144.

Cui, D. H., Xu, J., Zhu, T., Paradee, G., Ashok, S. and Gerhold, M. (2006). "Harvest of near infrared light in PbSe nanocrystal-polymer hybrid photovoltaic cells". *Appl. Phys. Lett.*, 88: 183111-183113.

Davidovich, R. L., Stavila, V. and Whitmire, K. H. (2010). "Stereochemistry of lead(II) precursor containing sulphur and selenium donor atom ligands". *Coord. Chem. Rev.*, 254: 2193-2226.

Dunning, T. H., Jr. and Hay, P. J. (1976). *Gaussian basis sets for molecular calculations*, in: H.F. Schaefer III (Ed.), *Modern Theoretical Chemistry*, vol. 3, Plenum, New York, 1-28.

Glasstone, S., Laidler, K. J. and Eyring, H. (1941). *The Theory of Rate Processes*, McGraw-Hill, New York.

Harman, T. C., Taylor, P. J., Walsh, M. P. and LaForge, B. E. (2002). "Quantum dot superlattice thermoelectric materials and devices". *Science*, 297: 2229-2232.

Hay, P. J. and Wadt, W, R. (1985a). "*Ab initio* effective core potentials for molecular calculations. Potentials for the transition metal atoms Sc to Hg". *J. Chem. Phys.*, 82: 270-283.

Hay, P. J. and Wadt, W, R. (1985b). "*Ab initio* effective core potentials for molecular calculations. Potentials for K to Au including the outermost core orbitals". *J. Chem. Phys.*, 82: 299-310.

Murray, C. B., Sun, S., Gaschler, W., Doyle, H., Betley, T. A. and Kagan, C. R. (2001). "Colloidal synthesis of nanocrystals and nanocrystal superlattices". *J. Res. Dev.*, 45(1): 47-56.

- Nguyen, C. Q., Adeogun, A., Afzaal, M., Malik, M. A., O'Brien, P. (2006). "Metal precursor of selenophosphinates from reaction with  $(R_2PSe)_2Se$ :  $[M(R_2PSe_2)_n]$  ( $M = Zn(II), Cd(II), Pb(II), In(III), Ga(III), Cu(I), Bi(III), Ni(II)$ ;  $R = ^iPr, Ph$ ) and  $[Mo(V)_2O_2Se_2(Se_2P^iPr_2)_2]$ ". *Chem Commun.*, 20: 2182–2184.
- Nguyen, C. Q., Afzaal, M., Malik, M. A., Helliwell, M., Raftery, J. and O'Brien, P. (2007). "Novel inorganic rings and materials deposition". *J. Orgmet. Chem.*, 692: 2669-2677.
- Ritch, J. S., Ahmad, K., Afzaal, M., Chivers, T. and O'Brien, P. (2010). "Epitaxial CdTe Rods on Au/Si Islands from a Molecular Compound". *Inorg. Chem.*, 49: 1158–1205.
- Rogach, A. L., Eychmüller, A., Hickey, S. G. and Kershaw, S. V. (2007). "Infrared Emitting Colloidal Nanocrystals: Synthesis, Assembly, Spectroscopy, and Applications". *Small*, 3: 536-557.
- Schaller, R. D., Petruska, M. A. and Klimov, V. I. (2003). "Tunable near-Infrared optical gain and amplified spontaneous emission using PbSe nanocrystals". *J. Phys. Chem. B*, 107: 13765-13768.
- Serrano, A. J., Llorona, M., Cordova, T. and Chuchani, G. (2008). "Theoretical calculations of the thermal decomposition kinetics of several tert-nitroalkanes in the gas phase". *J. Mol. Struct.*, 859: 69-72.
- Shchennikov, V. V. and Ovsyannikov, S. V. (2003). "Thermoelectric power, magnetoresistance of lead chalcogenides in the region of phase transitions under pressure". *Solid State Commun.*, 126(7): 373-378.

Shimoni-Livny, L., Glusker, J. P. and Bock, C. W. (1998). "Lone Pair Functionality in Divalent Lead Compounds". *Inorg. Chem.*, 37: 1853-1867.

*Spartan*, Waefunction, Inc.; 18401 Von Karman Ave., # 370, Irvine, CA, 92715, USA.

Trindade, T., Monteiro, O. C., O'Brien, P. and Motevalli, M. (1999). "Synthesis of PbSe nanocrystallites using a single-source method. The X-ray crystal structure of lead(II) diethyldiselenocarbamate". *Polyhedron*, 18: 1171-1175.

Wadt, W. R. and Hay, P. J. (1985). "Ab initio effective core potentials for molecular calculations. Potentials for main group elements Na to Bi". *J. Chem. Phys.*, 82: 284-298.

Wang, S., Zhang, X., Mao, X., Zeng, Q., Xu, H., Lin, Y., Chen, W. and Liu, G. (2008). "Electrochemical immunoassay of carcinoembryonic antigen based on a lead sulphide nanoparticle label". *Nanotech.*, 19: 435-501.

Zhang, Y. C., Qiao, T., Hu, X. Y., Wang, G. Y. and Wu, X. (2005). "Phase-controlled synthesis of ZnS nanocrystallites by mild solvothermal decomposition of an air-stable single-source molecular precursor". *J. Cryst. Growth*, 277: 518-523

## CHAPTER FOUR

### DENSITY FUNCTIONAL THEORY (DFT) STUDY OF THE DECOMPOSITION OF Pb[(<sup>1</sup>Pr)<sub>2</sub>PSSe]<sub>2</sub> SINGLE-SOURCE PRECURSOR FOR THE CHEMICAL VAPOUR DEPOSITION OF BINARY AND TERNARY LEAD CHALCOGENIDES

#### Abstract

The plausible pathways involved in the thermal decomposition of Pb[(<sup>1</sup>Pr)<sub>2</sub>PSSe]<sub>2</sub> precursor in the gas phase, both at room temperature (298.15 K) and at an elevated temperature (800 K) were studied using density functional theory at the MO6/6-31G\* levels of theory with the Los Alamos quasi-relativistic effective core potential (LAN2DZ) to model the non-negligible relativistic effects in lead. The results reveal that the steps that lead to PbS formation is the most dominant decomposition pathway than those that lead to PbSe and ternary PbSe<sub>x</sub>S<sub>1-x</sub> on both the doublet and singlet potential energy surface. Thermodynamically, the steps that lead to PbSe formation are more favourable than those that lead to PbS and ternary PbSe<sub>x</sub>S<sub>1-x</sub> formation on the singlet PES, while those that lead to PbSe<sub>x</sub>S<sub>1-x</sub> formation are more favourable than those that lead to PbSe and PbS formation on the doublet PES. Density functional theory calculations of the formation of ternary PbSe<sub>x</sub>S<sub>1-x</sub> are consistent with a dominant role on thermodynamic grounds rather than kinetic ones in controlling the material formed during the deposition process.

**Keywords:** Density functional theory, thermal decomposition, precursor, plausible pathways, potential energy surface

## 4.1 Introduction

Lead chalcogenides, PbE (E = S, Se, Te), as thin films have been of considerable interest (Afzaal *et al.*, 2004). One driving force is the recently discovered phenomenon of multiple exciton generation (MEG) (Ellingson *et al.*, 2005), which could ultimately lead to more efficient solar energy conversion (Luther *et al.*, 2008; Beard and Ellingso, 2008). The chemistry of dichalcogenophosphinates has been of considerable interest because complexes of the type  $[M(E_2PR_2)_2]$  (R = <sup>i</sup>Pr or Ph; E = S and/or Se) can be readily prepared because both the donor atoms and alkyl groups can be easily varied.

Lead sulphide nanoparticles may be useful in electroluminescent devices such as light-emitting diodes. In addition, the exceptional third-order non-linear optical properties of PbS nanoparticles have potential applications in high-speed switching (Colvin *et al.*, 1994). This material is also potentially useful for making devices that require small band-gap semiconductors with optical absorption and emission in the red and near-infrared region of the spectrum.

The thermal decomposition of metal-organic compounds can occur by exploring several reaction mechanisms and the main problem is how to control reaction pathway leading to decomposition of the precursor to deposit thin film material of desired phase. The film structure and composition are governed by other factors: chemical kinetics, surface and gas diffusion and mass transfer. To reveal important details of potential energy surfaces for the types of reactions which may occur in  $Pb[(^iPr)_2PSSe]_2$  single-source precursor, transition states and intermediate complexes for the given reactions paths were computed.

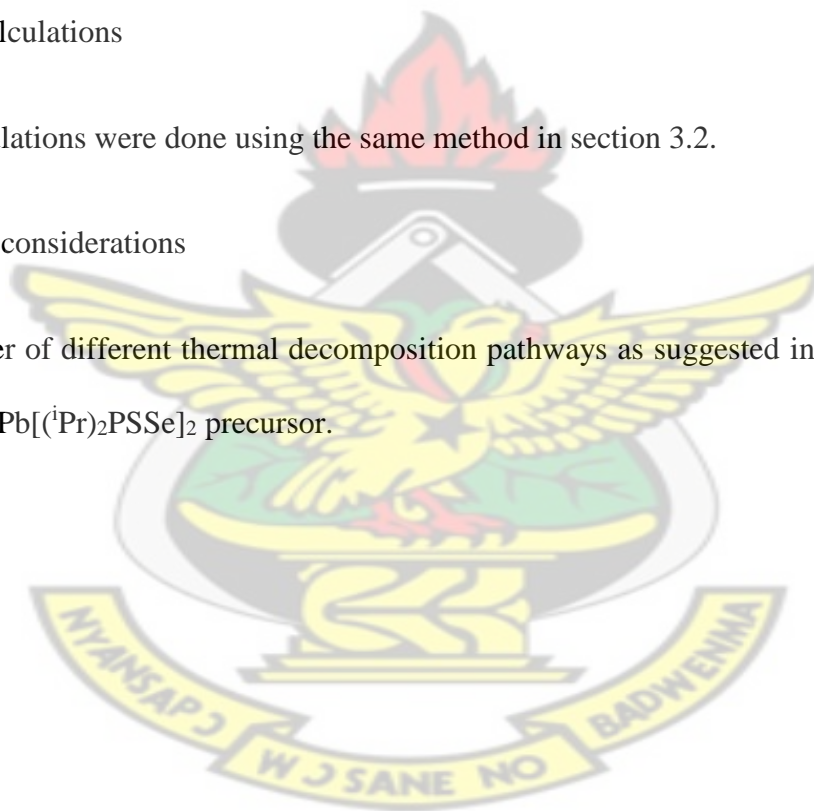
Akhtar *et al.* (2011) have used the results of density functional theory study to suggest that the formation of PbSe in CVD may involve more than one mechanism but the steps that lead to of PbSe are somewhat more favourable on thermodynamic grounds, than those that lead to PbS formation. The aim of this work is to extend the work of Akhtar *et al.* (2011) by employing density functional theory calculations at the MO6/LACVP\* level of theory to explore the thermal decomposition of  $\text{Pb}[(^1\text{Pr})_2\text{PSSe}]_2$  precursor and to investigate the possible mechanistic channels involved in the formation of lead chalcogenides.

#### 4.2 Details of calculations

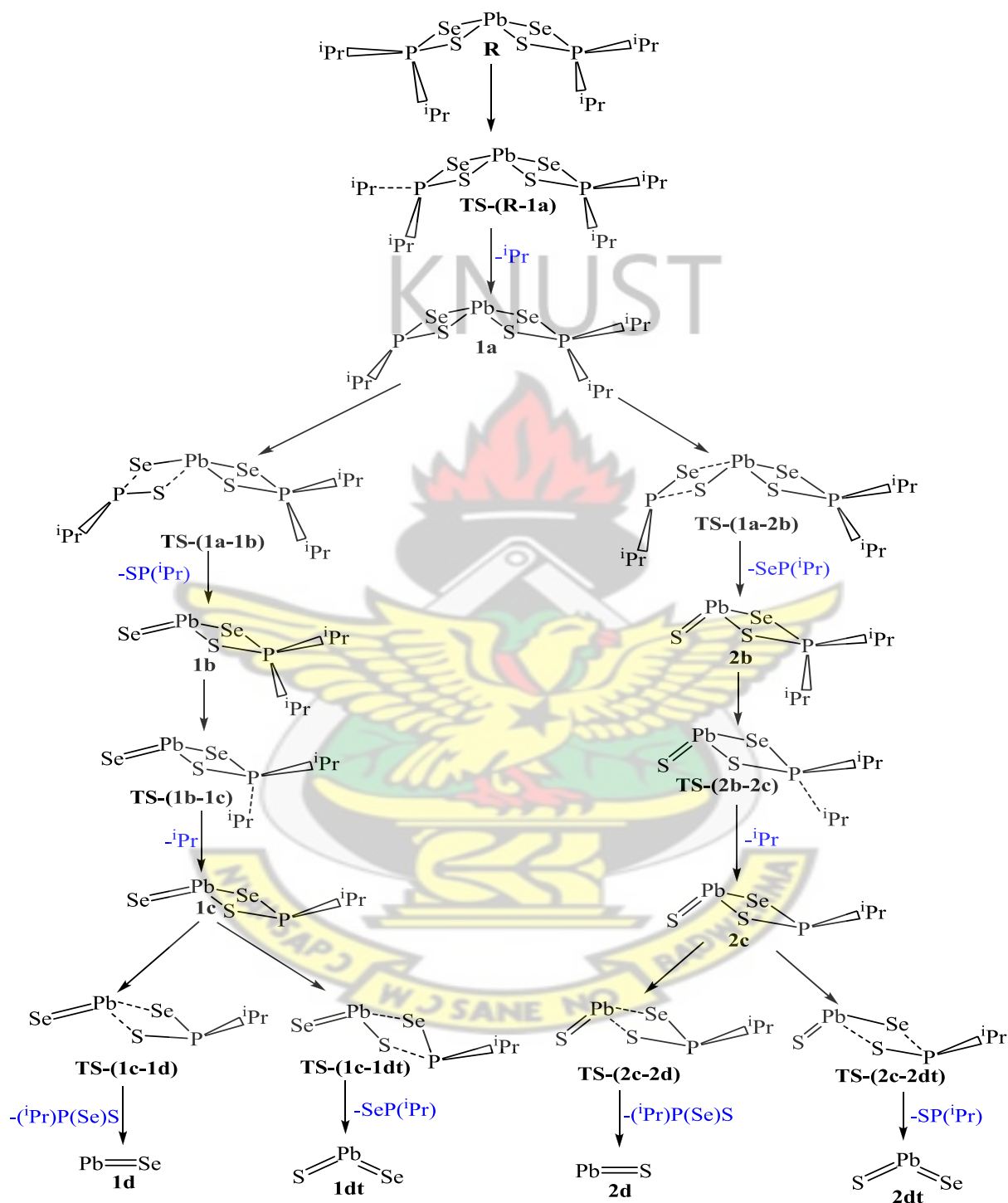
All calculations were done using the same method in section 3.2.

#### 4.3 Mechanistic considerations

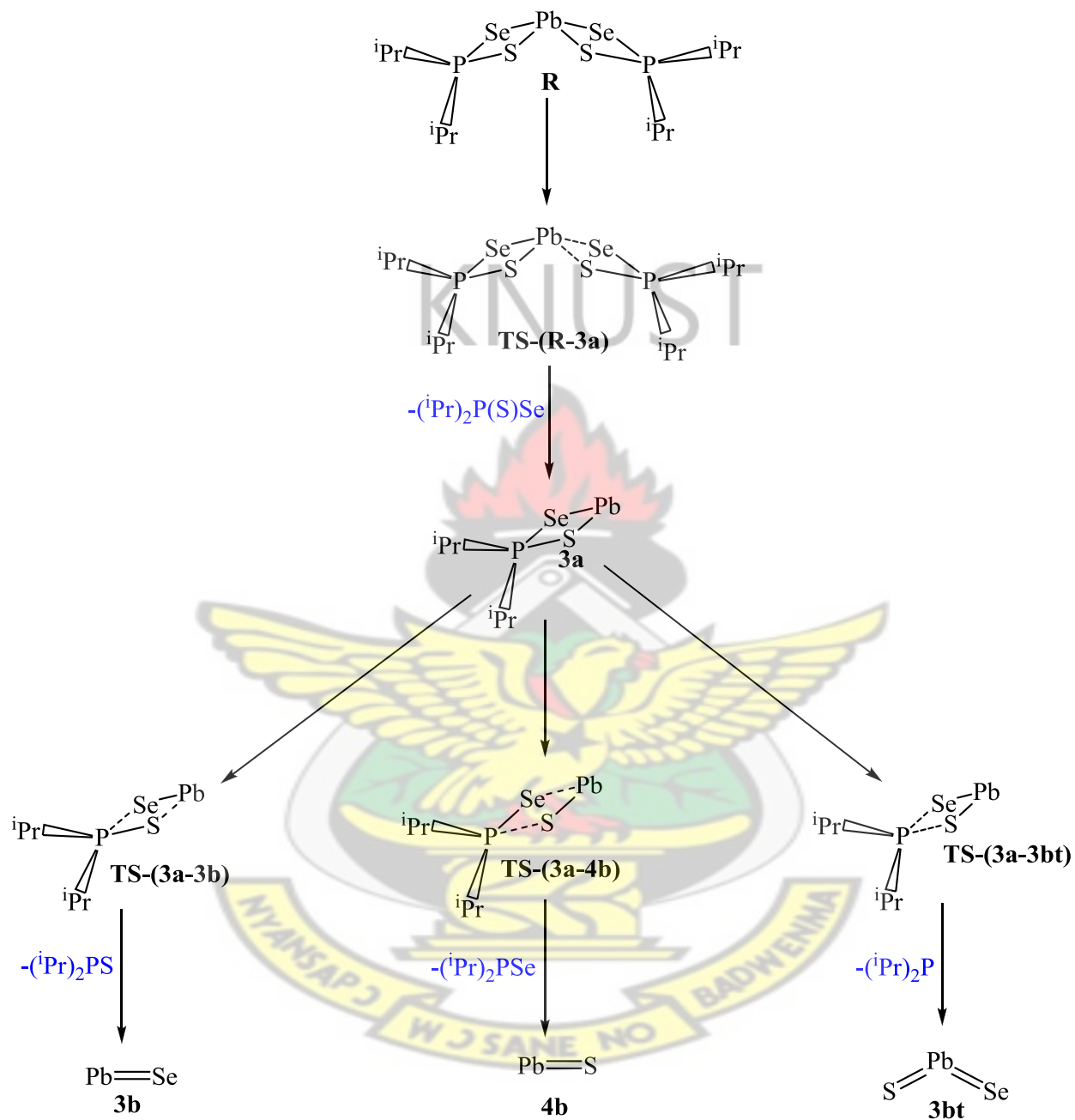
A number of different thermal decomposition pathways as suggested in section 3.3 were investigated for  $\text{Pb}[(^1\text{Pr})_2\text{PSSe}]_2$  precursor.



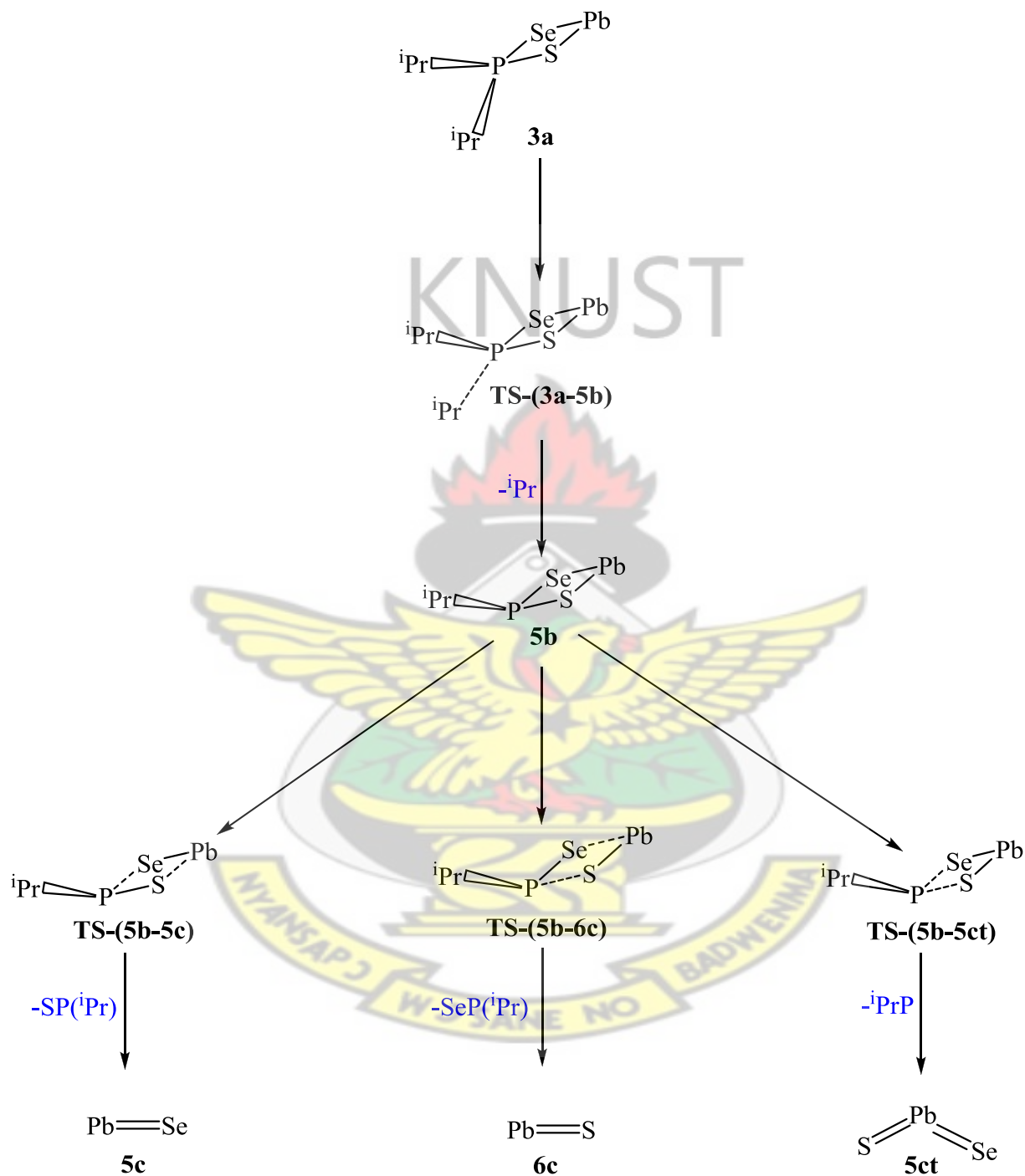
Scheme 4.1: Decomposition pathway (1, 2) of  $\text{Pb}[(i\text{Pr})_2\text{PSSe}]_2$  precursor



Scheme 4.2: Decomposition pathway (3, 4) of  $\text{Pb}[(i\text{Pr})_2\text{PSSe}]_2$  precursor



Scheme 4.3: Decomposition pathway (5, 6) of  $\text{Pb}[(i\text{Pr})_2\text{PSSe}]_2$  precursor



## 4.4 Results and Discussion

### 4.4.1 Optimized Geometry of Pb[(<sup>i</sup>Pr)<sub>2</sub>PSSe]<sub>2</sub> precursor

Data for the optimized geometry of Pb[(<sup>i</sup>Pr)<sub>2</sub>PSSe]<sub>2</sub> precursor was shown in Table 4.1. Lead has a distorted square pyramidal geometry with the ligand bond angles of 75.99° and 76.28° which are smaller than the perfect square planar angle, but the angles are slightly wider than those in the Pb[(C<sub>6</sub>H<sub>5</sub>)<sub>2</sub>PSSe]<sub>2</sub> precursor analogue. The two sulphur and two selenium atoms form the base of the pyramid with lone pair occupying the axial position. The density functional theory (DFT) geometry optimization of Pb[(<sup>i</sup>Pr)<sub>2</sub>PSSe]<sub>2</sub> precursor has Pb-S bond length at 2.83 Å, as expected, shorter than the bond length of Pb-Se (2.90 Å). The significant disparity in the Pb–Se bond distance at 3.01 Å suggests a stereochemical influence from the lone pair on the metal centre. The average bond angle around S/Se-Pb-S/Se is 95.62°, which are similar to the values in related lead dithiocarbamates (Afzaal *et al.*, 2004). The non-coordinating S and Se atoms are each proximate to the Pb(II) atom, giving rise to distortions from the ideal geometry as evident in the wide S-Pb-Se bond angle of 153.81°.

Table 4.1: Selected bond lengths (Å) and bond angles (°) of Pb[(iPr)<sub>2</sub>PSSe]<sub>2</sub> precursor

Bonds	length(Å)	length(Å)	bonds	angles (°)	angles (°)
		X-ray			X-ray
		crystallography <sup>a</sup>			crystallography <sup>a</sup>
P-S	2.022	2.190(3)	P-Se-Pb	85.97	89.10(3)
P-Se	2.230	2.151(6)	P-S-Pb	85.58	84.00(18)
S-P	2.058	-	S-Pb-Se	75.99	94.10(7)
Se-P	2.193	-	Se-Pb-S	76.28	75.62(19)
Pb-S	2.951	2.903(6)	Se-Pb-Se	84.87	89.10(3)
Pb-Se	2.789	3.017(5)	S-Pb-S	87.66	84.00(18)
Se-Pb	3.010	3.044(2)	S-Pb-Se	153.81	154.40(2)
S-Pb	2.715	2.812(8)	Se-Pb-S	95.14	94.40(2)

<sup>a</sup> (Akhtar *et al.*, 2011)

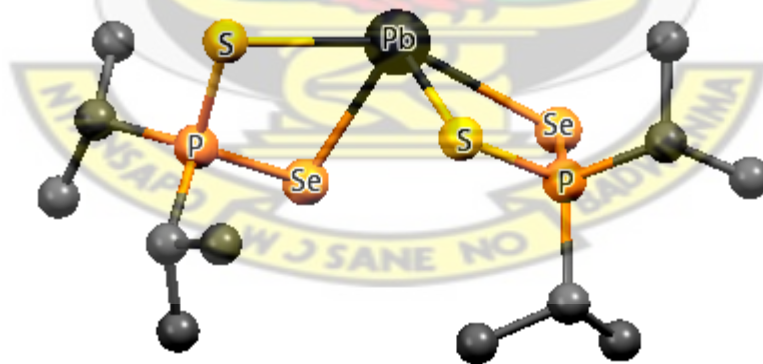


Figure 4.1: Optimized geometry of Pb[(iPr)<sub>2</sub>PSSe]<sub>2</sub> single-source precursor

#### 4.4.2 Overall Decomposition of $\text{Pb}[(^i\text{Pr})_2\text{PSSe}]_2$ precursor

The reaction mechanisms involved in gas phase decomposition of single-source precursor were studied by considering the energetics of the reactants, transition states, intermediates, and products of the given reactions using density functional theory method at the MO6/6-31G\* level of theory. The optimized structures have shown that the gas phase decomposition into the observed products involve a four-membered cyclic transition state. The Gibbs free energies have been computed at  $T = 298.15 \text{ K}$  and  $800 \text{ K}$ , which is the experimental temperature for the proposed reaction mechanisms in  $\text{Pb}[(\text{C}_6\text{H}_5)_2\text{PSSe}]_2$  single-source precursor. Figures 4.2 and 4.3 show the energy profile of the reaction pathway (1, 2) as well as the optimized structures of the main stationary points (reactants, transition states, intermediates and products). The full set of optimized structures for all the systems reported is shown in Figs. 4.4, 4.7 and 4.10. Literature survey reveals that there are no experimental or theoretical data available to compare these energy barriers.

The first mechanism involved the initial loss of isopropyl radical to form **1a** intermediate on the doublet PES. The activation free energy barrier involved in this process was calculated as  $+77.98 \text{ kcal/mol}$  ( $298.15 \text{ K}$ ) and  $+77.25 \text{ kcal/mol}$  ( $800 \text{ K}$ ) with a reaction free energy of  $+53.76 \text{ kcal/mol}$  ( $298.15 \text{ K}$ ) and  $+24.51 \text{ kcal/mol}$  ( $800 \text{ K}$ ).

The subsequent step is either the loss of  $\text{SP}(^i\text{Pr})$  or  $\text{SeP}(^i\text{Pr})$  and conversion of **1a** intermediate forms either  $(^i\text{Pr})_2\text{PSSe-Pb-Se}$  **1b** and  $(^i\text{Pr})_2\text{PSSe-Pb-S}$  **2b** intermediates on the doublet PES through the transition state **TS-(1a-1b)** and **TS-(2a-2b)** respectively. The activation free energy barrier for **1b** and **2b** were calculated as  $+6.00 \text{ kcal/mol}$  ( $298.15 \text{ K}$ ) and  $+32.78 \text{ kcal/mol}$  ( $800 \text{ K}$ ), and  $+9.72 \text{ kcal/mol}$  ( $298.15 \text{ K}$ ) and  $+36.30 \text{ kcal/mol}$  ( $800 \text{ K}$ ) respectively and a

reaction free energy of -26.75 kcal/mol (298.15 K) and -28.53 kcal/mol (800 K) for **1b**, and -17.84 kcal/mol (298.15 K) and -20.67 kcal/mol (800 K) for **2b**.

The (*i*Pr)<sub>2</sub>PSSe-Pb-Se **1b** and (*i*Pr)<sub>2</sub>PSSe-Pb-S **2b** intermediates were further decompose to form (*i*Pr)PSSe-PbSe **1c** and (*i*Pr)PSSe-PbSe **2c** intermediates on the singlet PES through a transition state **TS-(1b-1c)** and **TS-(2b-2c)** after a loss of isopropyl radical. The activation free energy barrier for (*i*Pr)PSSe-Pb-Se **1c** and (*i*Pr)PSSe-Pb-S **2c** were computed as +44.22 kcal/mol (298.15 K) and +74.49 kcal/mol (800 K), and +34.35 kcal/mol (298.15 K) and +62.95 kcal/mol (800 K) respectively and endergonic by 25.21 kcal/mol (298.15 K) and 29.53 kcal/mol (800 K) for **1c**, and 10.83 kcal/mol (298.15 K) and 14.36 kcal/mol (800 K) for **2c**.

The **1c** intermediate can go through two different pathways to form either PbSe or PbSe<sub>x</sub>S<sub>1-x</sub> on the singlet PES. The decomposition of (*i*Pr)PSSe-Pb-Se **1c** intermediate to form PbSe **1d** along the transition state **TS-(1c-1d)** has an activation free energy barrier of +23.51 kcal/mol (298.15 K) and +50.16 kcal/mol (800 K), and reaction free energy of -51.44 kcal/mol (298.15 K) and -39.37 kcal/mol (800 K). The optimized geometry of **TS-(1c-1d)** further reveals the elongation of Pb-Se bond length from 2.596 to 3.528 Å and Pb-S bond length from 2.490 to 3.666 Å. The (*i*Pr)PSSe-Pb-Se intermediate **1c** was further decompose to form ternary PbSe<sub>x</sub>S<sub>1-x</sub> **1dt**. The activation free energy barrier involved in the formation ternary PbSe<sub>x</sub>S<sub>1-x</sub> **1dt** along the transition state **TS-(1c-1dt)** was computed as +37.43 kcal/mol (298.15 K) and +63.79 kcal/mol (800 K) and exergonic by 23.04 kcal/mol (298.15) and 23.96 kcal/mol (800 K). The optimized geometry of **TS-(1c-1dt)** further reveals the elongation of Pb-Se bond length from 2.596 to 3.183 Å and P-S bond length from 2.159 to 3.505 Å.

The (*i*Pr)PSSe-Pb-S intermediate **2c** can also decompose through a transition state **TS-(2c-**

**2d**) to form PbS **2d** with an activation free energy barrier of +24.24 kcal/mol (298.15 K) and +52.78 kcal/mol (800 K). The formation of PbS **2d** was exergonic by 45.62 kcal/mol (298.15 K) and 33.95 kcal/mol (800 K) on the singlet PES. The optimized geometry of **TS-(2c-2d)** further reveals the elongation of Pb-S bond length from 2.488 to 3.510 Å and Pb-Se bond length from 2.589 to 3.664 Å.

The transition state **TS-(2c-2dt)** along the (<sup>i</sup>Pr)PSSe-Pb-S **2c** pathway to form ternary PbSe<sub>x</sub>S<sub>1-x</sub> **2dt** has an activation free energy barrier of +25.06 kcal/mol (298.15 K) and +53.59 kcal/mol (800 K), and exergonic by 20.98 kcal/mol (298.15 K) and 21.26 kcal/mol (800 K) on the singlet PES. The optimized geometry of **TS-(2c-2dt)** further reveals the elongation of Pb-S bond length from 2.448 to 2.946 Å and P-Se bond length from 2.314 to 2.764 Å.

On the singlet PES, the decomposition of <sup>i</sup>PrPSSe-Pb-Se/-Se intermediates reveal that, the **[1d]** dissociation of <sup>i</sup>PrP(Se)S from <sup>i</sup>PrPSSe-Pb-Se intermediate to form PbSe has the lowest barrier (50.16 kcal/mol) compared to **[1dt]** dissociation from <sup>i</sup>PrPSSe-Pb-Se intermediate (63.79 kcal/mol), **[2dt]** dissociation from <sup>i</sup>PrPSSe-Pb-S intermediate (53.59 kcal/mol), **[2d]** dissociation from <sup>i</sup>PrPSSe-Pb-S intermediate (52.78 kcal/mol). On the reaction PES, **2d** decomposition pathway to form PbS is the most stable species (39.37 kcal/mol exergonic). Kinetically the most favoured pathway is the **1d** decomposition pathway and in terms of equilibrium thermodynamic, the **2d** decomposition pathway is the favoured pathway. The rate constants along **1d** dissociation pathway is  $1.90 \times 10^{-43} \text{ s}^{-1}$  (298.15) and  $3.55 \times 10^{-8} \text{ s}^{-1}$  (800 K).

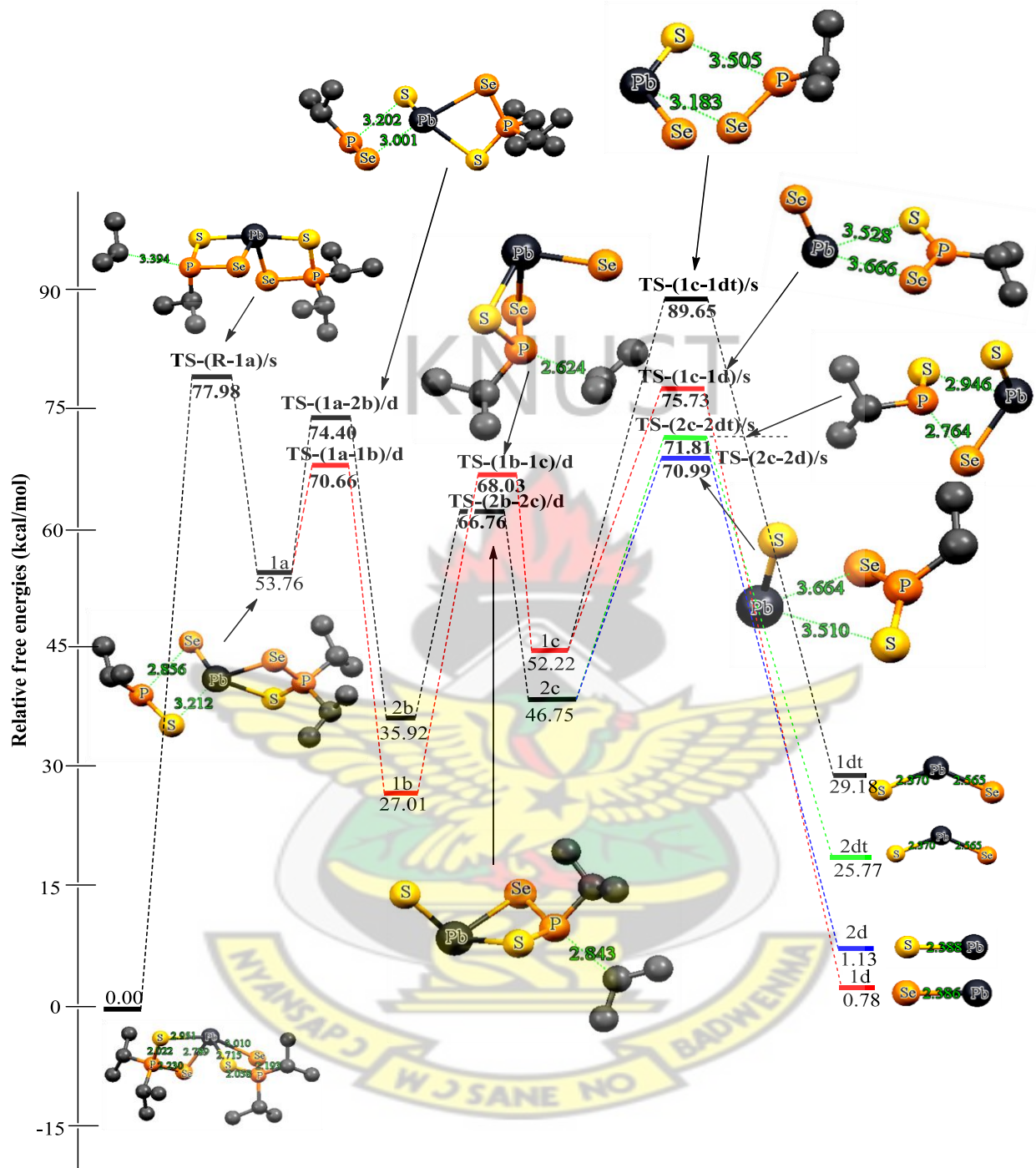


Figure 4.2: Energetics of the unimolecular decomposition pathway (1, 2) at 298.15 K. The relative free energies are in kcal/mol and bond distances in Å

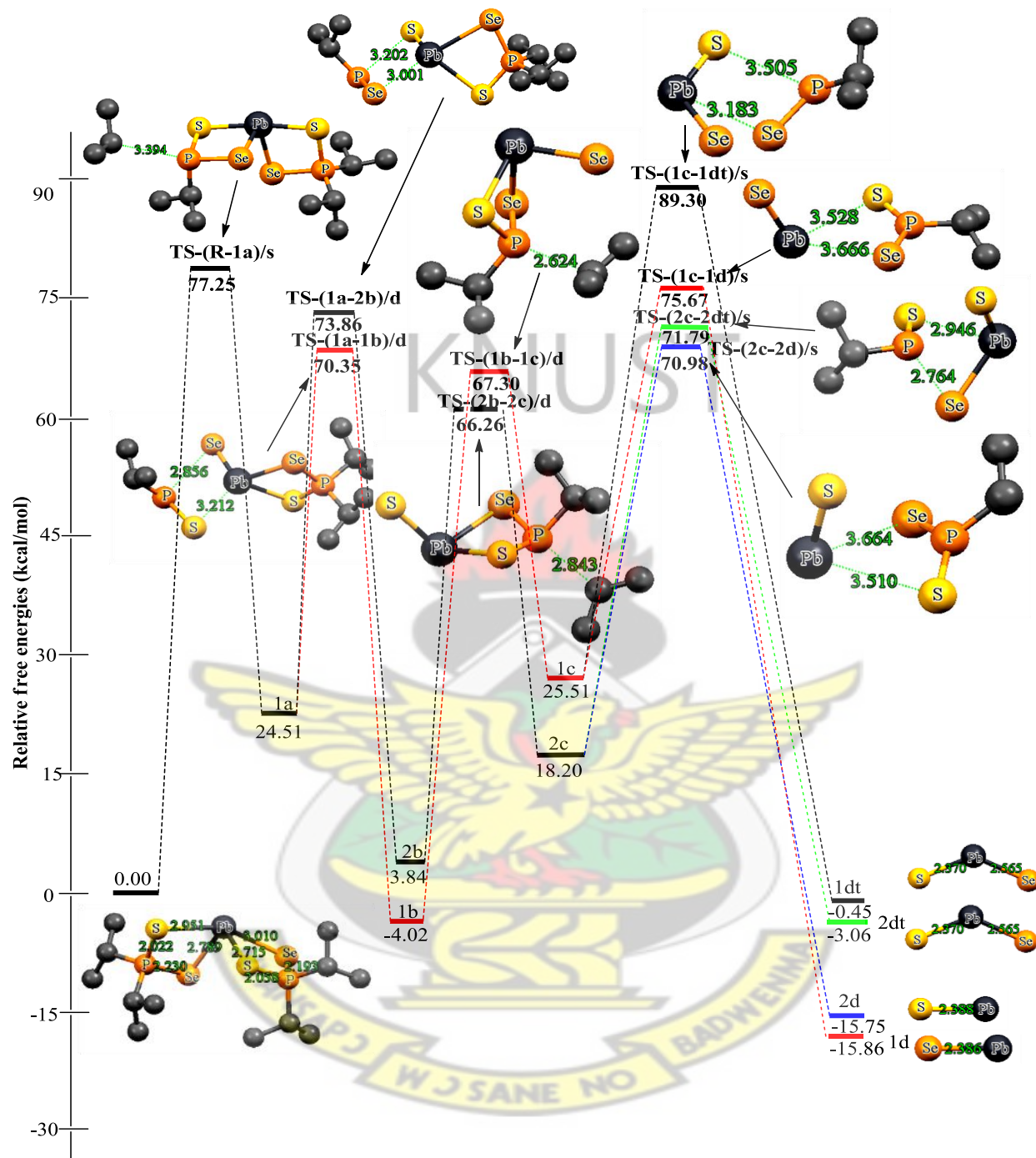


Figure 4.3: Energetics of the unimolecular decomposition pathway (1, 2) at 800 K. The relative free energies are in kcal/mol and bond distances in Å

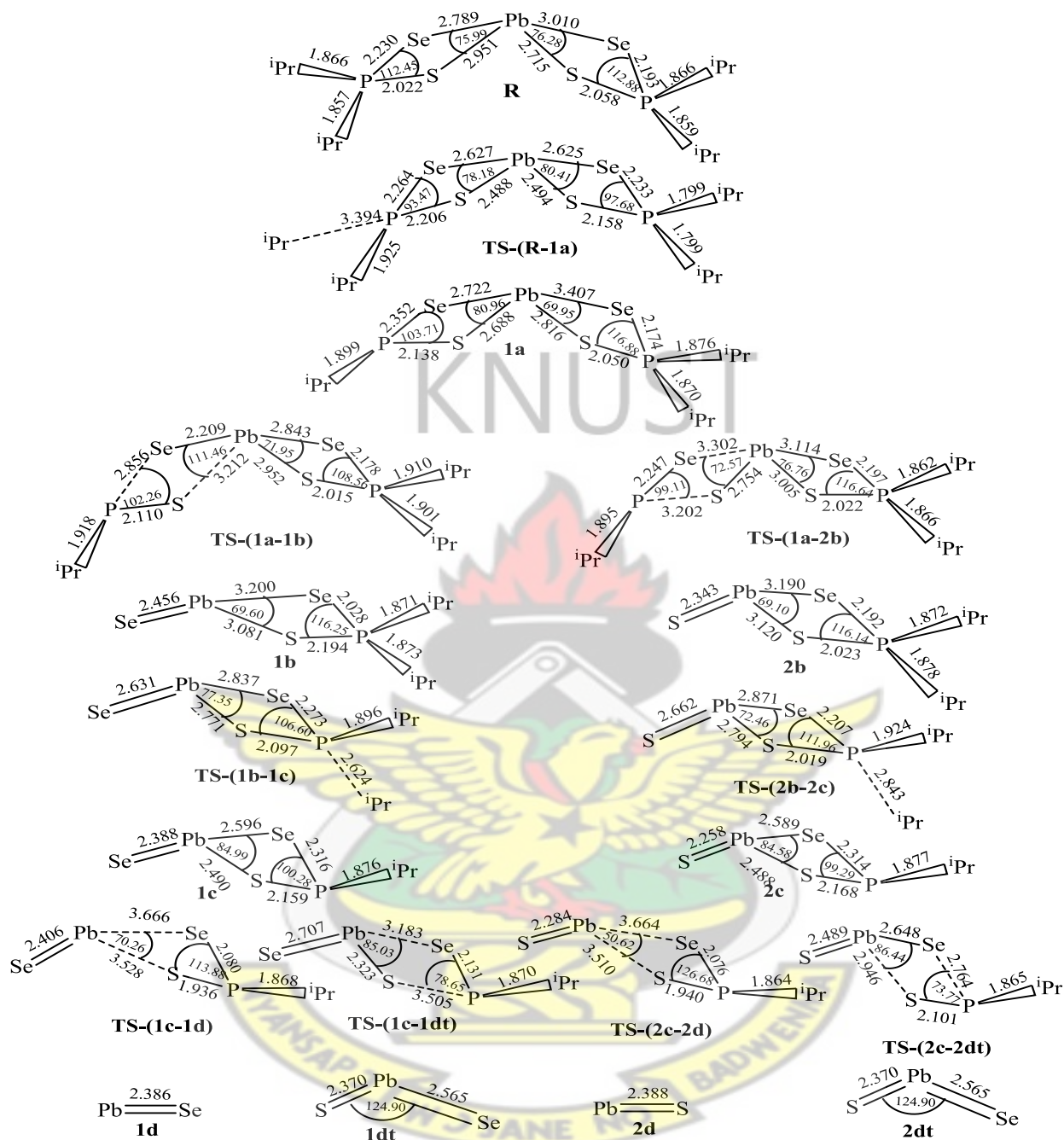


Figure 4.4: Optimized geometrical parameters of the main stationary points involved in the unimolecular decomposition pathway (1, 2). Bond distances in Å and bond angles in degrees

The reaction pathways involved in the decomposition of (<sup>i</sup>Pr)<sub>2</sub>PSSe-Pb intermediate were studied on the doublet surface by considering the energetics of the reactants, intermediates and products. The potential energy surface for all the possible unimolecular pathways involved in decomposition of (<sup>i</sup>Pr)<sub>2</sub>PSSe-Pb intermediate are given in Figures 4.5 and 4.6.

The decomposition of Pb[(<sup>i</sup>Pr)<sub>2</sub>PSSe]<sub>2</sub> precursor to form (<sup>i</sup>Pr)<sub>2</sub>PSSe-Pb **3a** intermediate on the doublet PES, has an activation free energy barrier of +59.78 kcal/mol (298.15 K) and +58.15 kcal/mol (800 K) and endergonic by 57.91 kcal/mol (298.15 K) and 24.10 kcal/mol (800 K).

The formation of PbSe **3b** on the doublet PES through a transition state **TS-(3a-3b)** has an activation free energy barrier of -16.97 kcal/mol (298.15 K) and +17.10 kcal/mol (800 K) and reaction free energy of -46.45 kcal/mol (298.15 K) and -29.09 kcal/mol (800 K). The optimized geometry of **TS-(3a-3b)** further reveals the elongation of Pb-S length from 2.598 to 2.946 Å and P-Se bond length from 2.241 to 2.934 Å.

Also, the activation free energy barrier involved in the formation of PbS **4b** through a transition state **TS-(3a-4b)** was -17.59 kcal/mol (298.15 K) and +16.47 kcal/mol (800 K) with a reaction free energy of -41.84 kcal/mol (298.15 K) and -25.11 kcal/mol (800 K) on the doublet PES. The calculated rate constants showed that PbSe formation was kinetically more favourable with unimolecular and recombination rate constants of  $1.38 \times 10^2 \text{ s}^{-1}$  and  $3.45 \times 10^{-3} \text{ s}^{-1}$  at T = 800 K respectively. The optimized geometry of **TS-(3a-4b)** further reveals the elongation of Pb-Se bond length from 2.691 to 3.294 Å and P-S bond length from 2.072 to 3.485 Å.

The transition state energies involved in the decomposition of (<sup>i</sup>Pr)<sub>2</sub>PSSe-Pb intermediate to form either PbS or PbSe was lower than the free energy of the intermediate molecule at T =

298.15 K. Thus these calculations predict that in the gas phase, PbSe or PbS decomposition pathway is likely to occur without a barrier at  $T = 298.15$  K.

Decomposition of  $(i\text{Pr})_2\text{PSSe-Pb } \mathbf{3b}$  intermediate was further explored to access the ternary nature of  $(i\text{Pr})_2\text{PSSe-Pb}$  radical on the doublet PES. The activation free energy barrier involved in the formation of ternary  $\text{PbSe}_x\text{S}_{1-x}$  through a transition state **TS-(3a-3bt)** has been computed as +25.86 kcal/mol (298.15 K) and +59.62 kcal/mol (800 K) with a reaction free energy of -62.36 kcal/mol (298.15 K) and -59.23 kcal/mol (800 K). The optimized geometry of **TS-(3a-3bt)** further reveals the elongation of P-S bond length from 2.072 to 2.890 Å and P-Se bond length from 2.241 to 2.962 Å.

Although the free energy involved in the formation of ternary  $\text{PbSe}_x\text{S}_{1-x}$  was more exergonic than PbSe and PbS, however, converting  $(i\text{Pr})_2\text{PSSe-Pb}$  intermediate into ternary  $\text{PbSe}_x\text{S}_{1-x}$  require a very high activation free energy barrier at  $T = 800$  K, hence ternary  $\text{PbSe}_x\text{S}_{1-x}$  formation is not a likely product from the decomposition of  $(i\text{Pr})_2\text{PSSe-Pb}$  intermediate. The unimolecular and recombination rate constants were calculated as  $2.24 \times 10^{-10} \text{ s}^{-1}$  and  $8.89 \times 10^{-46} \text{ s}^{-1}$  at  $T = 800$  K respectively.

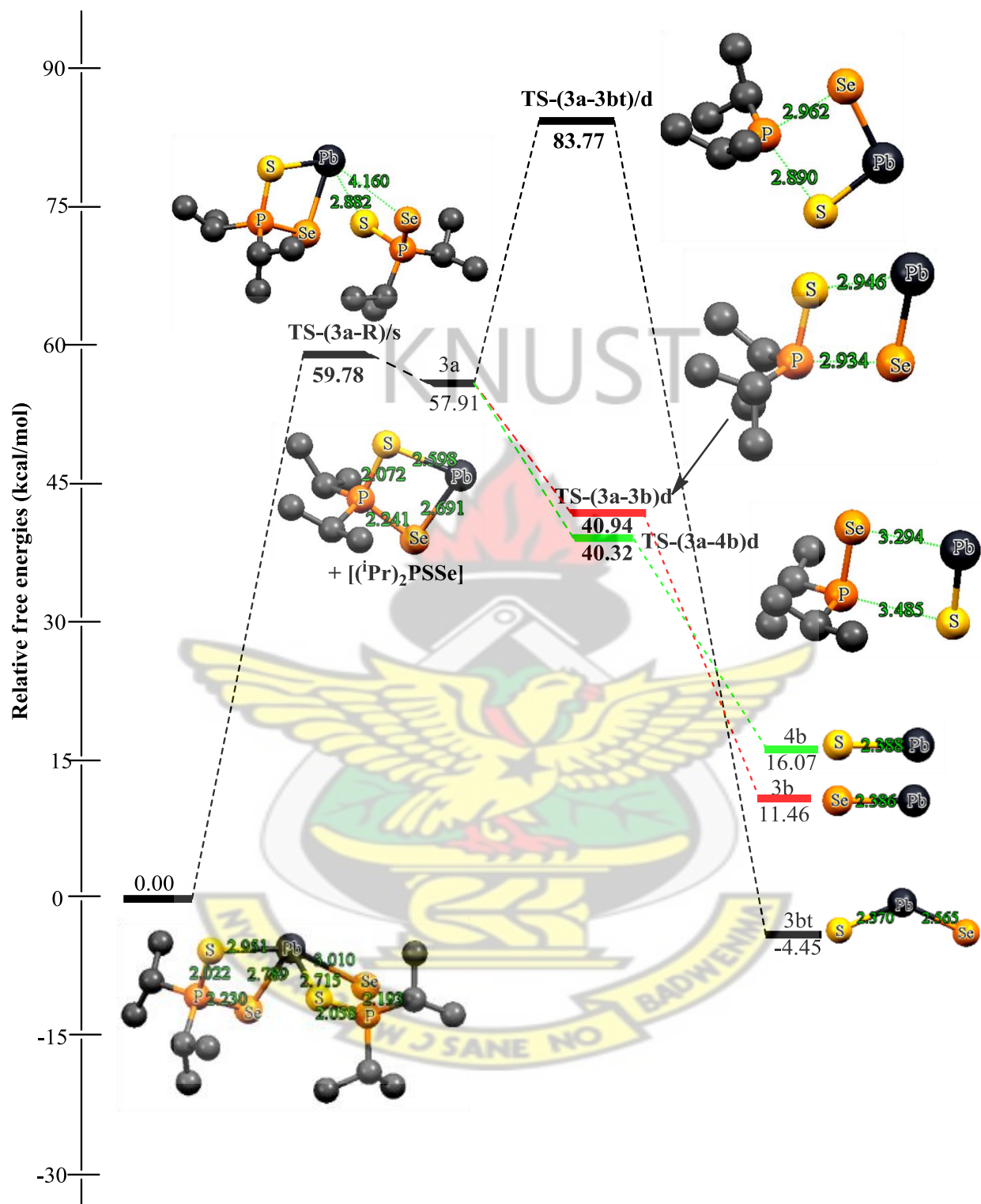


Figure 4.5: Energetics of the unimolecular decomposition pathway (3, 4) at 298.15 K. The relative free energies are in kcal/mol and bond distances in Å

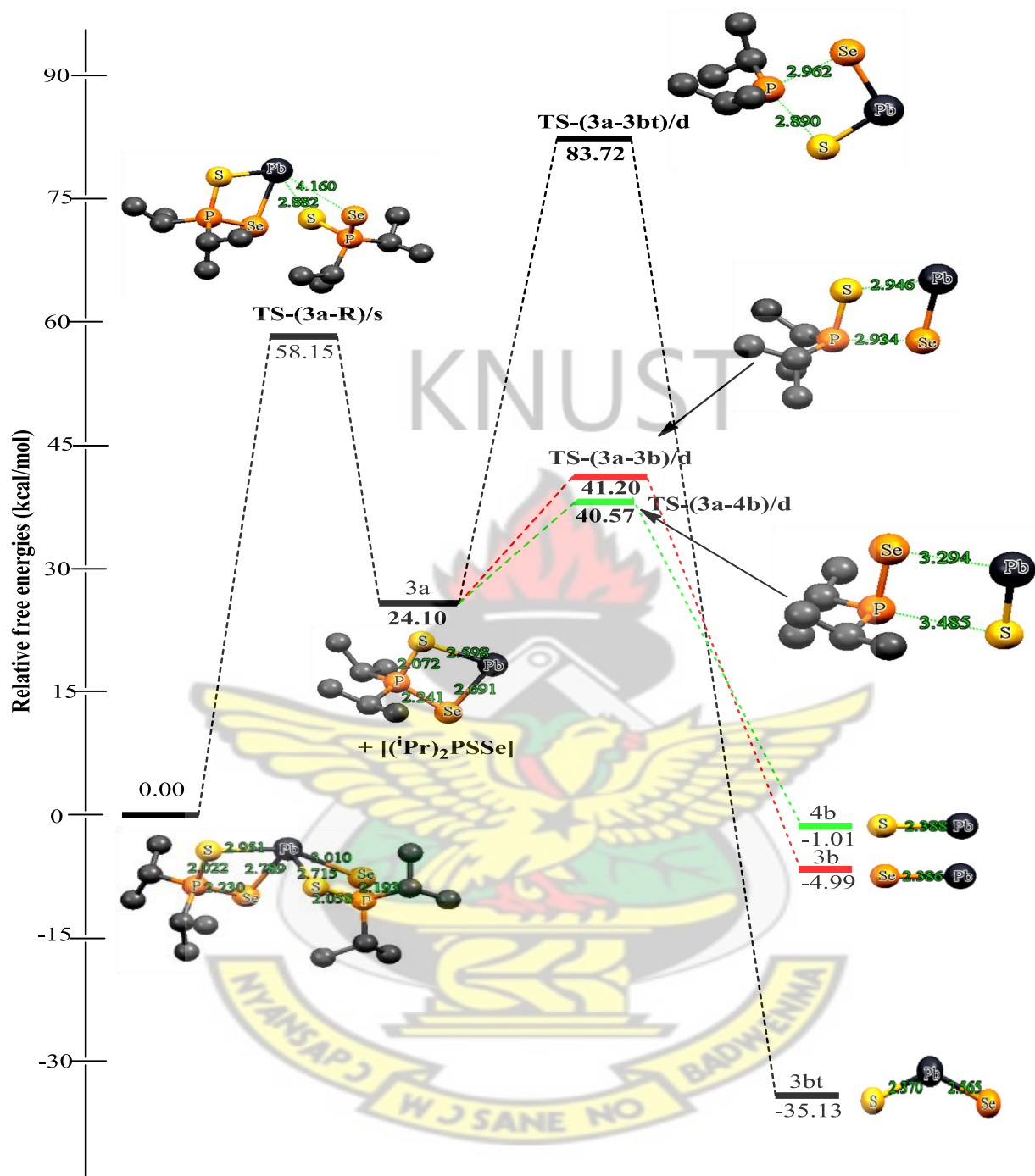


Figure 4.6: Energetics of the unimolecular decomposition pathway (3, 4) at 800 K. The relative free energies are in kcal/mol and bond distances in Å

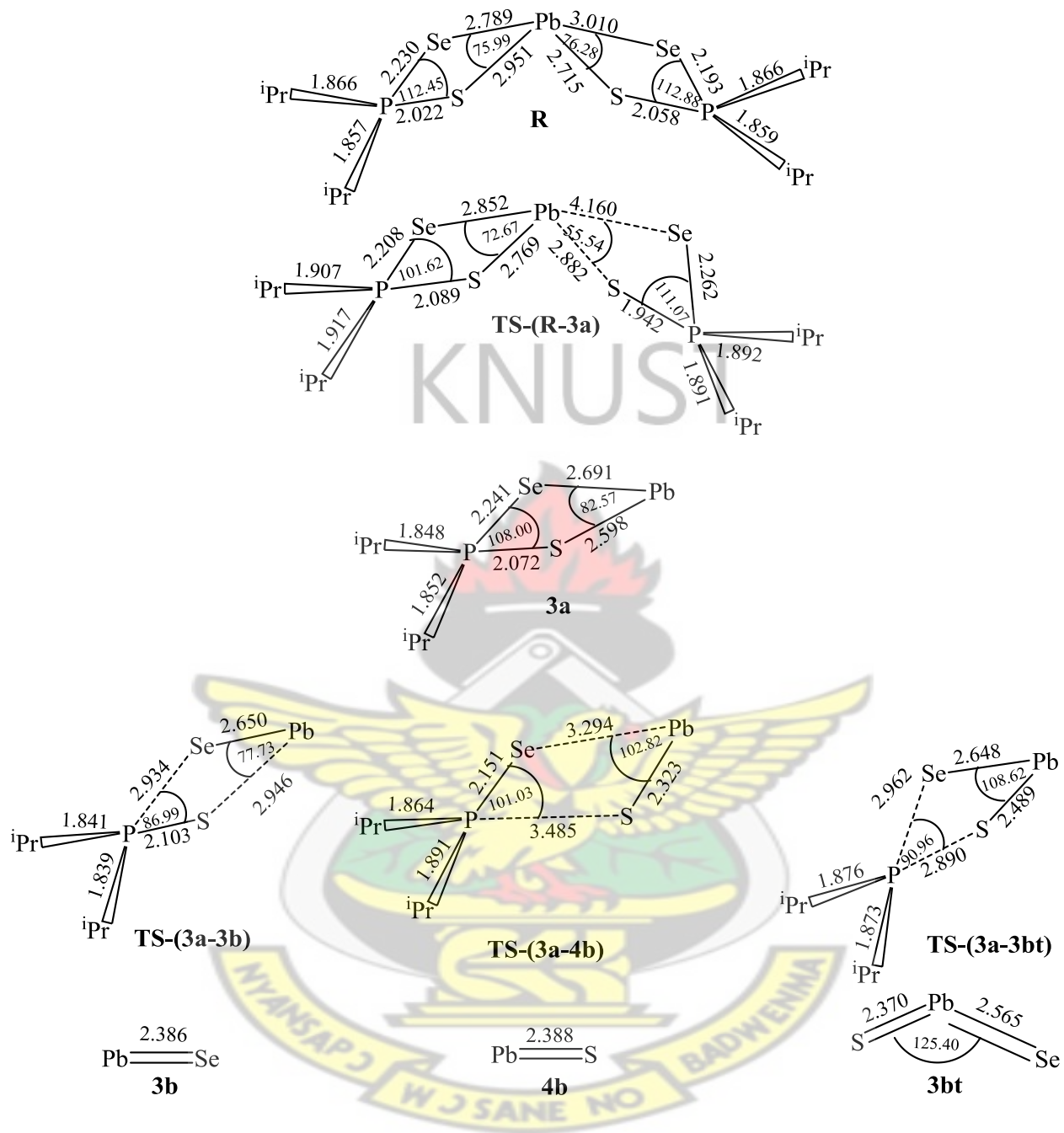


Figure 4.7: Optimized geometrical parameters of the main stationary points involved in the unimolecular decomposition pathway (3, 4). Bond distances in Å and bond angles in degrees

The reaction pathways involved in the decomposition of (<sup>i</sup>Pr)PSSe-Pb intermediate were studied on the singlet PES by considering the energetics of the reactants, intermediates and products. The potential energy surface for all the possible unimolecular pathways involved in decomposition of (<sup>i</sup>Pr)PSSe-Pb intermediate are given in Figures 4.8 and 4.9.

The decomposition of (<sup>i</sup>Pr)<sub>2</sub>PSSe-Pb **3a** intermediate was further explored by first abstracting isopropyl radical to form (<sup>i</sup>Pr)PSSe-Pb **5b** intermediate on the singlet PES. The activation free energy barrier was calculated as +11.44 kcal/mol (298.15 K) and +45.20 kcal/mol (800 K) and reaction free energy of -21.34 kcal/mol (298.15 K) and -1.99 kcal/mol (800 K) respectively.

The formation of PbSe **5c** from the (<sup>i</sup>Pr)PSSe-Pb **5b** intermediate through the transition state **TS-(5b-5c)** has been found to have an activation free energy barrier of +1.60 kcal/mol (298.15 K) and +16.11 kcal/mol (800 K) and a reaction free energy of -0.20 kcal/mol (298.15 K) and -0.90 kcal/mol (800 K) on the singlet PES. The optimized geometry of **TS-(5b-5c)** further reveals the elongation of Pb-S bond length from 2.528 to 3.779 Å and P-Se bond length from 2.314 to 2.860 Å.

The activation free energy barrier and reaction free energy involved in the abstraction (<sup>i</sup>Pr)PSe from (<sup>i</sup>Pr)PSSe-Pb intermediate **5b** through the transition state **TS-(5b-6c)** to form PbS **6c** were +0.73 kcal/mol (298.15 K) and +15.23 kcal/mol (800 K), and -4.16 kcal/mol (298.15 K) and -5.87 kcal/mol (800 K) respectively on the singlet PES. The optimized geometry of **TS-(5b-6c)** further reveals the elongation of Pb-Se bond length from 2.641 to 2.936 Å and P-S bond length from 2.160 to 3.369 Å.

The formation of ternary  $\text{PbSe}_x\text{S}_{1-x}$  **5ct** from (*i*Pr)PSSe-Pb intermediate **5b** proceed through a transition state **TS-(5b-5ct)** with a barrier of +1.18 kcal/mol (298.15 K) and +15.75 kcal/mol (800 K) and exergonic by 14.66 kcal/mol (298.15 K) and 16.37 kcal/mol (800 K) on the singlet PES. The optimized geometry of **TS-(5b-5ct)** further reveals the elongation of P-Se bond length from 2.314 to 2.903 Å and P-S bond length from 2.160 to 2.892 Å.

The activation energies involved in the main mechanistic steps - PbS (37.29 kcal/mol), PbSe (37.74 kcal/mol) and  $\text{PbSe}_x\text{S}_{1-x}$  (38.16 kcal/mol) are all in the narrow range of 37 to 38 kcal/mol. The results suggest that these reactions should be competitive in the temperature range used for CVD.

Kinetically the most favourable pathway is the [6c] dissociation pathway to form PbS. The barrier along this pathway is 15.23 kcal/mol lower than the barrier along the [5c] dissociation (16.11) kcal/mol and the [5ct] dissociation pathway (15.75 kcal/mol). In terms of energetics, the [5ct] dissociation pathway to form a ternary  $\text{PbSeS}_{1-x}$  is the most stable species on the reaction PES (16.37 kcal/mol exergonic).

The results also indicate that decomposition of (*i*Pr)PSSe-Pb intermediate to form PbS was kinetically more favourable and stable than ternary  $\text{PbSe}_x\text{S}_{1-x}$  and PbSe formation. The unimolecular and recombination rate constants along the [6c] decomposition pathway is  $1.05 \times 10^3 \text{ s}^{-1}$  and  $8.86 \times 10^{17} \text{ s}^{-1}$  at  $T = 800 \text{ K}$  respectively.

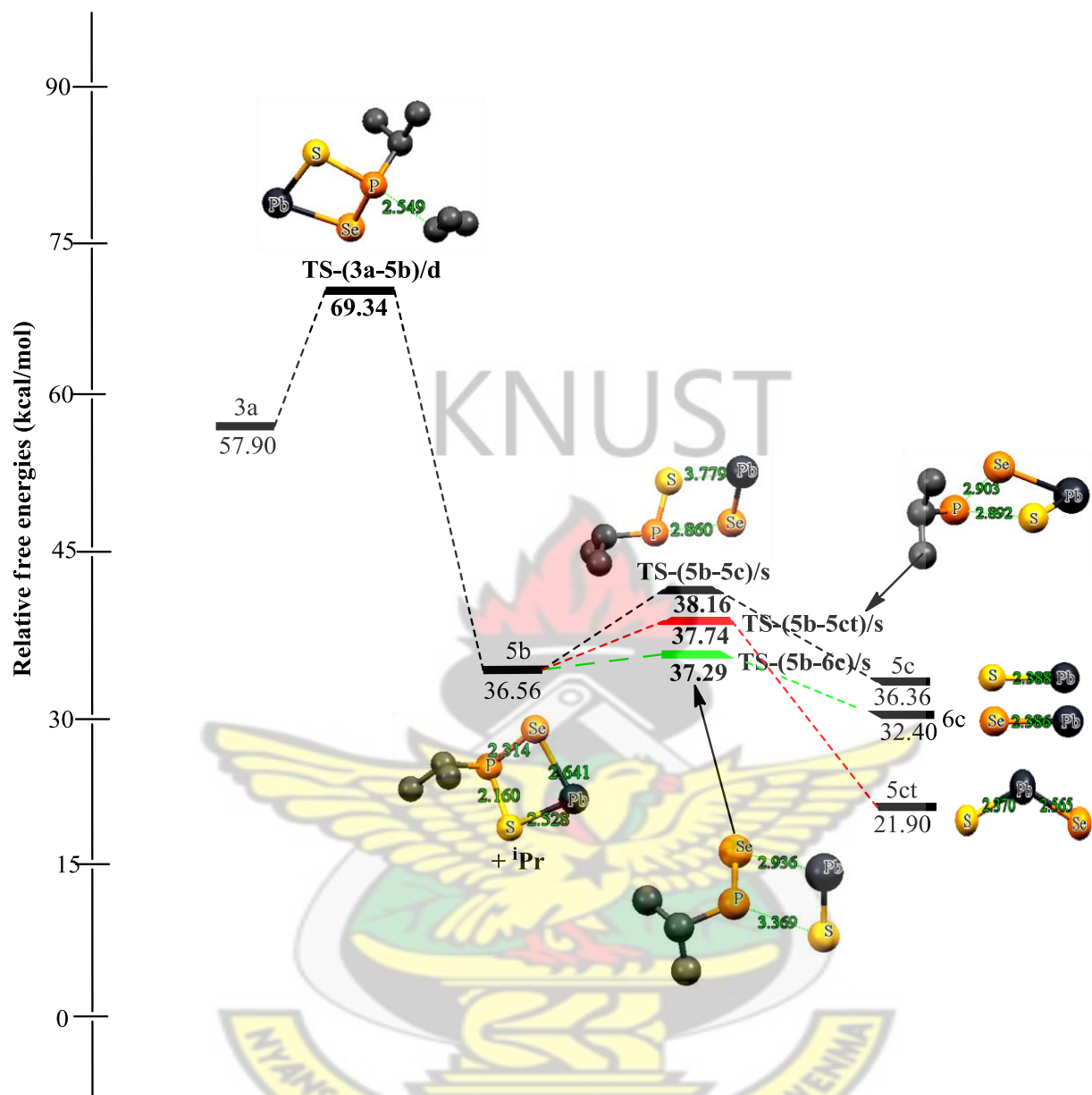


Figure 4.8: Energetics of the unimolecular decomposition pathway (5, 6) at 298.15 K. The relative free energies are in kcal/mol and bond distances in Å

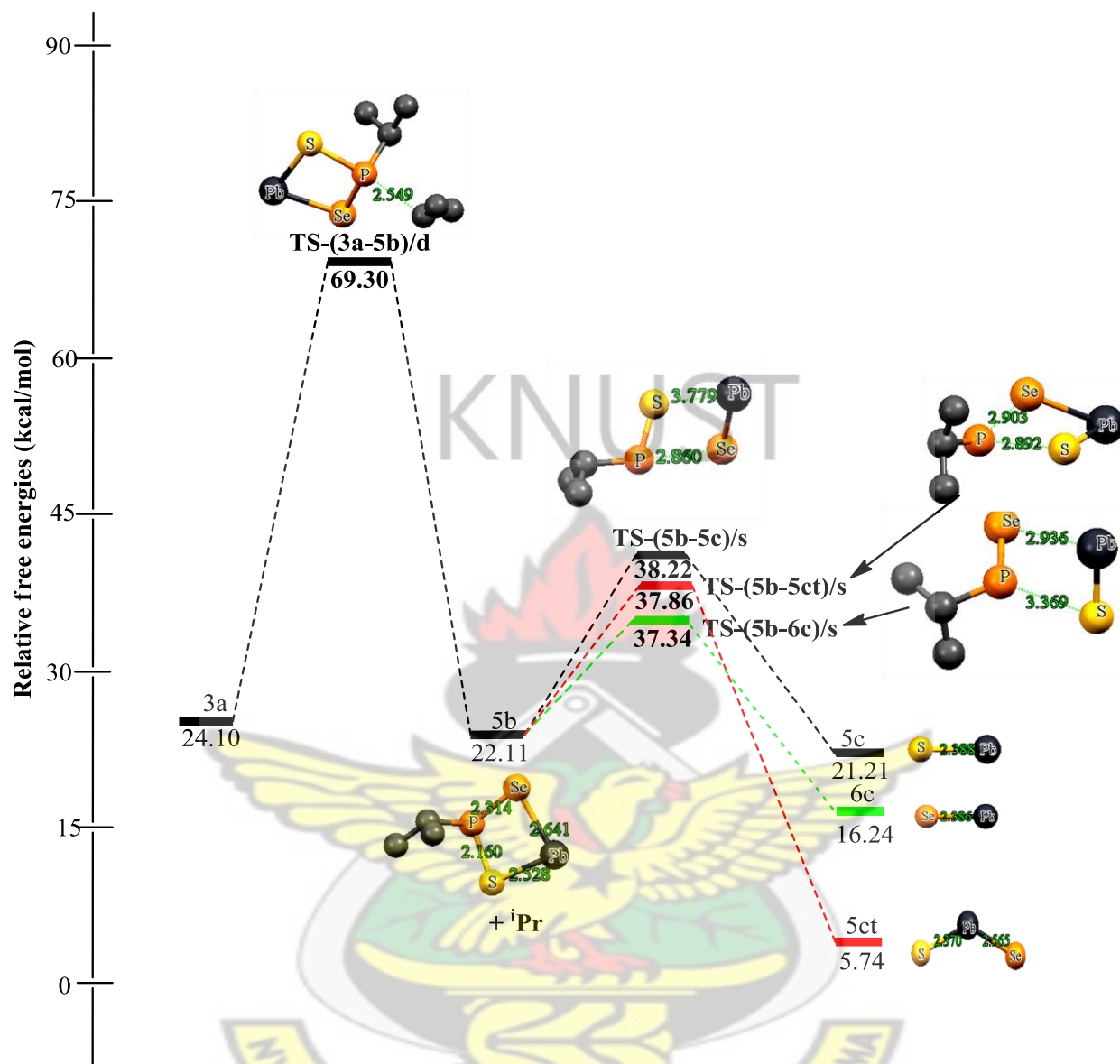


Figure 4.9: Energetics of the unimolecular decomposition pathway (5, 6) at 800 K. The relative free energies are in kcal/mol and bond distances in Å

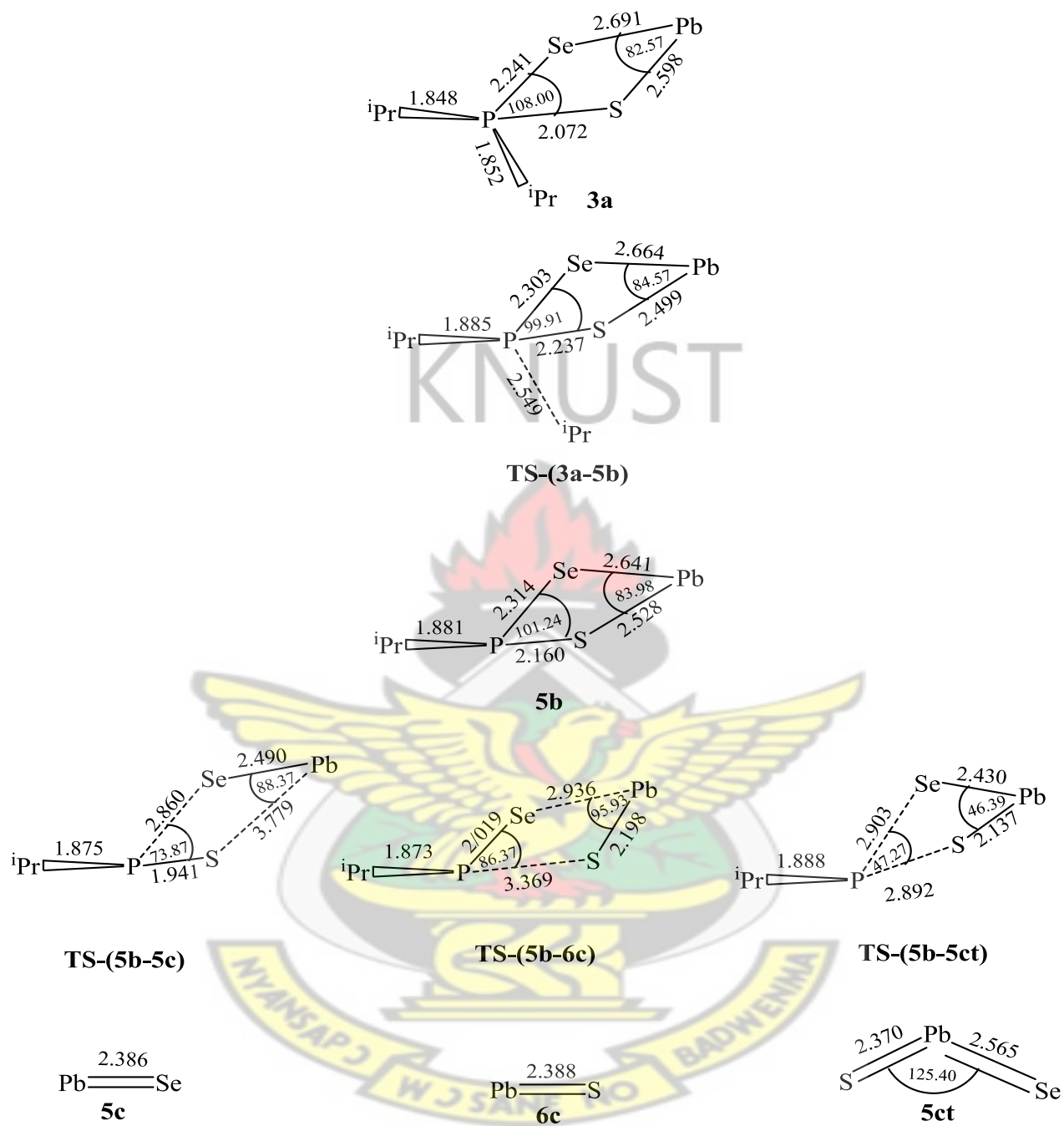


Figure 4.10: Optimized geometrical parameters of the main stationary points involved in the unimolecular decomposition pathway (5, 6). Bond distances in Å and bond angles in degrees

Table 4.2: Calculated rate constants for selected individual steps in the decomposition of  $\text{Pb}[(^i\text{Pr})_2\text{PSSe}]_2$  precursor both at room temperature (298.15 K) and at an elevated temperature (800 K)

Reaction pathway	$k_{\text{uni}} (\text{s}^{-1})$		$k_{\text{eq}}$		$k_{\text{rec}} (\text{s}^{-1})$	
	298.15 K	800 K	298.15 K	800 K	298.15 K	800 K
1c $\rightarrow$ 1d	$1.90 \times 10^{-43}$	$3.55 \times 10^{-8}$	$2.68 \times 10^{-1}$	$4.23 \times 10^{11}$	$5.09 \times 10^{-44}$	$2.98 \times 10^{-27}$
2c $\rightarrow$ 2d	$5.68 \times 10^{-40}$	$6.78 \times 10^{-7}$	$1.48 \times 10^{-1}$	$3.51 \times 10^{11}$	$8.41 \times 10^{-41}$	$1.31 \times 10^{-24}$
1c $\rightarrow$ 1dt	$1.19 \times 10^{-53}$	$6.70 \times 10^{-12}$	$4.07 \times 10^{-22}$	$2.14 \times 10^6$	$4.84 \times 10^{-75}$	$2.10 \times 10^{-23}$
2c $\rightarrow$ 2dt	$1.42 \times 10^{-40}$	$4.07 \times 10^{-7}$	$1.29 \times 10^{-19}$	$1.75 \times 10^2$	$1.83 \times 10^{-59}$	$9.48 \times 10^{-16}$
3a $\rightarrow$ 3b	$6.06 \times 10^{-18}$	$9.27 \times 10^1$	$3.97 \times 10^{-9}$	$4.55 \times 10^3$	$2.41 \times 10^{-26}$	$1.89 \times 10^1$
3a $\rightarrow$ 4b	$1.72 \times 10^{-17}$	$1.38 \times 10^2$	$1.66 \times 10^{-12}$	$5.50 \times 10^6$	$2.86 \times 10^{-29}$	$3.45 \times 10^{-3}$
3a $\rightarrow$ 3bt	$2.43 \times 10^{-49}$	$2.24 \times 10^{-10}$	$1.83 \times 10^3$	$5.65 \times 10^{25}$	$4.45 \times 10^{-46}$	$8.89 \times 10^{-46}$
5b $\rightarrow$ 5c	$1.34 \times 10^{-15}$	$7.62 \times 10^2$	$2.22 \times 10^{-27}$	$2.83 \times 10^{-16}$	$2.97 \times 10^{-42}$	$2.05 \times 10^{21}$
5b $\rightarrow$ 6c	$2.87 \times 10^{-15}$	$1.05 \times 10^3$	$1.78 \times 10^{-24}$	$1.25 \times 10^{-12}$	$5.11 \times 10^{-39}$	$8.86 \times 10^{17}$
5b $\rightarrow$ 5ct	$6.61 \times 10^{-16}$	$6.04 \times 10^2$	$8.84 \times 10^{-17}$	$6.20 \times 10^{-5}$	$5.84 \times 10^{-32}$	$5.89 \times 10^9$

The values of  $n_T$  for the thermal decomposition of  $\text{Pb}[(^i\text{Pr})_2\text{PSSe}]_2$  precursor is shown in Table 4.3. In fact, the similarity between the reactants, intermediates, and products increases with respect to the reactions in the order of  $5c > 6c > 5ct > 4b > 2dt > 1dt > 3b > 2d-1d > 3bt$ , and  $5c > 6c > 5ct > 1dt > 4b > 2dt > 3b > 2d-1d > 3bt$  at  $T = 298.15 \text{ K}$  and  $800 \text{ K}$  respectively. These results imply that the transition state structure involved in formation of  $\text{PbSe } 5c$  has a larger similarity to the product than the other reactions pathway at both temperatures.

Table 4.3: Position of the transition state structures ( $n_T$ ) for selected individual steps

Reaction pathway	298.15 K	800 K
1c $\rightarrow$ 1d	0.502588	0.452572
2c $\rightarrow$ 2d	0.504011	0.450067
1c $\rightarrow$ 1dt	0.597189	0.498743
2c $\rightarrow$ 2dt	0.609334	0.489566
3a $\rightarrow$ 3b	0.581369	0.47145
3a $\rightarrow$ 4b	0.624439	0.493853
3a $\rightarrow$ 3bt	0.487063	0.413289
5b $\rightarrow$ 5c	0.964724	0.694623
5b $\rightarrow$ 6c	0.884068	0.638946
5b $\rightarrow$ 5ct	0.701213	0.540594

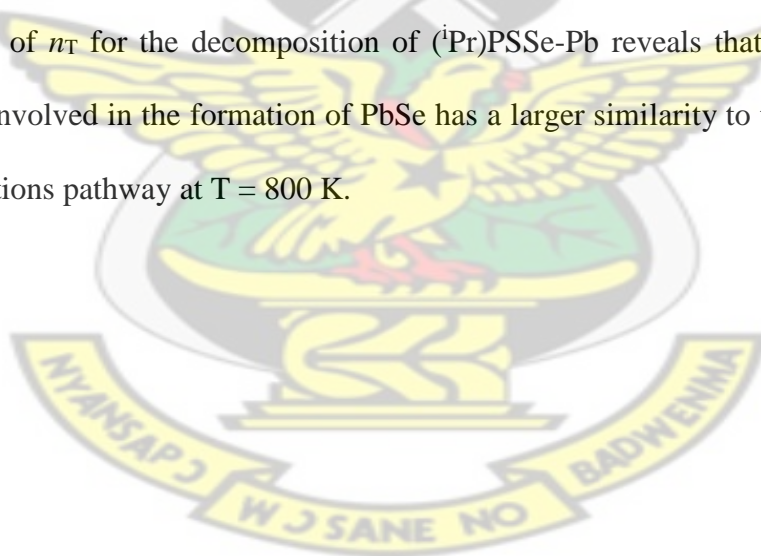
#### 4.5 Conclusion

A number of possible CVD decomposition reactions of  $\text{Pb}[(^i\text{Pr})_2\text{PSSe}]_2$  precursor were studied using DFT calculations. Several possible pathways involved in the decomposition of  $\text{Pb}[(^i\text{Pr})_2\text{PSSe}]_2$  precursor have been explored and their corresponding reaction free energies have been calculated, both at room temperature (298.15 K) and elevated temperature (800 K). The following conclusions are drawn from the results presented:

1. On the singlet PES, the decomposition of  $(^i\text{Pr})\text{PSSe-PbSe}$  intermediate leading to the formation of PbSe was thermodynamically favoured, but the reaction is kinetically blocked

by the highest activation barrier. The unimolecular and bimolecular recombination rate constants were calculated as  $3.55 \times 10^{-8} \text{ s}^{-1}$  and  $2.98 \times 10^{-27} \text{ s}^{-1}$  at  $T = 298.15 \text{ K}$  respectively.

2. The calculation indicate that on the singlet PES, the decomposition of (<sup>i</sup>Pr)PSSe-Pb intermediate leading to the formation of PbS, is proposed as the most probable decomposition mechanism. The unimolecular and bimolecular recombination rate constants were calculated as  $1.05 \times 10^3 \text{ s}^{-1}$  and  $8.86 \times 10^{17} \text{ s}^{-1}$  at  $T = 800 \text{ K}$  respectively.
3. On the doublet PES, the decomposition of (<sup>i</sup>Pr)<sub>2</sub>PSSe-Pb intermediate leading to the formation of ternary PbSe<sub>x</sub>S<sub>1-x</sub> was thermodynamically favoured, but the reaction is kinetically blocked by the highest activation barrier. The unimolecular and bimolecular recombination rate constants were calculated as  $2.24 \times 10^{-10} \text{ s}^{-1}$  and  $8.89 \times 10^{-46} \text{ s}^{-1}$  at  $T = 800 \text{ K}$  respectively. The most plausible pathway leads to the formation of PbS.
4. The value of  $n_T$  for the decomposition of (<sup>i</sup>Pr)PSSe-Pb reveals that the transition state structure involved in the formation of PbSe has a larger similarity to the product than the other reactions pathway at  $T = 800 \text{ K}$ .



## References

- Afzaal, M., Ellwood, K., Pickett, N. L., O'Brien, P., Raftery, J. and Waters, J. (2004). "Growth of lead chalcogenide thin films using single-source precursors". *J. Mater. Chem.*, 14, 1310-1315.
- Akhtar, J., Afzaal, M., Vincent, M., Burton, N., Raftery, J., Hillier, I. and O'Brien, P. (2011). "Understanding the Decomposition Pathways of Mixed Sulphur/Selenium Lead Phosphinato Precursor Explaining the Formation of Lead Selenide". *J. Phys. Chem. C*, 115(34): 16904-16909.
- Beard, M. C., Ellingson, R. J. (2008). "Multiple Exciton Generation in Semiconductor Nanocrystals: Toward Efficient Solar Energy Conversion". *Laser Photonics Rev.*, 2: 377-399.
- Colvin, V. L., Schlamp, M. C. and Alivisatos, A. P. (1994). "On Conductivity in Lead Chalcogenides". *Nature*, 370: 354-357.
- Ellingson, R. J., Beard, M. C., Johnson, J. C., Yu, P. R., Micic, O. I., Nozik, A. J., Shabaev, A. and Efros, A. L. (2005). "Highly Efficient Multiple Exciton Generation in Colloidal PbSe and PbS Quantum Dots". *Nano Lett.*, 5: 865-871.
- Luther, J. M., Law, M., Song, Q., Perkins, C. L., Beard, M. C. and Nozik, A. J. (2008). "Structural, Optical and Electrical Properties of Self-Assembled Films of PbSe Nanocrystals Treated with 1,2-Ethanedithiol". *ACS Nano*, 2: 271-280.

## CHAPTER FIVE

### DENSITY FUNCTIONAL THEORY (DFT) STUDY OF THE DECOMPOSITION OF Zn[(<sup>i</sup>Pr)<sub>2</sub>PSSe]<sub>2</sub> SINGLE-SOURCE PRECURSOR FOR THE CHEMICAL VAPOUR DEPOSITION OF BINARY AND TERNARY ZINC CHALCOGENIDES

#### Abstract

The reaction mechanisms involved in the thermal decomposition of Zn[(<sup>i</sup>Pr)<sub>2</sub>PSSe]<sub>2</sub> single-source precursor have been examined, both at room temperature and elevated temperature. The kinetic and thermodynamic parameters involved were computed at the density functional theory MO6/LACVP\* level of theory. The results indicate that the steps that lead to ZnS formation on the singlet potential energy surface is favoured kinetically over those that lead to ZnSe and ternary ZnSe<sub>x</sub>S<sub>1-x</sub> formation. On the doublet PES, the steps that lead to ZnSe formation are more favourable on kinetic grounds than those that lead to ZnS and ternary ZnSe<sub>x</sub>S<sub>1-x</sub> formation. The steps that lead to ternary ZnSe<sub>x</sub>S<sub>1-x</sub> formation on both the singlet and the doublet PES's are more favourable than those that lead to ZnSe and ZnS formation. Density functional theory calculations of the formation of ternary ZnSe<sub>x</sub>S<sub>1-x</sub> are consistent with a dominant role on thermodynamic grounds rather than kinetic ones in controlling the material formed during the deposition process.

**Keywords:** single-source precursor, density functional theory, reaction pathways, thermal decomposition, plausible pathway

## 5.1 Introduction

The group II–VI thin films are important semiconductor compounds and among one of the most explored because of their wide range of potential applications. ZnS is a promising material for optoelectronic device applications such as optical coatings, solid-state solar cell windows, electrooptic modulators, photoconductors, field effect transistors, sensors, transducers, light-emitting applications, and photonic crystal devices which operate in the region from visible to near infrared (Gao *et al.*, 2004; Nicolau *et al.*, 1998; Bhargava, 1994; Elidrissi *et al.*, 2011).

The surface reaction that result in film formation during chemical vapour deposition (CVD) provide opportunities for growth of highly conformal thin layers of material on substrates, an advantage of chemical deposition methods as compared to physical deposition methods. Approach to precursor design is a mechanism-based strategy in which known pathways for thermal decomposition of organometallic precursor have been used to predict the reactivity of precursors during CVD process. The challenge is the difference between reaction conditions used in the majority of mechanistic studies (precursor in solution at or below room temperature) and the conditions used in CVD (gas/surface reaction at temperatures  $\geq 600$  °C).

The mixed crystals of II–VI compound semiconductors have attracted much attention for applications in optical devices (Gunshor and Nurmikko, 1997). Indeed, the easiest way to change artificially the electronic and optical properties of semiconductors is by forming their alloys. It seems therefore very interesting to study ZnS and ZnSe mixed in the  $\text{ZnSe}_x\text{S}_{1-x}$  ternary alloys.

The studies performed by Akhtar *et al.* (2011) allow us to rationalize the mechanisms involved in the thermal decomposition of  $\text{Zn}[(i\text{Pr})_2\text{PSSe}]_2$  precursor and to explore the thermodynamic and

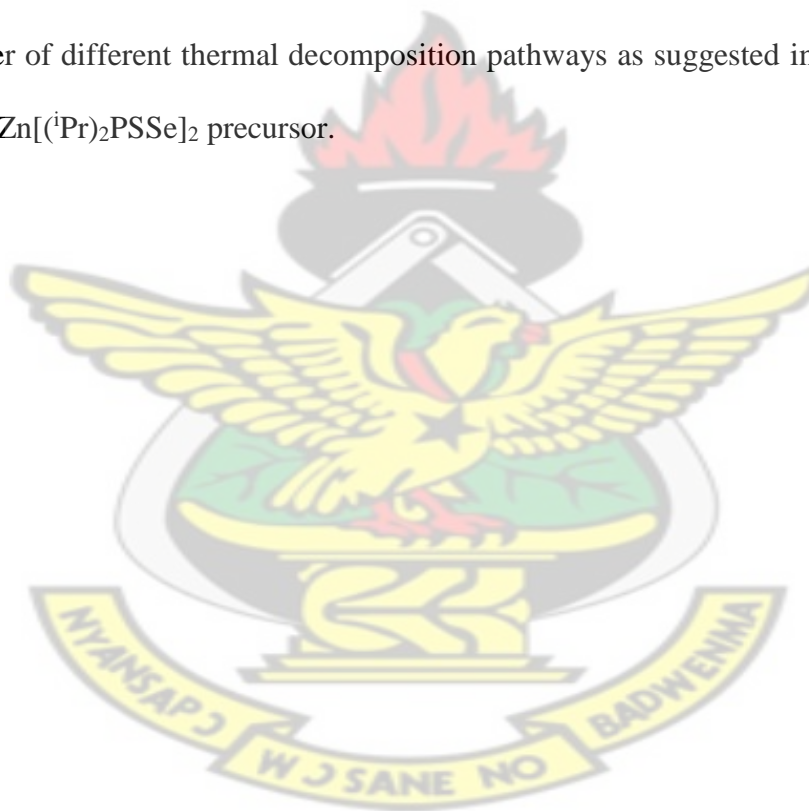
kinetic parameters for a variety of steps leading to the formation of binary and ternary alloys by employing density functional theory calculations at the MO6/LACVP\* level of theory (Koch and Holthansen, 2001).

## 5.2 Details of calculations

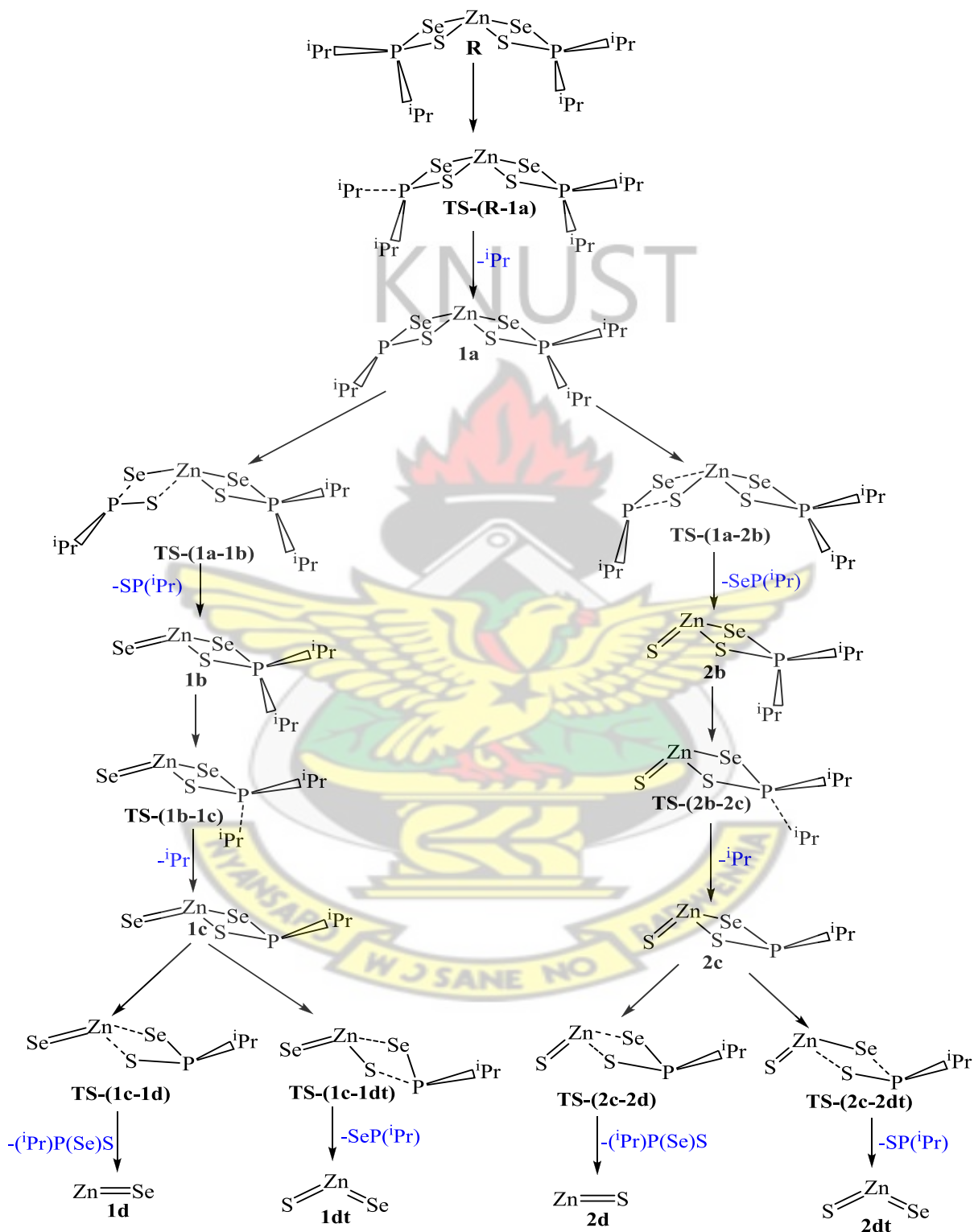
All calculations were done using the same method in section 3.2.

## 5.3 Mechanistic considerations

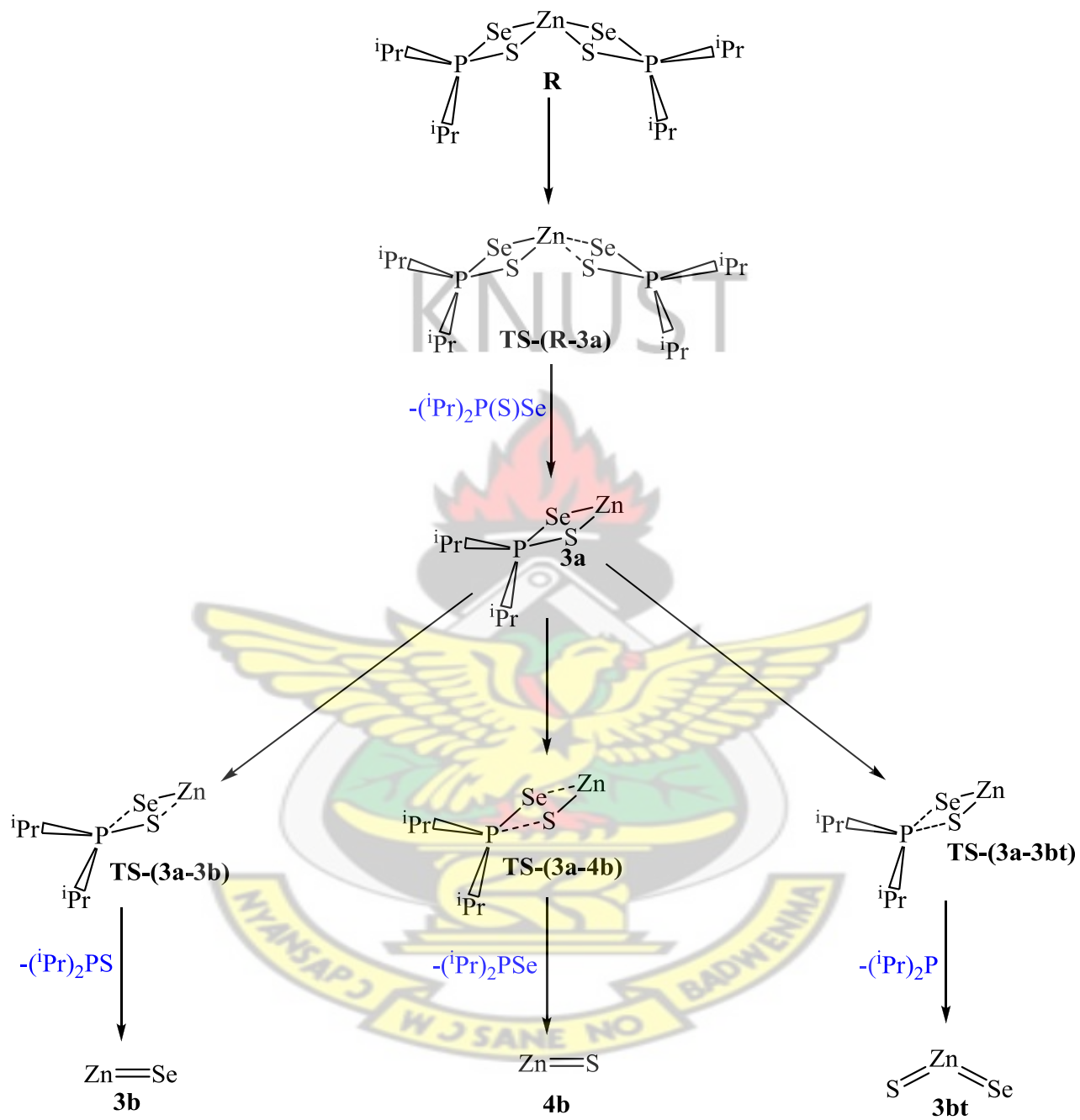
A number of different thermal decomposition pathways as suggested in section 3.3 were investigated for  $\text{Zn}[(^i\text{Pr})_2\text{PSSe}]_2$  precursor.



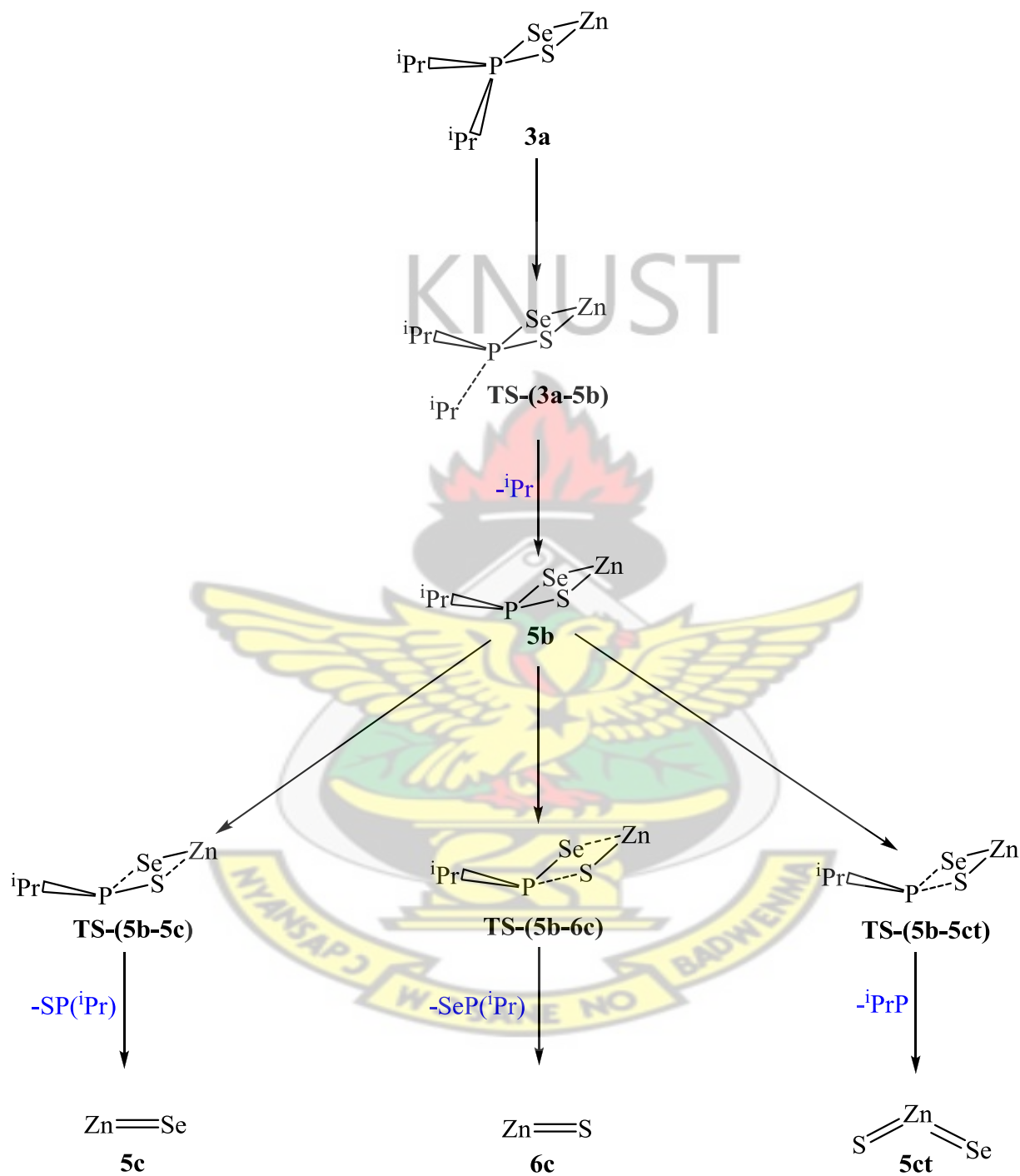
Scheme 5.1: Decomposition pathway (1, 2) of  $\text{Zn}[(i\text{Pr})_2\text{PSSe}]_2$  precursor



Scheme 5.2: Decomposition pathway (3, 4) of  $\text{Zn}[(i\text{Pr})_2\text{PSSe}]_2$  precursor



Scheme 5.3: Decomposition pathway (5, 6) of  $\text{Zn}[(i\text{Pr})_2\text{PSSe}]_2$  precursor



## 5.4 Results and discussion

### 5.4.1 Optimized Geometry of $\text{Zn}[(i\text{Pr})_2\text{PSSe}]_2$ precursors

DFT calculations using the MO6/6-31G\* levels of theory with the Los Alamos quasi-relativistic effective core potential (Lan2DZ) described in computational methods were employed. The optimized geometrical parameters are shown in Table 5.1. To the best of our knowledge there are no reports for the use of  $\text{Zn}[(i\text{Pr})_2\text{PSSe}]_2$  complexes as a single source precursor for the preparation of zinc chalcogenides thin films or nanoparticles. The geometry at the zinc atom is a distorted tetrahedral with the ligand bond angles of  $87.85^\circ$  and  $87.46^\circ$  and somewhat smaller than the perfect tetrahedral angle, but the angles are slightly wider than those in the  $\text{Cd}[(i\text{Pr})_2\text{PSSe}]_2$  precursor analogue. The two sulphur and two selenium atoms are at the corners of the tetrahedron. The density functional theory (DFT) geometry optimization of  $\text{Zn}[(i\text{Pr})_2\text{PSSe}]_2$  precursor on a singlet potential energy surface (PES) has Zn-S bond length at  $2.20 \text{ \AA}$ , which is shorter than the Zn-Se bond length at  $2.54 \text{ \AA}$ .

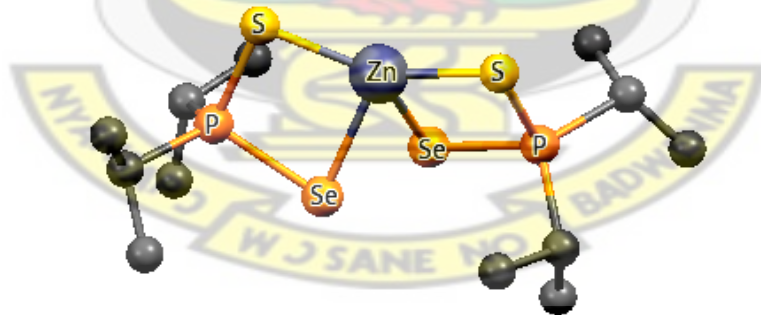


Fig. 5.1: Optimized geometry of  $\text{Zn}[(i\text{Pr})_2\text{PSSe}]_2$  single-source precursor

Table 5.1: Selected bond lengths (Å) and bond angles (°) of Zn[(<sup>i</sup>Pr)<sub>2</sub>PSSe]<sub>2</sub> precursor

Bonds	length(Å)	bonds	angles (°)
P-S	2.1329	S-P-Se	97.97
P-Se	2.2397	S-Zn-Se	87.46
S-P	2.1391	Se-Zn-S	87.85
Se-P	2.2392	Se-Zn-Se	52.56
Zn-S	2.2022	S-Zn-S	150.06
Zn-Se	2.5419	S-Zn-Se	120.53
S-Zn	2.2001	Se-Zn-S	120.02
Se-Zn	2.5467	Se-P-S	97.44

#### 5.4.2: Overall Decomposition of Zn[(<sup>i</sup>Pr)<sub>2</sub>PSSe]<sub>2</sub> precursor

The proposed mechanisms (Scheme 5.1) involved in the thermal decomposition of Zn[(<sup>i</sup>Pr)<sub>2</sub>PSSe]<sub>2</sub> precursor leading to the formation of zinc chalcogenides thin films were studied using DFT calculations. Values of free energy change,  $\Delta G^\circ$  and free energy of activation,  $G^\ddagger$  of intermediates, along with selected geometrical parameters are shown in Figures 5.2 and 5.3. To determine the rate at which these decomposition proceeds, the appropriate transition state for these reactions pathway were located.

Abstraction of isopropyl radical from reactant **R** gives **1a** intermediate on the doublet PES. The formation of **1a** intermediate through transition state **TS-(R-1a)** has an activation free energy barrier of +70.45 kcal/mol (298.15 K) and +70.13 kcal/mol (800 K) and endergonic by +55.19 kcal/mol (298.15 K) and +26.01 kcal/mol (800 K).

The reaction surface was further explored by decomposing **1a** into (<sup>i</sup>Pr)<sub>2</sub>PSSe-Zn-Se **1b** and (<sup>i</sup>Pr)<sub>2</sub>PSSe-Zn-S **2b** intermediates (Scheme 4.1) on the doublet PES. The decomposition of **1a** to form **1b** and **2b** through transition state **TS-(1a-1b)** and **TS-(1a-2b)** have an activation free energy barrier of +11.66 kcal/mol (298.15 K) and +30.31 kcal/mol (800 K), and +13.05 kcal/mol (298.15 K) and +32.05 kcal/mol (800 K) respectively. The reaction free energies were -22.61 kcal/mol (298.15 K) and -24.00 kcal/mol (800 K) for **1b**, and -13.7 kcal/mol (298.15 K) and -15.77 kcal/mol (800 K) for **2b**.

Conversion of **1b** and **2b** intermediates into (<sup>i</sup>Pr)PSSe-Zn-Se **1c** and (<sup>i</sup>Pr)PSSe-Zn-S **2c** intermediates proceed through the transition state **TS-(1b-1c)** and **TS-(2b-2c)** after a loss of isopropyl radical on the singlet PES. The activation free energy barrier for **1c** and **2c** were calculated as +42.21 kcal/mol (298.15 K) and +77.63 kcal/mol (800 K), and +37.38 kcal/mol (298.15 K) and +65.52 kcal/mol (800 K) respectively with a reaction free energy of +7.76 kcal/mol (298.15 K) and +9.91 kcal/mol (800 K) for **1c**, and -7.84 kcal/mol (298.15 K) and -5.13 kcal/mol (800 K) for **2c**.

On the singlet PES, the decomposition of (<sup>i</sup>Pr)PSSe-Zn-Se **1c** and (<sup>i</sup>Pr)PSSe-Zn-S **2c** proceeded through a transition state **TS-(1c-1d)** and **TS-(2c-2d)** to form ZnSe **1d** and ZnS **2d**. The formation of ZnSe **1d** has an activation free energy barrier of +21.02 kcal/mol (298.15 K) and +56.22 kcal/mol (800 K), and an exergonic by 48.16 kcal/mol (298.15 K) and 31.05 kcal/mol (800 K). The optimized geometry of **TS-(1c-1d)** further reveals the elongation of Zn-S bond length from 2.490 to 2.700 Å and Zn-Se bond length from 2.596 to 2.850 Å. The formation of ZnS **2d** through **TS-(2c-2d)** has an activation free energy barrier of +28.35 kcal/mol (298.15 K) and +49.22 kcal/mol (800 K), and reaction free energy of -35.85 kcal/mol (298.15 K) and -22.64 kcal/mol (800 K).

(800 K). The optimized geometry of **TS-(2c-2d)** further reveals the elongation of Zn-S bond length from 2.488 to 3.430 Å and Zn-Se bond length from 2.589 to 3.453 Å.

The potential energy surface involved in the decomposition of (<sup>i</sup>Pr)PSSe-Zn-Se **1c** and (<sup>i</sup>Pr)PSSe-Zn-S **2c** intermediates were further explored to access the ternary nature of the intermediates. The transition state **TS-(1c-1dt)** linking **1c** to form ternary ZnSe<sub>x</sub>S<sub>1-x</sub> **1dt** has a barrier of +31.31 kcal/mol (298.15 K) and +67.34 kcal/mol (800 K), and exergonic by 49.64 kcal/mol (298.15) and 46.80 kcal/mol (800 K). The optimized geometry of **TS-(1c-1dt)** further reveals the elongation of Zn-Se bond length from 2.596 to 2.678 Å and P-S bond length from 2.159 to 2.852 Å. The transition state **TS-(2c-2dt)** along the **2c** pathway has a barrier of +31.98 kcal/mol (298.15 K) and +53.65 kcal/mol (800 K), and exergonic by 49.72 kcal/mol (298.15 K) and 46.47 kcal/mol (800 K). The optimized geometry of **TS-(2c-2dt)** further reveals the elongation of the Zn-S bond length from 2.488 to 2.955 Å and P-Se bond length from 2.314 to 3.192 Å.

On the singlet surface, the [2d] decomposition pathway leading to the formation of ZnS is kinetically the most favoured pathway since the activation barrier is lower than the [2dt], [1dt] decomposition pathway leading to the formation of ZnSe<sub>x</sub>S<sub>1-x</sub> and [1d] decomposition pathway leading to the formation of ZnSe. The unimolecular and bimolecular recombination rate constants were calculated as  $2.57 \times 10^{-4} \text{ s}^{-1}$  and  $1.82 \times 10^9 \text{ cm}^3 \text{ molecule}^{-1} \text{ s}^{-1}$  at  $T = 800 \text{ K}$  respectively. On the reaction PES, ternary ZnSe<sub>x</sub>S<sub>1-x</sub> [2dt] formed from decomposition of <sup>i</sup>PrPSSe-Zn-Se intermediate is the most stable species (46.80 kcal/mol exergonic), but the reaction is kinetically blocked by the highest activation barrier. Thermodynamically the most favoured pathway is the 2dt decomposition pathway.

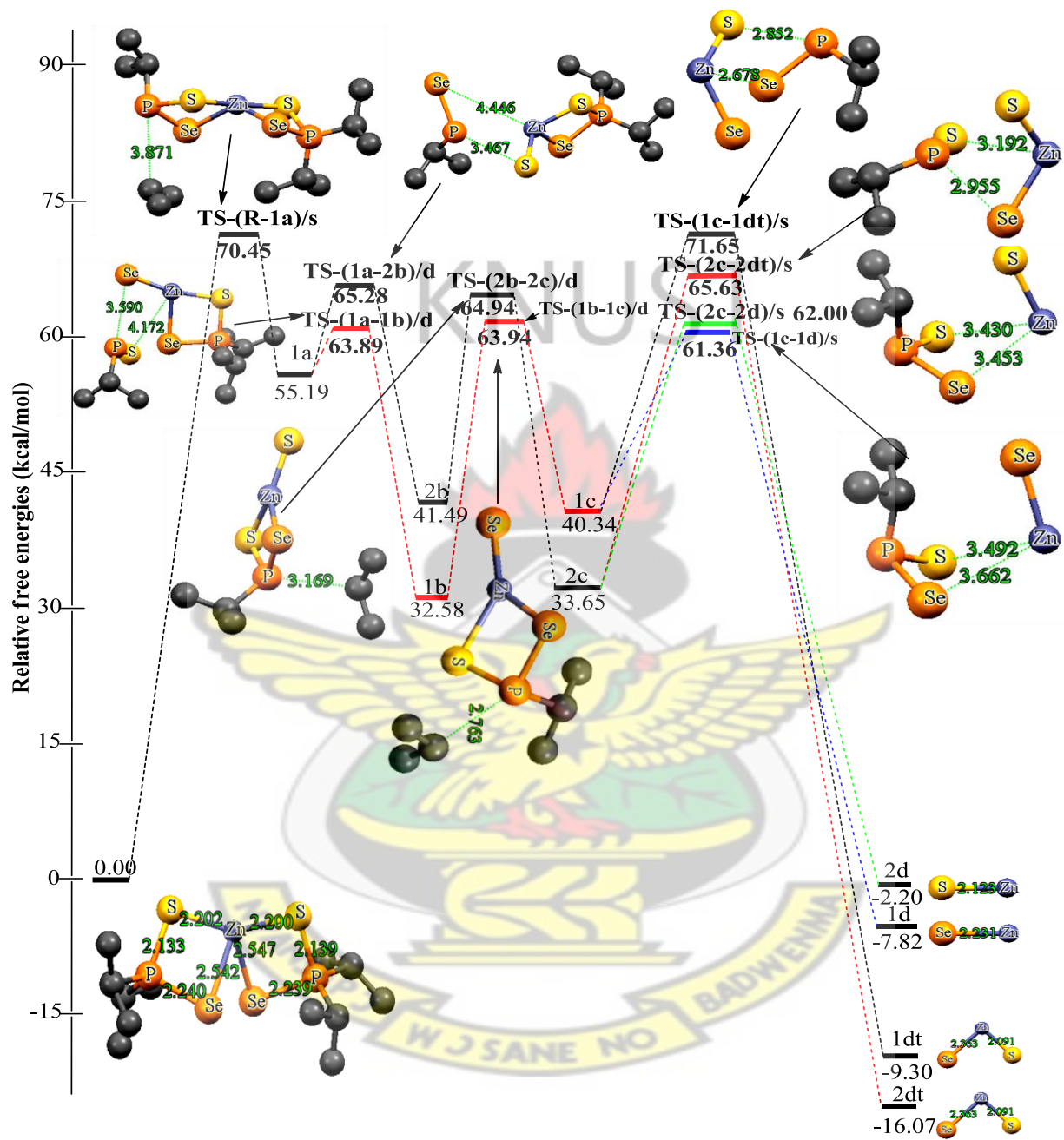


Figure 5.2: Energetics of the unimolecular decomposition pathway (1, 2) at 298.15 K. The relative free energies are in kcal/mol and bond distances in Å

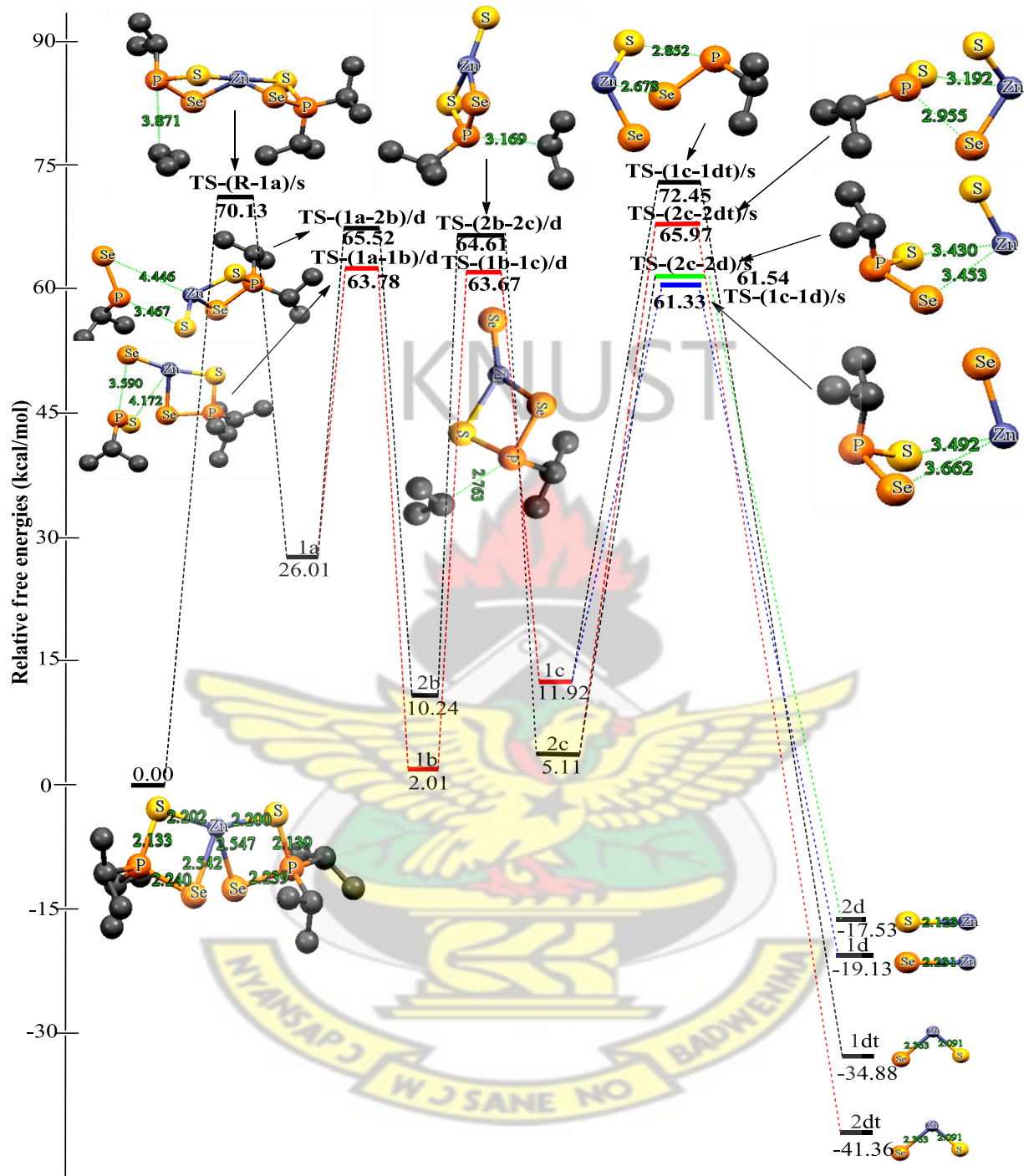


Figure 5.3: Energetics of the unimolecular decomposition pathway (1, 2) at 800 K. The relative free energies are in kcal/mol and bond distances in Å

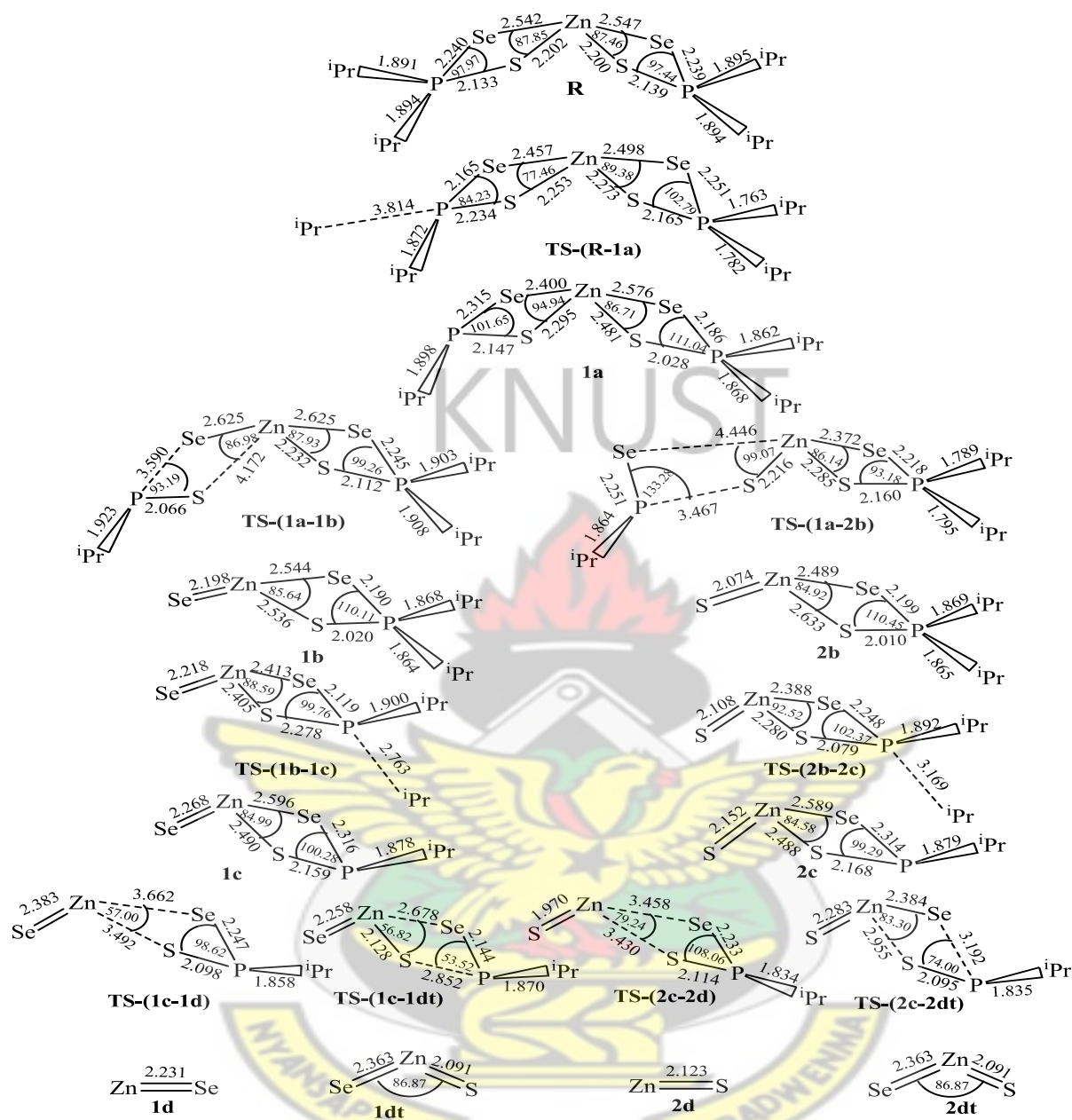


Figure 5.4: Optimized geometrical parameters of the main stationary points involved in the unimolecular decomposition pathway (1, 2). Bond distances in Å and bond angles in degrees

The reaction mechanisms involved in the unimolecular decomposition of  $(i\text{Pr})_2\text{PSSe-Zn}$  intermediate leading to the formation of zinc chalcogenides are shown in Figures 5.5 and 5.6.

The initial decomposition of  $[\text{Zn}\{(\text{iPr})_2\text{PSSe}\}_2]$  precursor was further explored by abstracting  $(\text{iPr})_2\text{PSSe}^-$  radical to form  $(\text{iPr})_2\text{PSSe-Zn } \mathbf{3a}$  intermediate on the doublet PES. The decomposition of  $[\text{Zn}\{(\text{iPr})_2\text{PSSe}\}_2]$  precursor to form  $(\text{iPr})_2\text{PSSe-Zn } \mathbf{3a}$  intermediate proceed through a transition state **TS-(R-3a)** with an activation free energy barrier of +62.29 kcal/mol (298.15 K) and +61.81 kcal/mol (800 K) and endergonic by +51.38 (298.15 K) and +27.51 (800 K) kcal/mol respectively.

The formation of  $\text{ZnSe } \mathbf{3b}$  through a transition state **TS-(3a-3b)** has an activation free energy barrier of -21.08 kcal/mol (298.15 K) and +0.82 kcal/mol (800 K), and reaction free energy of -35.83 kcal/mol (298.15 K) and -28.57 kcal/mol (800 K) on the doublet PES. This unimolecular decomposition, however, has the lowest activation free energy barrier and will proceed very fast with unimolecular and bimolecular recombination rate constants of  $3.02 \times 10^5 \text{ s}^{-1}$  and  $5.31 \times 10^4 \text{ cm}^3 \text{ molecule}^{-1} \text{ s}^{-1}$  at  $T = 800 \text{ K}$ . The optimized geometry of **TS-(3a-3b)** further reveals the elongation of Zn-S bond length from 2.203 to 2.975 Å and P-Se bond length from 2.284 to 2.827 Å.

Also, the activation free energy barrier involved in the formation of  $\text{ZnS } \mathbf{4b}$  through a transition state **TS-(3a-4b)** was found to be -19.10 kcal/mol (298.15 K) and +5.35 kcal/mol (800 K) with a reaction free energy of -30.53 kcal/mol (298.15 K) and -23.50 kcal/mol (800 K) on the doublet PES. The optimized geometry of **TS-(3a-4b)** further reveals the elongation of Zn-Se bond length from 2.289 to 2.950 Å and P-S bond length from 2.107 to 2.800 Å.

The transition state energy involved in the decomposition of  $(\text{iPr})_2\text{PSSe-Zn}$  was lower than the free energy of the intermediate. The calculations predict that in the gas phase,  $\text{ZnSe}$  or  $\text{ZnS}$

decomposition is likely to occur without a barrier at  $T = 298.15$  K. It can be observed that these reactions cannot proceed with an acceptable rate at room temperature.

Decomposition of  $(i\text{Pr})_2\text{PSSe-Zn } \mathbf{3b}$  to form ternary  $\text{ZnSe}_x\text{S}_{1-x} \mathbf{3bt}$  was further explored to access the ternary nature of the intermediate. The activation free energy barrier involved in the formation of ternary  $\text{ZnSe}_x\text{S}_{1-x}$  through a transition state **TS-(3a-3bt)** has been computed as +35.86 kcal/mol (298.15 K) and +58.86 kcal/mol (800 K) with a reaction free energy -61.27 kcal/mol (298.15 K) and -63.55 kcal/mol (800 K) on the doublet PES. However, the activation energy involved in the formation of ternary  $\text{ZnSe}_x\text{S}_{1-x}$  was significantly higher than the activation energy required for ZnSe. This means that ZnSe can diffuse more easily on the surface to produce a smooth surface and avoid structural impurities. The optimized geometry of **TS-(3a-3bt)** further reveals the elongation of P-Se bond length from 2.284 to 3.069 Å and P-S bond length from 2.107 to 2.902 Å.

On the doublet PES, the [3b] elimination pathway leading to the formation of ZnSe from the  $(i\text{Pr})_2\text{PSSe-Zn}$  intermediate is kinetically favoured over ZnS [4b] and ternary  $\text{ZnSe}_x\text{S}_{1-x}$  [3bt] decomposition pathways. The activation barriers for the formation of ZnSe, ZnS and ternary  $\text{ZnSe}_x\text{S}_{1-x}$  from  $(i\text{Pr})_2\text{PSSe-Zn}$  intermediate were found to be 0.82 kcal/mol, 5.35 kcal/mol and 58.86 kcal/mol respectively. The unimolecular and bimolecular recombination rate constants for the 3b pathway were calculated as  $3.02 \times 10^5 \text{ s}^{-1}$  and  $1.72 \times 10^{12} \text{ s}^{-1}$  at  $T = 800$  K respectively.

In terms of energetics, ternary  $\text{ZnSe}_x\text{S}_{1-x}$  [3bt] formed from decomposition of the  $(i\text{Pr})_2\text{PSSe-Zn}$  intermediate is the most stable species on the reaction PES (63.55 kcal/mol exergonic). Thermodynamically the most favoured pathway is the 3bt decomposition pathway to form a ternary  $\text{ZnSe}_x\text{S}_{1-x}$ .

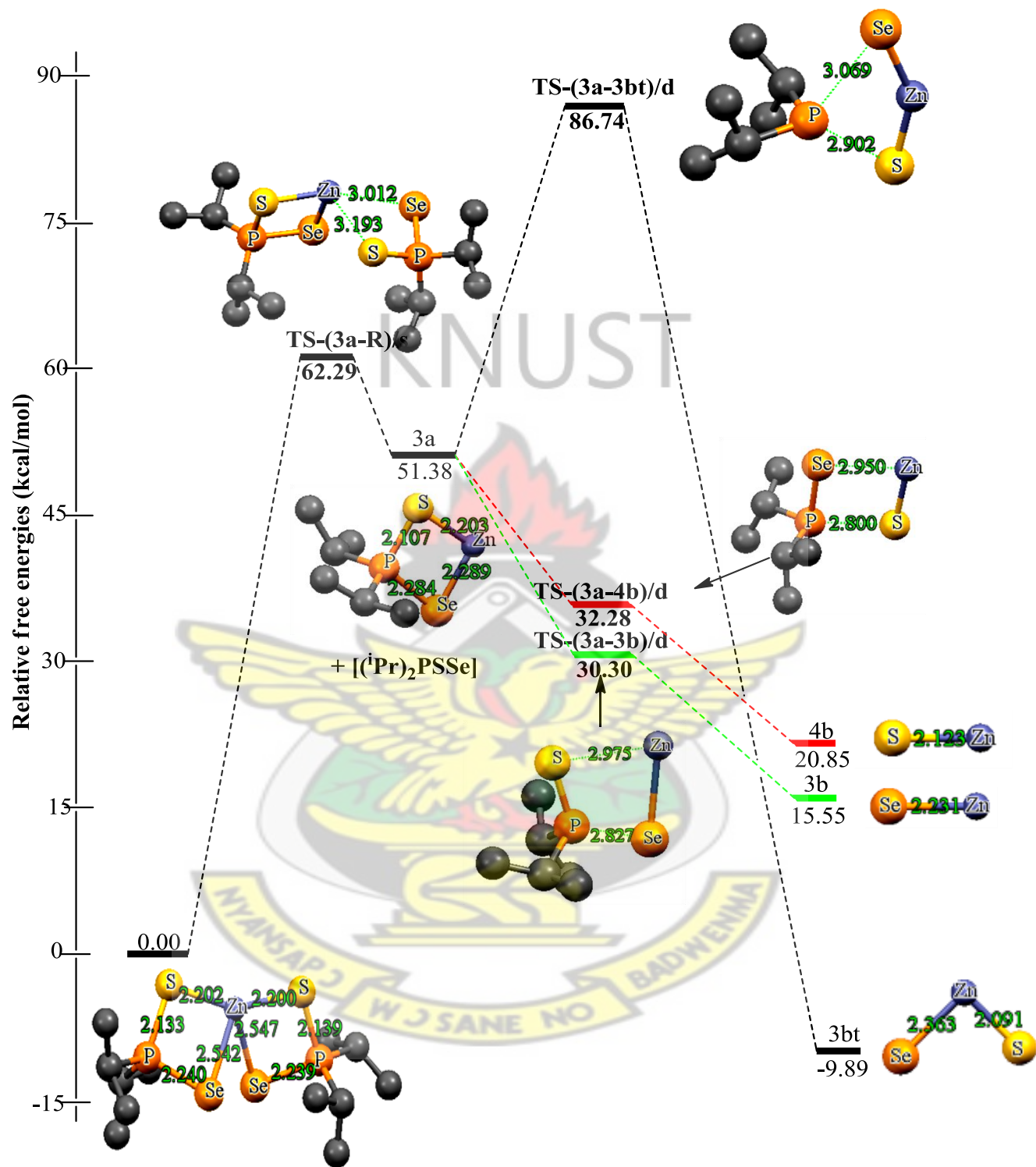


Figure 5.5: Energetics of the unimolecular decomposition pathway (3, 4) at 298.15 K. The relative free energies are in kcal/mol and bond distances in Å

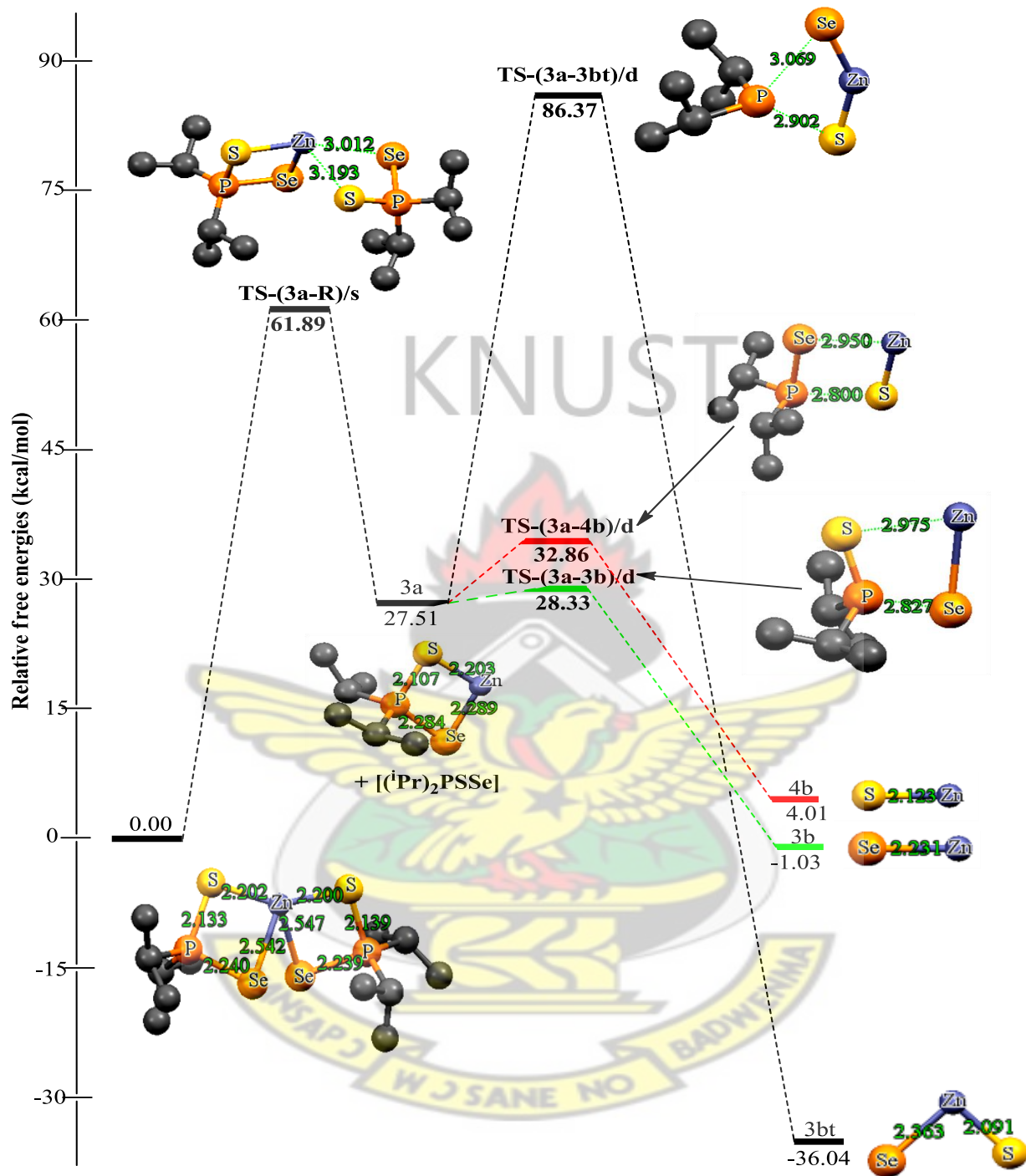


Figure 5.6: Energetics of the unimolecular decomposition pathway (3, 4) at 800 K. The relative free energies are in kcal/mol and bond distances in Å

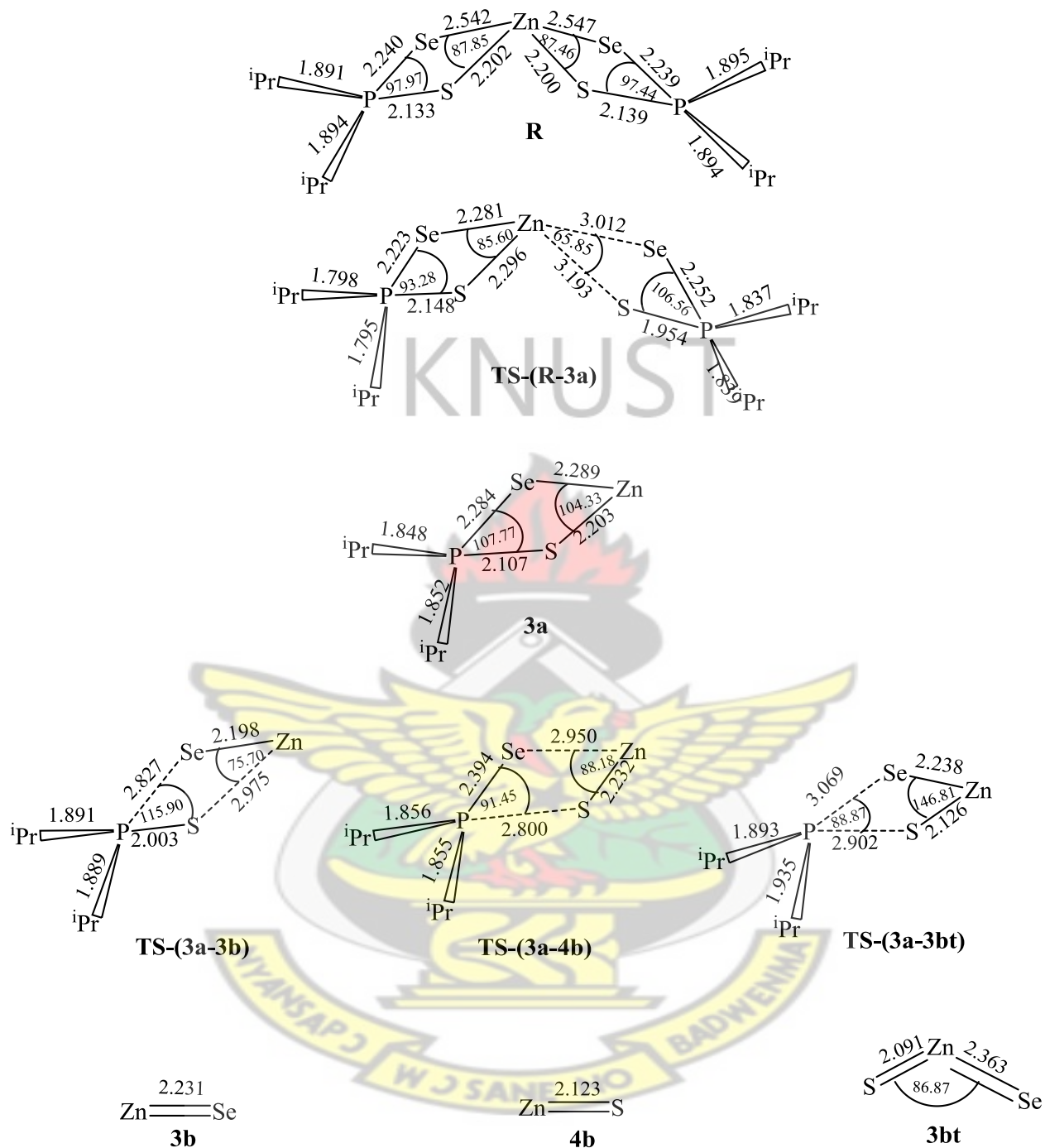


Figure 5.7: Optimized geometrical parameters of the main stationary points involved in the unimolecular decomposition pathway (3, 4). Bond distances in Å and bond angles in degrees

The reaction mechanisms involved in the unimolecular decomposition of (<sup>i</sup>Pr)<sub>2</sub>PSSe-Zn intermediate leading to the formation of zinc chalcogenides are shown in Figures 5.8 and 5.9.

The decomposition of (<sup>i</sup>Pr)<sub>2</sub>PSSe-Zn **3a** intermediate was further explored to form (<sup>i</sup>Pr)PSSe-Zn **5b** intermediate after the abstraction of isopropyl radical on the singlet PES. The activation free energy barrier involved in the formation of **5b** through the transition state **TS-(3a-5b)** was calculated as +10.91 kcal/mol (298.15 K) and +38.64 kcal/mol (800 K), and reaction free energy of -22.91 kcal/mol (298.15 K) and -3.28 kcal/mol (800 K).

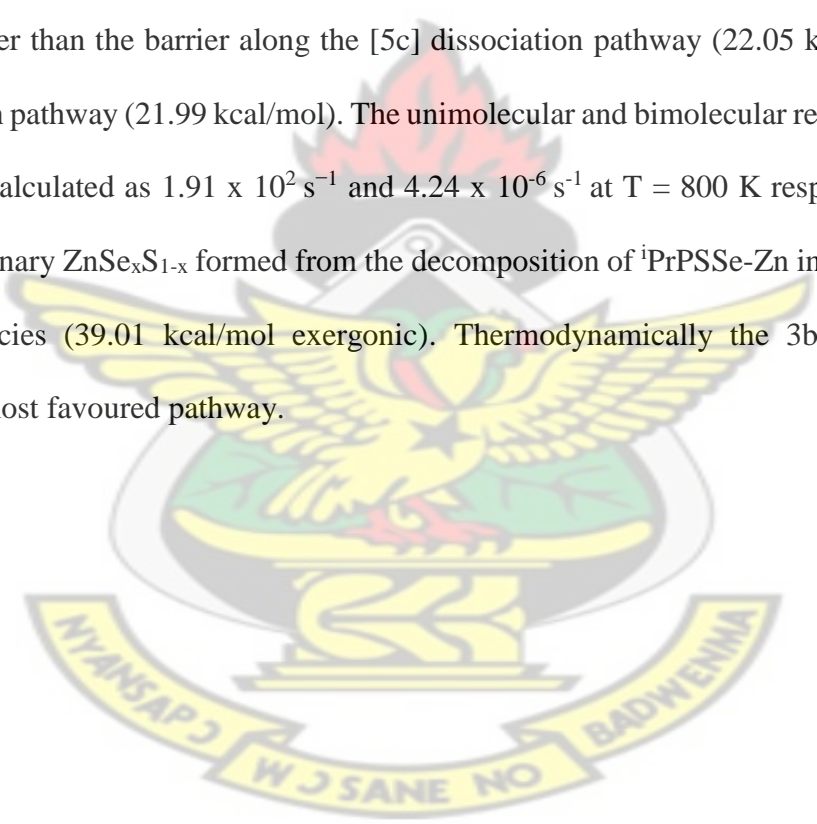
The formation of ZnSe **5c** from (<sup>i</sup>Pr)<sub>2</sub>PSSe-Zn intermediate **5b** through the transition state **TS-(3a-5c)** has been found to have an activation free energy barrier of +13.17 kcal/mol (298.15 K) and +22.05 kcal/mol (800 K), and reaction free energy of -9.51 kcal/mol (298.15 K) and -16.16 kcal/mol (800 K) on the singlet PES. The optimized geometry of **TS-(5b-5c)** further reveals the elongation of P-Se bond length from 2.352 to 2.850 Å and Zn-S bond length from 2.167 to 2.700 Å.

The activation free energy barrier involved in the formation of ZnS **6c** from (<sup>i</sup>Pr)<sub>2</sub>PSSe-Zn intermediate through the transition state **TS-(5b-6c)** was +11.34 kcal/mol (298.15 K) and +20.11 kcal/mol (800 K), with reaction free energy of -2.16 kcal/mol (298.15 K) and -9.50 kcal/mol (800 K) on the singlet PES. The optimized geometry of **TS-(5b-6c)** further reveals the elongation of Zn-Se bond length from 2.262 to 2.750 Å and P-S bond length from 2.185 to 2.650 Å.

The formation of ternary ZnSe<sub>x</sub>S<sub>1-x</sub> from (<sup>i</sup>Pr)<sub>2</sub>PSSe-Zn intermediate **5b** required the cleavage of both P-S and P-Se bonds in the phosphinato ligand. The activation free energy barrier involved in the formation of ternary ZnSe<sub>x</sub>S<sub>1-x</sub> **5ct** through the transition state **TS-(5b-5ct)** was

+13.14 kcal/mol (298.15 K) and +21.99 kcal/mol (800 K) with a reaction free energy of -22.88 kcal/mol (298.15 K) and -39.01 kcal/mol (800 K) on the singlet PES. The optimized geometry of **TS-(5b-5ct)** further reveals the elongation of P-Se bond length from 2.352 to 2.932 Å and P-S bond length from 2.185 to 2.757 Å.

On the singlet PES, the [6c] dissociation pathway to form ZnS from (<sup>i</sup>Pr)PSSe-Zn intermediate is kinetically favoured over [5c] dissociation pathway to form ZnSe and [5ct] dissociation pathway to form ternary ZnSe<sub>x</sub>S<sub>1-x</sub>. The barrier along [6c] dissociation pathway (20.11 kcal/mol) is lower than the barrier along the [5c] dissociation pathway (22.05 kcal/mol) and the [5ct] dissociation pathway (21.99 kcal/mol). The unimolecular and bimolecular recombination rate constants were calculated as  $1.91 \times 10^2 \text{ s}^{-1}$  and  $4.24 \times 10^{-6} \text{ s}^{-1}$  at T = 800 K respectively. On the reaction PES, ternary ZnSe<sub>x</sub>S<sub>1-x</sub> formed from the decomposition of <sup>i</sup>PrPSSe-Zn intermediate is the most stable species (39.01 kcal/mol exergonic). Thermodynamically the 3bt decomposition pathway is the most favoured pathway.



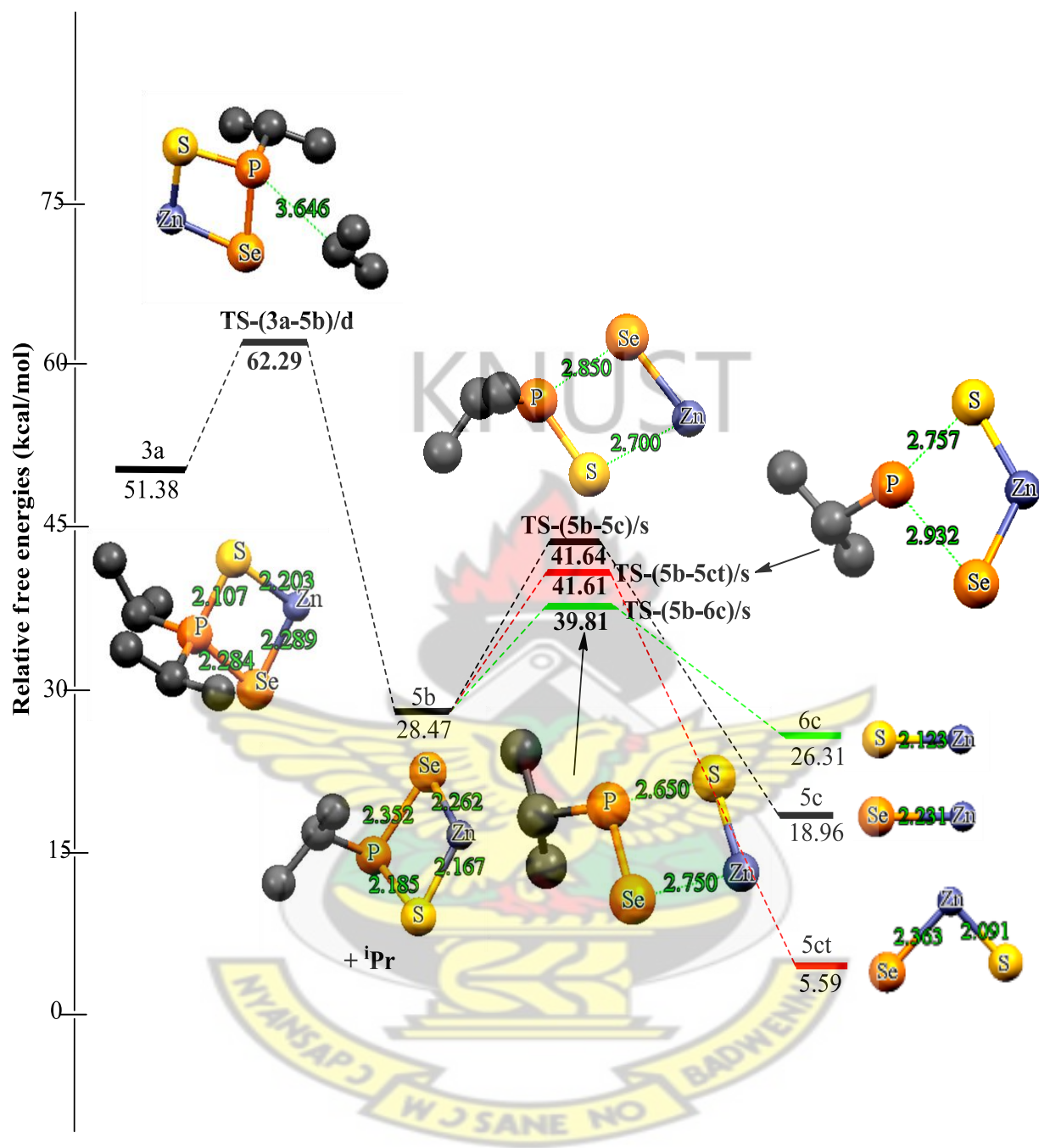


Figure 5.8: Energetics of the unimolecular decomposition pathway (5, 6) at 298.15 K. The relative free energies are in kcal/mol and bond distances in Å

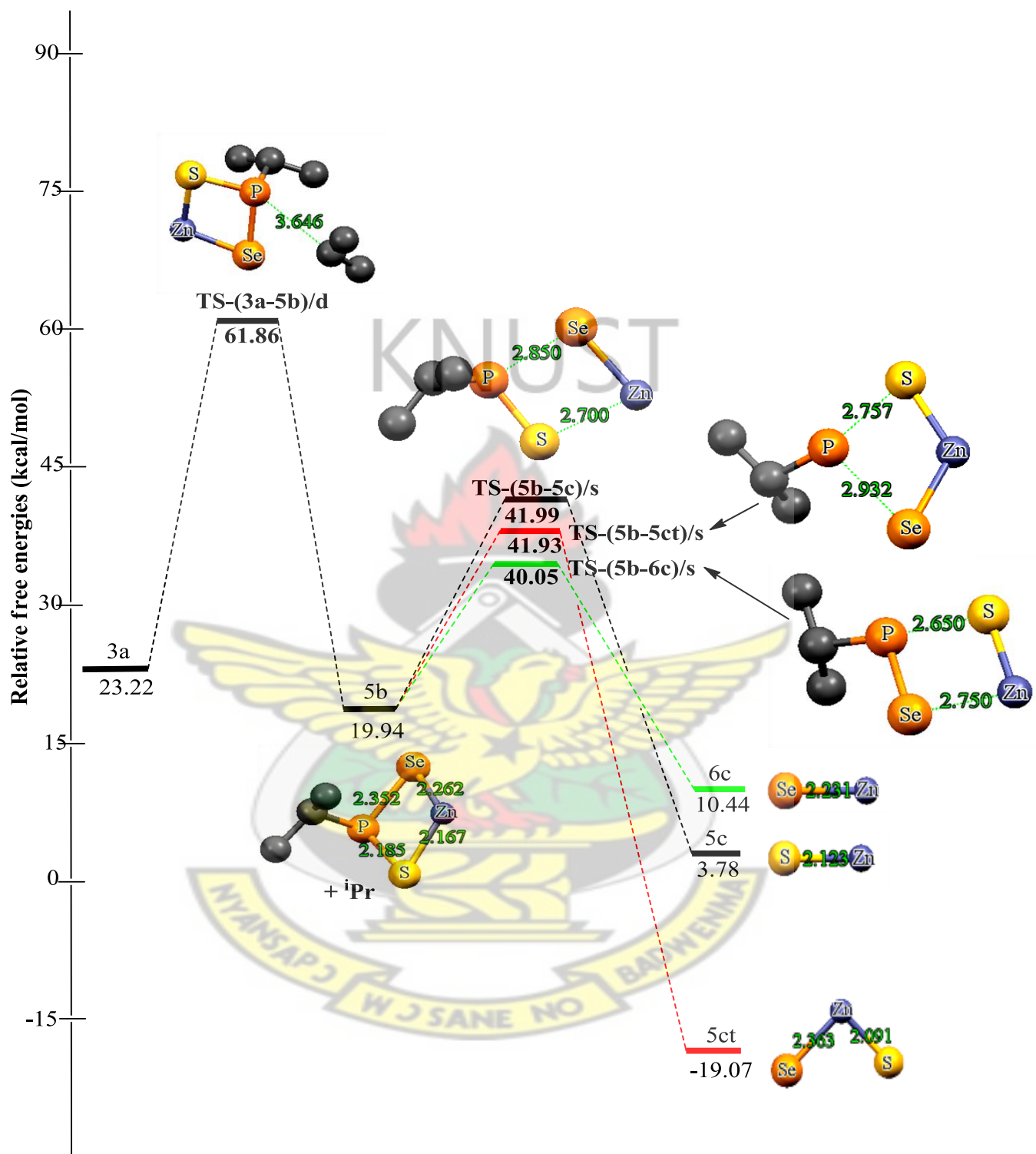


Figure 5.9: Energetics of the unimolecular decomposition pathway (5, 6) at 800 K. The relative free energies are in kcal/mol and bond distances in Å

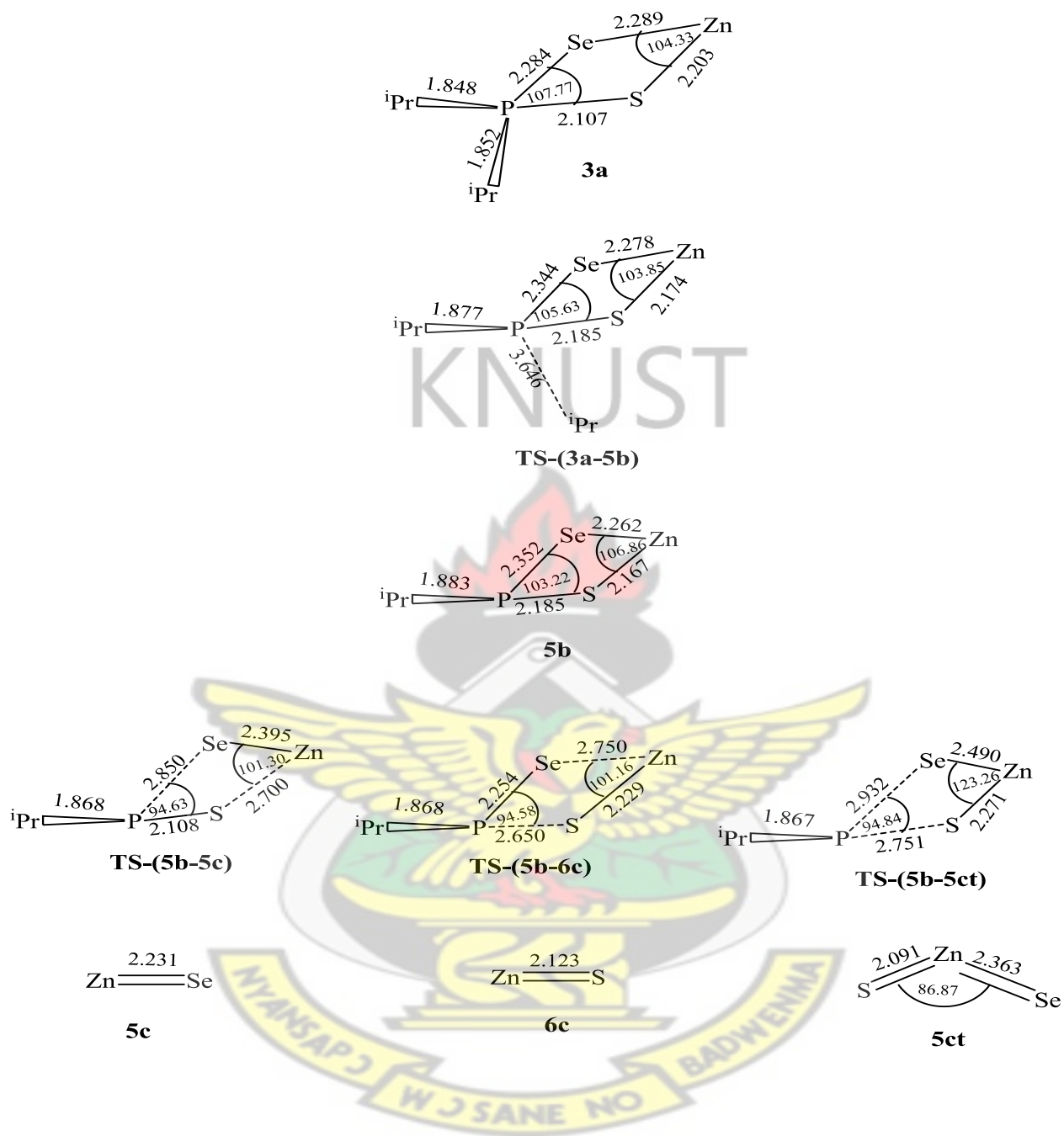


Figure 5.10: Optimized geometrical parameters of the main stationary points involved in the unimolecular decomposition pathway (5, 6). Bond distances in Å and bond angles in degrees

Table 5.2: Calculated rate constants for selected individual steps involve in the decomposition of Zn[(<sup>1</sup>Pr)<sub>2</sub>PSSe]<sub>2</sub> precursor at room temperature (298.15 K) and at an elevated temperature (800 K)

Reaction pathway	k <sub>uni</sub> (s <sup>-1</sup> )		k <sub>eq</sub>		k <sub>rec</sub> (s <sup>-1</sup> )	
	298.15 K	800 K	298.15 K	800 K	298.15 K	800 K
1c → 1d	6.51 x 10 <sup>-33</sup>	2.93 x 10 <sup>-4</sup>	5.40 x 10 <sup>5</sup>	1.05 x 10 <sup>14</sup>	3.52 x 10 <sup>-27</sup>	3.08 x 10 <sup>10</sup>
2c → 2d	2.21 x 10 <sup>-33</sup>	2.57 x 10 <sup>-4</sup>	4.01 x 10 <sup>1</sup>	7.08 x 10 <sup>12</sup>	8.86 x 10 <sup>-32</sup>	1.82 x 10 <sup>9</sup>
1c → 1dt	1.86 x 10 <sup>-40</sup>	2.69 x 10 <sup>-7</sup>	6.57 x 10 <sup>6</sup>	3.70 x 10 <sup>25</sup>	1.22 x 10 <sup>-33</sup>	9.95 x 10 <sup>18</sup>
2c → 2dt	4.82 x 10 <sup>-36</sup>	1.58 x 10 <sup>-5</sup>	6.03 x 10 <sup>11</sup>	2.08 x 10 <sup>30</sup>	2.91 x 10 <sup>-24</sup>	3.29 x 10 <sup>25</sup>
3a → 3b	1.06 x 10 <sup>-08</sup>	3.02 x 10 <sup>5</sup>	3.99 x 10 <sup>-12</sup>	5.69 x 10 <sup>6</sup>	4.23 x 10 <sup>-20</sup>	1.72 x 10 <sup>12</sup>
3a → 4b	5.16 x 10 <sup>-12</sup>	1.76 x 10 <sup>4</sup>	5.20 x 10 <sup>-16</sup>	1.15 x 10 <sup>-3</sup>	2.68 x 10 <sup>-27</sup>	2.02 x 10 <sup>1</sup>
3a → 3bt	1.67 x 10 <sup>-51</sup>	3.31 x 10 <sup>-11</sup>	1.78 x 10 <sup>7</sup>	2.62 x 10 <sup>26</sup>	2.97 x 10 <sup>-44</sup>	8.67 x 10 <sup>15</sup>
5b → 5c	1.83 x 10 <sup>-18</sup>	5.69 x 10 <sup>1</sup>	7.98 x 10 <sup>-5</sup>	1.70 x 10 <sup>-3</sup>	1.46 x 10 <sup>-22</sup>	9.67 x 10 <sup>-2</sup>
5b → 6c	4.08 x 10 <sup>-17</sup>	1.91 x 10 <sup>2</sup>	1.26 x 10 <sup>-14</sup>	2.22 x 10 <sup>-8</sup>	5.14 x 10 <sup>-31</sup>	4.24 x 10 <sup>-6</sup>
5b → 5ct	1.95 x 10 <sup>-18</sup>	5.85 x 10 <sup>1</sup>	7.98 x 10 <sup>-5</sup>	9.53 x 10 <sup>13</sup>	1.56 x 10 <sup>-22</sup>	5.58 x 10 <sup>15</sup>

Hammond's postulate can be interpreted in terms of the position of transition state along the reaction coordinate,  $n_T$ , as defined by Agmon (Serrano *et al.*, 2008);

$$n_T = \frac{1}{2 - \left(\frac{\Delta G^0}{\Delta G^\ddagger}\right)} \quad (5.3)$$

The values of  $n_T$  for the thermal decomposition of Zn[(<sup>1</sup>Pr)<sub>2</sub>PSSe]<sub>2</sub> precursor is given in Table 5.3.

In fact, the similarity between the reactants, intermediates, and products increases with respect to the reaction in the order of 4b > 3b > 6c > 5c-5ct > 2d > 3bt-1d > 1dt > 2dt, and 6c > 4b > 5c > 3b > 2d-1d > 3bt > 5ct-1dt > 2dt at T = 298.15 K and 800 K respectively.

These results imply that the transition structures involved in the formation of ZnSe **5c** and ZnS **6c** have a larger similarity to the product than the other reactions pathway at T = 298.15 K and 800 K respectively.

Table 5.3: Position of the transition structures ( $n_T$ ) for selected individual steps

Reaction pathway	298.15 K	800 K
1c → 1d	0.470047	0.432541
2c → 2d	0.491284	0.437664
1c → 1dt	0.469528	0.402993
2c → 2dt	0.445463	0.380669
3a → 3b	0.689127	0.491076
3a → 4b	0.732441	0.532491
3a → 3bt	0.473027	0.414010
5b → 5c	0.535967	0.523566
5b → 6c	0.656281	0.574935
5b → 5ct	0.536004	0.407364

## 5.5 Conclusion

The decomposition of Zn[(<sup>i</sup>Pr)<sub>2</sub>PSSe]<sub>2</sub> precursor was studied by using density functional theory (DFT) calculations both at room temperature (298.15 K) and elevated temperature (800 K) to verify the nature of the reaction mechanisms. Computational thermochemistry have been undertaken in order to determine the most thermodynamically and kinetically viable mechanistic

pathways involved in the thermal decomposition of the precursor. The following conclusions are drawn from the results presented.

1. On the singlet PES, the decomposition of (<sup>i</sup>Pr)PSSe-Zn-S intermediate leading to the formation of ternary ZnSe<sub>x</sub>S<sub>1-x</sub> was thermodynamically favoured, but the reaction is kinetically slow by the highest activation barrier. The unimolecular and bimolecular recombination rate constants were calculated as  $1.58 \times 10^{-5} \text{ s}^{-1}$  and  $3.29 \times 10^{25} \text{ s}^{-1}$  at T = 800 K respectively.
2. The calculation indicate that on the singlet PES, the decomposition of (<sup>i</sup>Pr)PSSe-Zn intermediate leading to ZnS formation, is proposed as the most probable decomposition mechanism. The unimolecular and bimolecular recombination rate constants were calculated as  $1.91 \times 10^2 \text{ s}^{-1}$  and  $4.24 \times 10^{-6} \text{ s}^{-1}$  at T = 800 K respectively.
3. On the doublet PES, the decomposition of (<sup>i</sup>Pr)<sub>2</sub>PSSe-Zn intermediate leading to the formation of ternary ZnSe<sub>x</sub>S<sub>1-x</sub> was thermodynamically favoured, but the reaction is kinetically slow by the highest activation barrier. However the formation of ZnSe from (<sup>i</sup>Pr)<sub>2</sub>PSSe-Zn intermediate, is proposed as the most probable decomposition mechanism. The unimolecular and bimolecular recombination rate constants were calculated as  $3.02 \times 10^5 \text{ s}^{-1}$  and  $1.72 \times 10^{12} \text{ s}^{-1}$  at T = 298.15 K respectively.
4. The value of  $n_T$  for the decomposition of (<sup>i</sup>Pr)PSSe-Zn reveals that the transition state structure involved in the formation of ZnS has a larger similarity to the product than the other reactions pathway at T = 800 K.

## References

- Akhtar, J., Afzaal, M., Vincent, M., Burton, N., Raftery, J., Hillier, I. and O'Brien, P. (2011). "Understanding the Decomposition Pathways of Mixed Sulphur/Selenium Lead Phosphinato Precursor Explaining the Formation of Lead Selenide". *J. Phys. Chem. C*, 115(34): 16904-16909.
- Bhargava, R. N., Gallagher, D., Hong, X. and Nurmikko, D. (1994). "Optical properties of manganese doped nanocrystals of zinc sulphide". *Phys. Rev. Lett.*, 72: 416–419.
- Elidrissi, B., Addou, M., Regragui, M., Bougrine, A., Kachoune, A. and Bernecde, J. C. (2001). "Structure, composition and optical properties of ZnS thin films prepared by spray pyrolysis". *Mater. Chem. Phys.*, 68: 175–179.
- Gao, X. D., Li, X. M. and Yu, W. D. (2004). "Morphology and optical properties of amorphous ZnS films deposited by ultrasonic-assisted successive ionic layer adsorption and reaction method". *Thin Solid Films*, 468: 43–47.
- Gunshor, R. L. and Nurmikko, A. V. (1997). *II–VI blue/green light emitters: devices physics and epitaxial growth. Semiconductor and Semimetals*, vol. 44, Academic press, New York.
- Koch, W. and Holthansen, M. C. (2001). *A Chemist Guide to Density Functional Theory*, 2nd Ed., Wiley-VCH, Weinheim, Federal Republic of Germany.
- Nicolau, Y.F., Dupuy, M. and Bruel, M. (1998). "Solution growth of ZnS, CdS and  $Zn_{1-x}Cd_xS$  thin films deposited by the successive ion layer adsorption and reaction process". *J. Electrochem. Soc.*, 137: 2915–2924.

## CHAPTER SIX

### DENSITY FUNCTIONAL THEORY (DFT) STUDY OF THE DECOMPOSITION OF Cd[(<sup>1</sup>Pr)<sub>2</sub>PSSe]<sub>2</sub> SINGLE-SOURCE PRECURSOR FOR THE CHEMICAL VAPOUR DEPOSITION OF BINARY AND TERNARY CADMIUM CHALCOGENIDES

#### Abstract

The thermal decomposition of Cd[(<sup>1</sup>Pr)<sub>2</sub>PSSe]<sub>2</sub> single-source precursor in the gas-phase have been explored and the geometries of the species involved were optimized by employing density functional theory calculation at the MO6/LACVP\* level of theory. The Gibbs free energy and activation free energy barrier for all the reaction mechanisms involved in the decomposition process were calculated, both at 298.15 K and 800 K. The results indicate the steps that lead to CdSe formation on both singlet and doublet potential energy surface is favoured kinetically over those that lead to CdS and CdSe<sub>x</sub>S<sub>1-x</sub> formation. Thermodynamically, the steps that lead to ternary CdSe<sub>x</sub>S<sub>1-x</sub> formation are more favourable than those that lead to CdSe and CdS formation on both the singlet and the doublet PES. Density functional theory calculations of the formation of ternary CdSe<sub>x</sub>S<sub>1-x</sub> are consistent with a dominant role on thermodynamic grounds rather than kinetic ones in controlling the material formed during the deposition process.

**Keywords:** Thermal decomposition, single-source precursor, gas phase, potential energy surface, density functional theory

## 6.1 Introduction

Cadmium selenide is an interesting member of the II-VI semiconductor family, owing to their unique chemical and physical properties (Xia *et al.*, 2003). CdSe nanocrystalline semiconductors have attracted great interest over the past years because their properties and applications such as light-emitting diodes, lasers, holographic optical memories, photonic band-gap crystals, ultrafast photonic switches, and biomedical tags for fluoroimmuno assays, nanosensors and biological imaging (Bruchez *et al.*, 1998). Cadmium sulphide shows great potential for uses in photochemical catalysis, solar cells, and nonlinear optical materials (Ma *et al.*, 2007), and could be used as bioorganic detector of proteins (Tan *et al.*, 2004) or DNA (Mahtab *et al.*, 1995; 1996).

The single-molecule precursor has some distinct advantages over conventional dual source precursors including low toxicity and limited premature reaction. The use of traditional gaseous and hazardous organometallic precursors for the growth of solid-state materials is a matter of concern. In order to overcome such problems, precursors in which the elements of a binary semiconductor are within a single molecule are of considerable interest (Gleizes, 2000). The use of single-source precursors for the synthesis of metal chalcogenide nanoparticles has proven to be efficient routes for the synthesis of high quality nanocrystals. Ligands properties of the metal precursor used as precursor could be used in the modification of the size and shape of the nanoparticles.

Much of the early work was performed on the readily prepared phenyl derivatives (Bhattacharyya *et al.*, 1995). Since the isopropyl derivative is of paramount interest in metal precursor that may serve as single-source precursors of metal chalcogenide thin films (Kim *et al.*,

2003; Green *et al.*, 2003). In CVD applications, precursors of isopropyl derivatives are better in view of their higher volatility as compared to those of the phenyl-substituted derivatives (Afzaal *et al.*, 2002).

The optimization of the CVD condition for obtaining higher quality films, better conformity or higher (optimal) film growth rate requires knowledge of the deposition chemistry, which can be obtained from specially designed experiments or/and modeling and simulation. Experiments provide the most reliable results, but they are expensive and time and material consuming. Recent developments of quantum chemical methods, particularly density functional theory (DFT), and fast progress in software and hardware development have provided first principles (*ab initio*) theoretical quantum chemistry approaches as an alternative to experiments in some areas of CVD modeling.

Although studies performed by Akhtar *et al.* (2011) allow us to rationalize a mechanism for the gas phase decomposition of  $\text{Cd}[(i\text{Pr})_2\text{PSSe}]_2$  single-source precursor. In this work several reaction mechanisms for the gas phase decomposition of  $\text{Cd}[(i\text{Pr})_2\text{PSSe}]_2$  precursor were explored by employing density functional theory method at the MO6/LACVP\* level of theory and also to investigate the possible mechanistic channels for the formation of an ternary phase.

## 6.2 Details of calculations

All calculations were done using the same method in section 3.2.

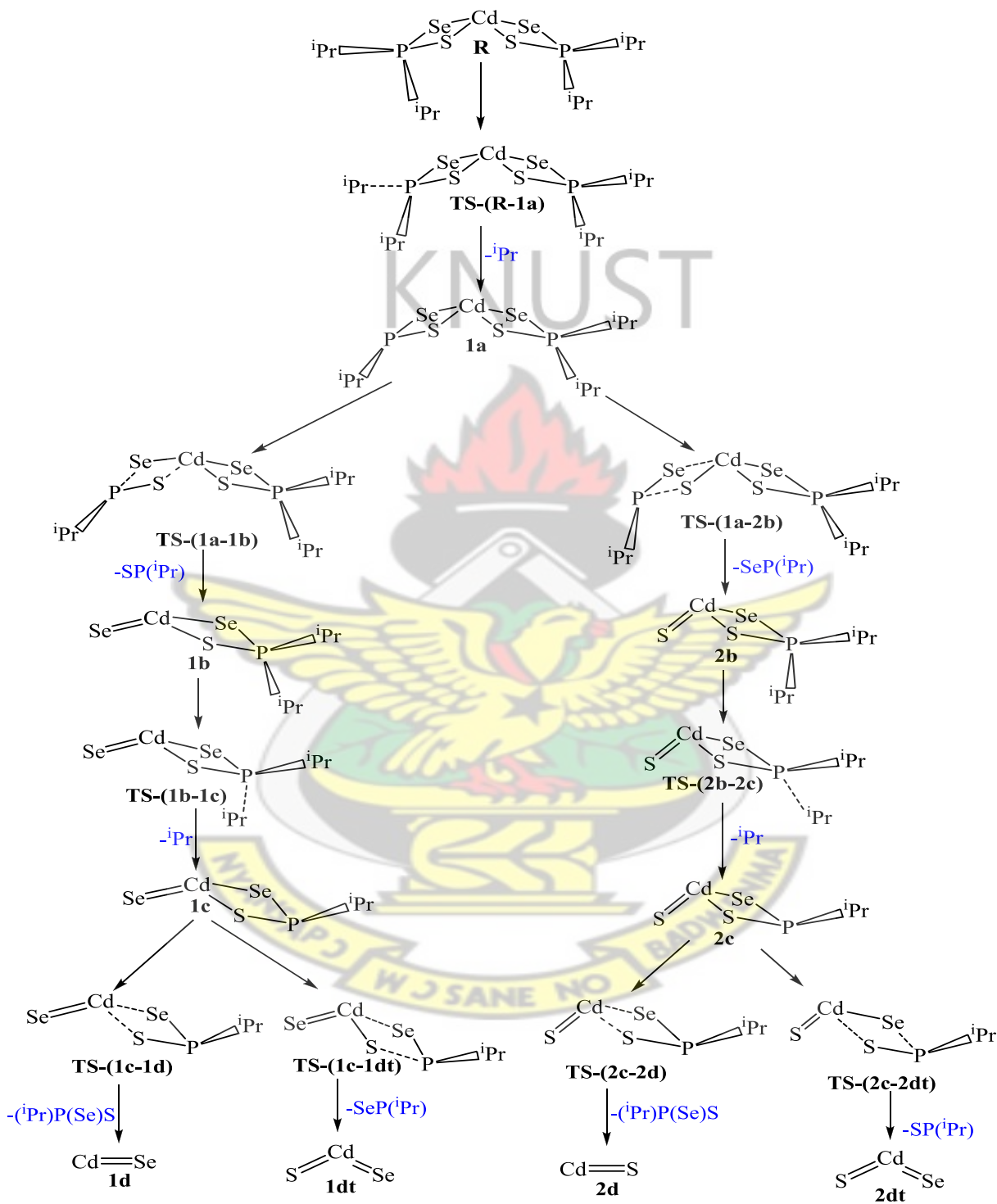
### 6.3 Mechanistic considerations

A number of different thermal decomposition pathways as suggested in section 3.3 were investigated for  $\text{Cd}[(^1\text{Pr})_2\text{PSSe}]_2$  precursor.

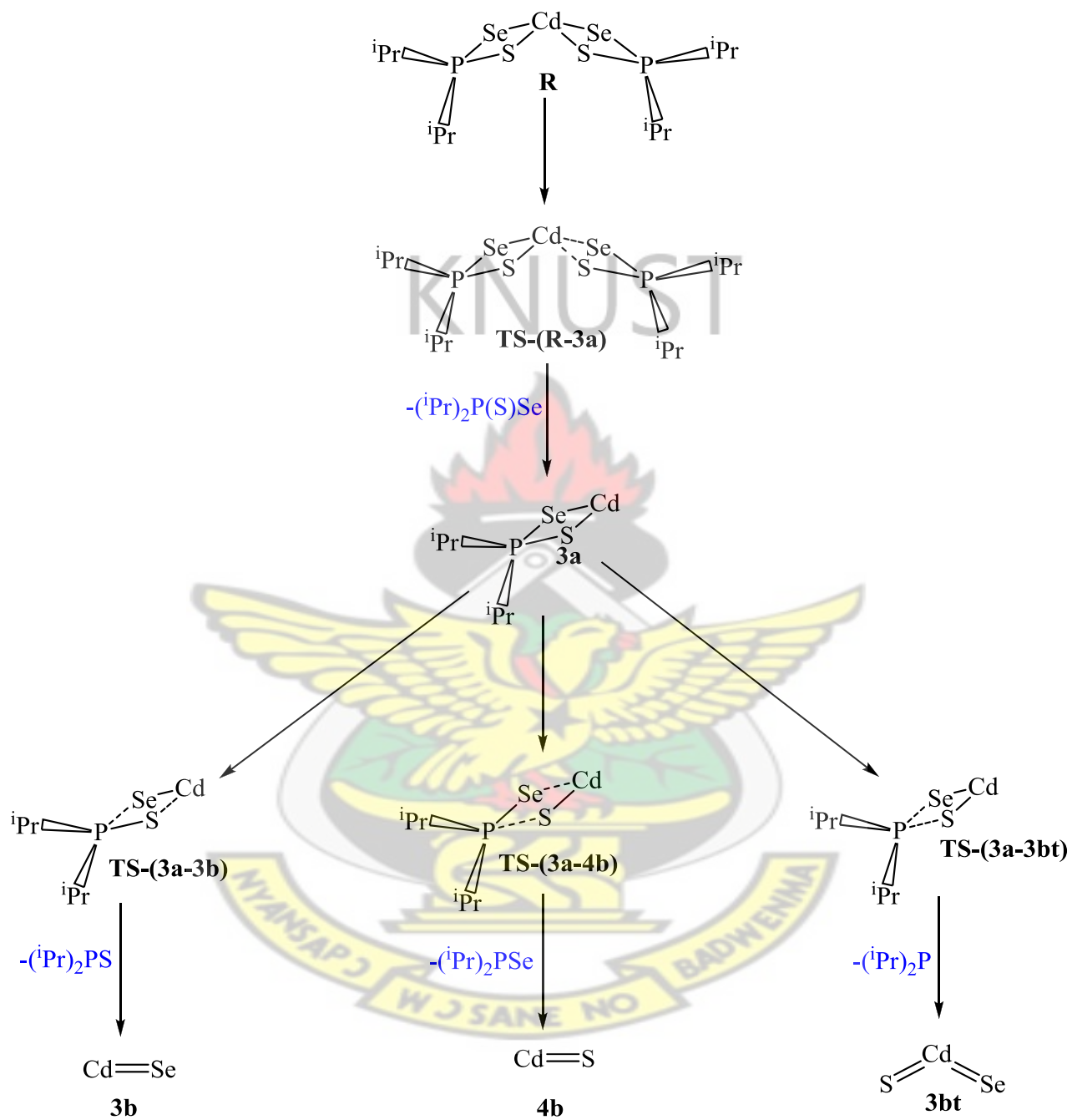
# KNUST



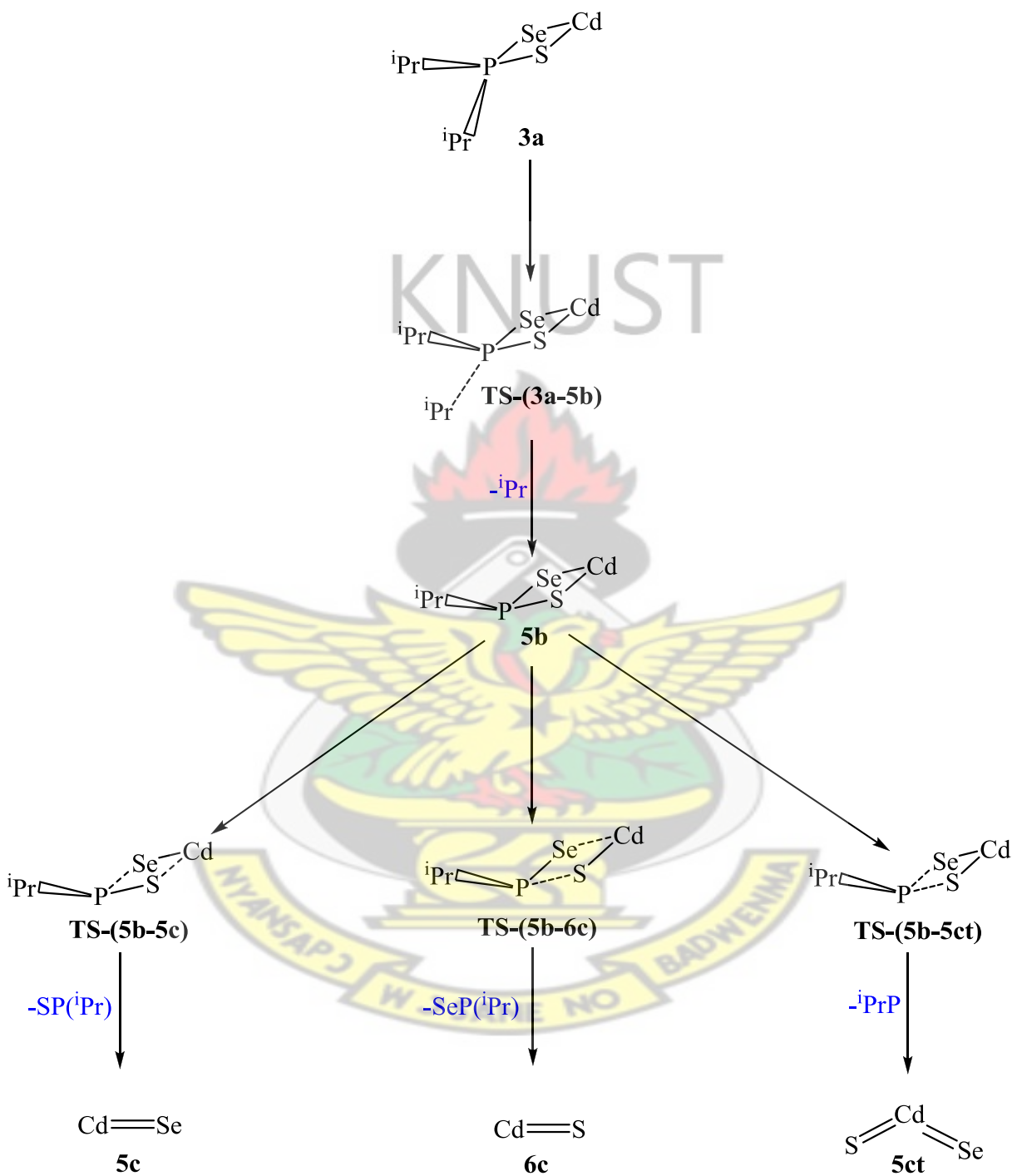
Scheme 6.1: Decomposition pathway (1, 2) of Cd[(<sup>i</sup>Pr)<sub>2</sub>PSSe]<sub>2</sub> precursor



Scheme 6.2: Decomposition pathway (3, 4) of  $\text{Cd}[(i\text{Pr})_2\text{PSSe}]_2$  precursor



Scheme 6.3: Decomposition pathway (5, 6) of Cd[(*i*Pr)<sub>2</sub>PSSe]<sub>2</sub> precursor



## 6.4 Results and discussion

### 6.4.1 Optimized Geometry of $\text{Cd}[(^i\text{Pr})_2\text{PSSe}]_2$ precursor

Optimized bond lengths and bond angles are given in Table 6.1. To the best of our knowledge there are no reports for the use  $\text{Cd}[(^i\text{Pr})_2\text{PSSe}]_2$  complexes as a single source precursor for the deposition of cadmium chalcogenide thin films or nanoparticles. Cadmium has a distorted tetrahedral geometry with the ligand bond angles of  $83.45^\circ$  and  $83.30^\circ$ , but the angles are smaller than the perfect tetrahedral angle. The two sulphur and two selenium atoms are at the corners of the tetrahedron. The density functional theory (DFT) geometry optimization of  $\text{Cd}[(^i\text{Pr})_2\text{PSSe}]_2$  precursor on a singlet potential energy surface (PES) has an average bond length of  $2.51 \text{ \AA}$  (Cd-S), which are smaller than the bond length of Cd-Se ( $2.54 \text{ \AA}$ ).

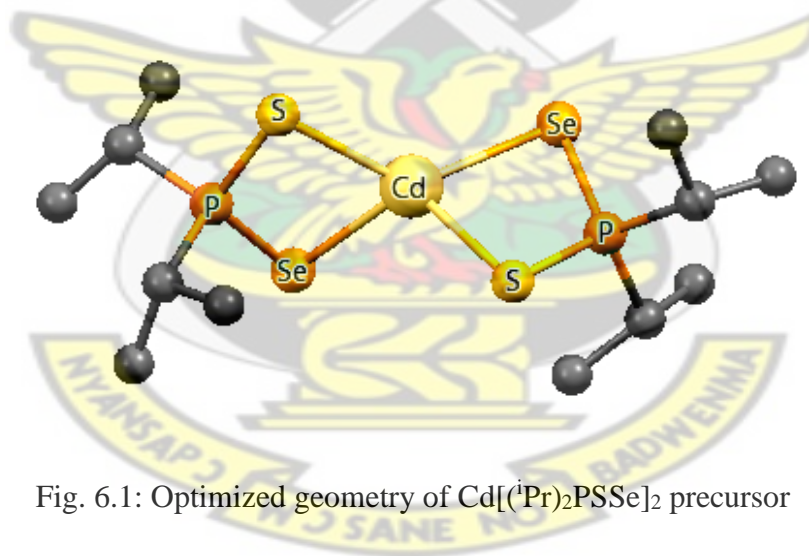


Fig. 6.1: Optimized geometry of  $\text{Cd}[(^i\text{Pr})_2\text{PSSe}]_2$  precursor

Table 6.1: Selected bond lengths (Å) and bond angles (°) of Cd[(<sup>i</sup>Pr)<sub>2</sub>PSSe]<sub>2</sub> precursor

Bonds	length(Å)	bonds	angles (°)
P-Se	2.1965	Se-P-S	112.34
P-S	2.0682	S-P-Se	112.17
S-P	2.0683	Se-Cd-S	83.45
Se-P	2.1966	S-Cd-Se	83.30
Cd-Se	2.8101	Se-Cd-Se	124.93
Cd-S	2.5076	S-Cd-S	119.64
Se-Cd	2.8106	Se-Cd-S	116.44
S-Cd	2.5075	S-Cd-Se	133.00

#### 6.4.2 Overall Decomposition of Cd[(<sup>i</sup>Pr)<sub>2</sub>PSSe]<sub>2</sub> precursor

The free energies of the transition states relative to the reactant(s) and their corresponding intermediates involved in the decomposition pathway (1, 2), both at room temperature (298.15 K) and elevated temperature (800 K) are shown in Figures 6.2 and 6.3.

The formation of **1a** intermediate from the reactant **R** through transition state **TS-(R-1a)** has an activation free energy barrier of +77.88 kcal/mol (298.15 K) and +76.72 kcal/mol (800 K) and endergonic by 52.50 kcal/mol (298.15 K) and 23.48 kcal/mol (800 K) on the doublet PES.

The transition state (**TS-(1a-1b)**) in Scheme 6.1) involved in the decomposition of **1a** to form (<sup>i</sup>Pr)<sub>2</sub>PSSe-Cd-Se **1b** intermediate has an activation free energy barrier of +9.91 kcal/mol (298.15 K) and +38.73 kcal/mol (800 K) and reaction free energy of -19.82 kcal/mol (298.15 K)

and -21.94 kcal/mol (800 K) on the doublet PES. The **1a** intermediate can also decompose to form (<sup>i</sup>Pr)<sub>2</sub>PSSe-Cd-S **2b** intermediate through transition state **TS-(2a-2b)** on the doublet PES. The activation free energy barrier for this process was +13.22 kcal/mol (298.15 K) and +42.55 kcal/mol (800 K), and reaction free energy of -10.26 kcal/mol (298.15 K) and -13.21 kcal/mol (800 K).

As shown in Figures 6.2 and 6.3, if the reaction proceeds from the **1b** intermediate through the transition state **TS-(1b-1c)** to form (<sup>i</sup>Pr)PSSe-Cd-Se **1c** intermediates on the singlet PES, the activation free energy barrier was +22.66 kcal/mol (298.15 K) and +53.65 kcal/mol (800 K) with a reaction free energy of +7.64 kcal/mol (298.15 K) and +10.25 kcal/mol (800 K). If on the other hand, it proceeds from the **2b** intermediate through the transition state **TS-(2b-2c)** to form (<sup>i</sup>Pr)PSSe-CdS **2c** intermediate on the singlet PES, the activation free energy barrier was +9.06 kcal/mol (298.15 K) and +43.54 kcal/mol (800 K) with a reaction free energy of -4.51 kcal/mol (298.15 K) and -1.04 kcal/mol (800 K).

The singlet transition states (**TS-(1c-1d)** in Scheme 6.1) involved in the decomposition of (<sup>i</sup>Pr)PSSe-Cd-Se **1c** intermediate to form a singlet CdSe **1d** has activation free energy barrier of +5.14 kcal/mol (298.15 K) and +33.65 kcal/mol (800 K) and reaction free energy of -43.10 kcal/mol (298.15 K) and -30.92 kcal/mol (800 K). The optimized geometry of **TS-(1c-1d)** further reveals the elongation of Cd-Se bond length from 2.639 to 3.134 Å and Cd-S bond length from 2.542 to 2.919 Å. The formation of ternary CdSe<sub>x</sub>S<sub>1-x</sub> **1dt** along the **1c** pathway through a transition state **TS-(1c-1dt)** has activation free energy barrier of +12.75 kcal/mol (298.15 K) and +41.35 kcal/mol (800 K) and exergonic by 47.64 kcal/mol (298.15 K) and 44.82 kcal/mol (800 K) on the singlet PES. The optimized geometry of **TS-(1c-1dt)** further reveals the elongation of Cd-Se bond length from 2.639 to 3.253 Å and P-S bond length from 2.148 to 2.958 Å.

Also, the decomposition of (<sup>i</sup>Pr)PSSe-Cd-S intermediate **2c** to form CdS **2d** through transition state **TS-(2c-2d)** has an activation free energy barrier of +1.22 kcal/mol (298.15 K) and +29.87 kcal/mol (800 K), and reaction free energy of -38.29 kcal/mol (298.15 K) and -26.21 kcal/mol (800 K) on the singlet PES. The optimized geometry of **TS-(2c-2d)** further reveals the elongation of Cd-Se bond length from 2.544 to 3.100 Å and Cd-S bond length from 3.132 to 3.367 Å. The transition state **TS-(2c-2dt)** along the **2c** pathway has a barrier of +30.84 kcal/mol (298.15 K) and +59.43 kcal/mol (800 K), and exergonic by 52.03 kcal/mol (298.15 K) and 48.43 kcal/mol (800 K) on the singlet PES. The optimized geometry of **TS-(2c-2dt)** further reveals the elongation of Cd-S bond length from 3.132 to 3.293 Å and P-Se bond length from 2.301 to 2.972 Å.

On the singlet PES, the decomposition of <sup>i</sup>PrPSSe-Cd-S/Se intermediates reveal that, the [2d] elimination of <sup>i</sup>PrP(Se)S from <sup>i</sup>PrPSSe-Cd-S intermediate to form CdS has the lowest barrier (29.87 kcal/mol) compared to [1dt] elimination from <sup>i</sup>PrPSSe-Cd-Se intermediate (41.35 kcal/mol), [2dt] elimination from <sup>i</sup>PrPSSe-Cd-S intermediate (59.43 kcal/mol), and [1d] elimination from <sup>i</sup>PrPSSe-Cd-Se intermediate to form CdSe (33.65 kcal/mol). The unimolecular and recombination rate constants for the 2d decomposition pathway were  $6.44 \times 10^1 \text{ s}^{-1}$  and  $6.76 \times 10^{15} \text{ s}^{-1}$  at  $T = 800 \text{ K}$  respectively. Kinetically the 2d decomposition pathway is the most favoured pathway.

The ternary  $\text{CdSe}_x\text{S}_{1-x}$  [2dt] formed from optimization of the <sup>i</sup>PrPSSe-Cd-S intermediate is the most stable species on the reaction PES (48.43 kcal/mol exergonic). Thermodynamically the most favoured pathway is the 2dt decomposition pathway.

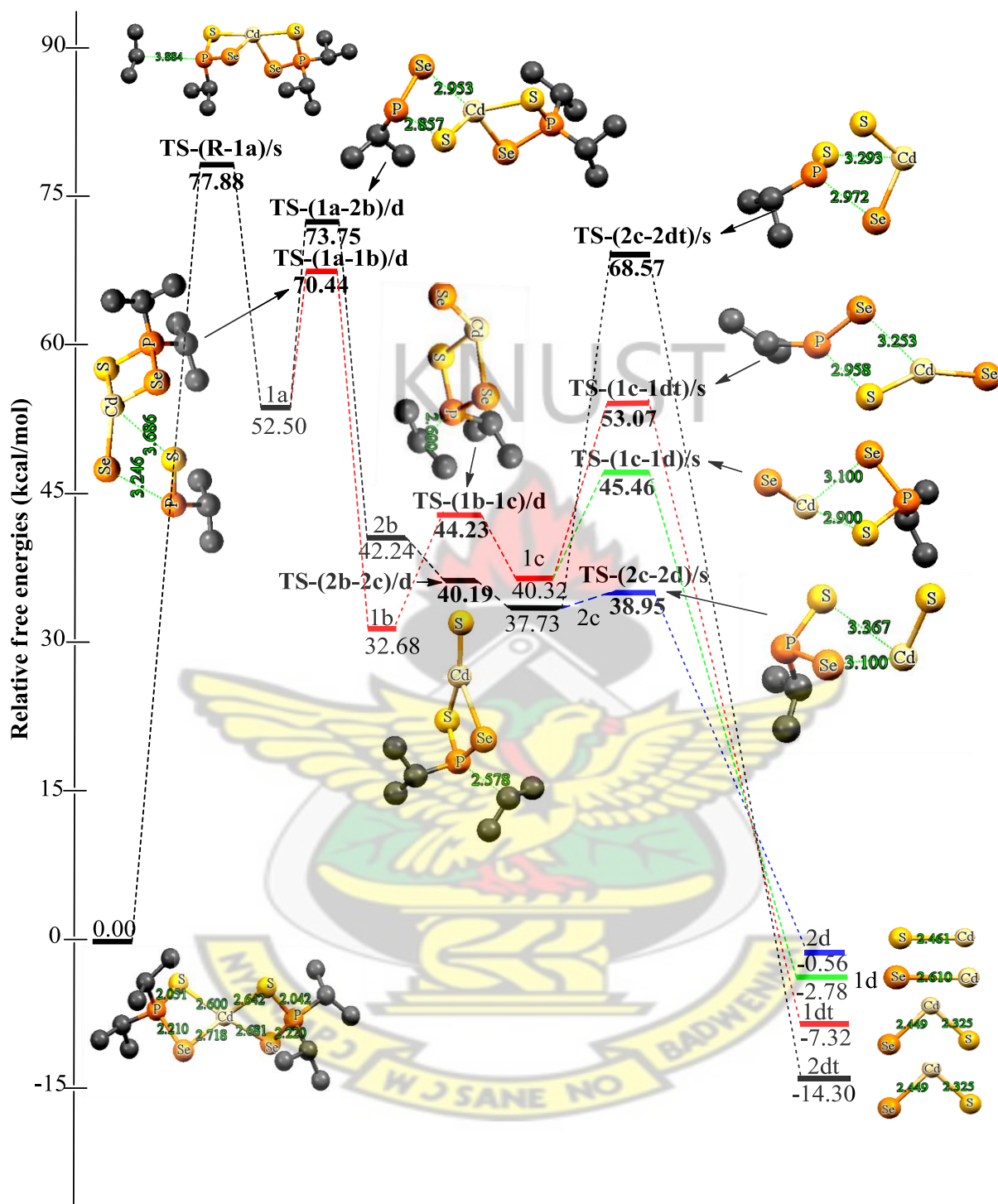


Figure 6.2: Energetics of the unimolecular decomposition pathway (1, 2) at 298.15 K. The relative free energies are in kcal/mol and bond distances in Å

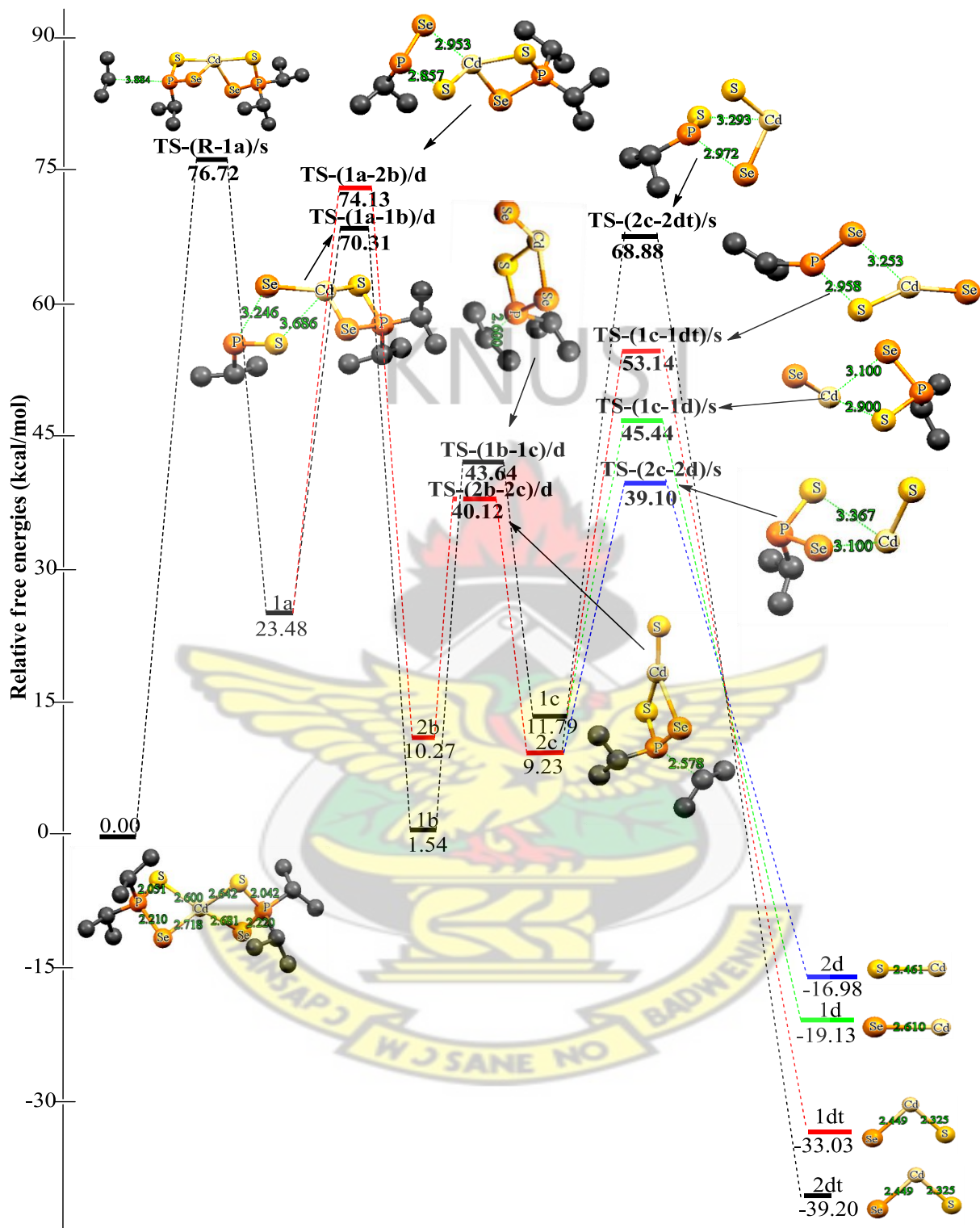


Figure 6.3: Energetics of the unimolecular decomposition pathway (1, 2) at 800 K. The relative free energies are in kcal/mol and bond distances in Å

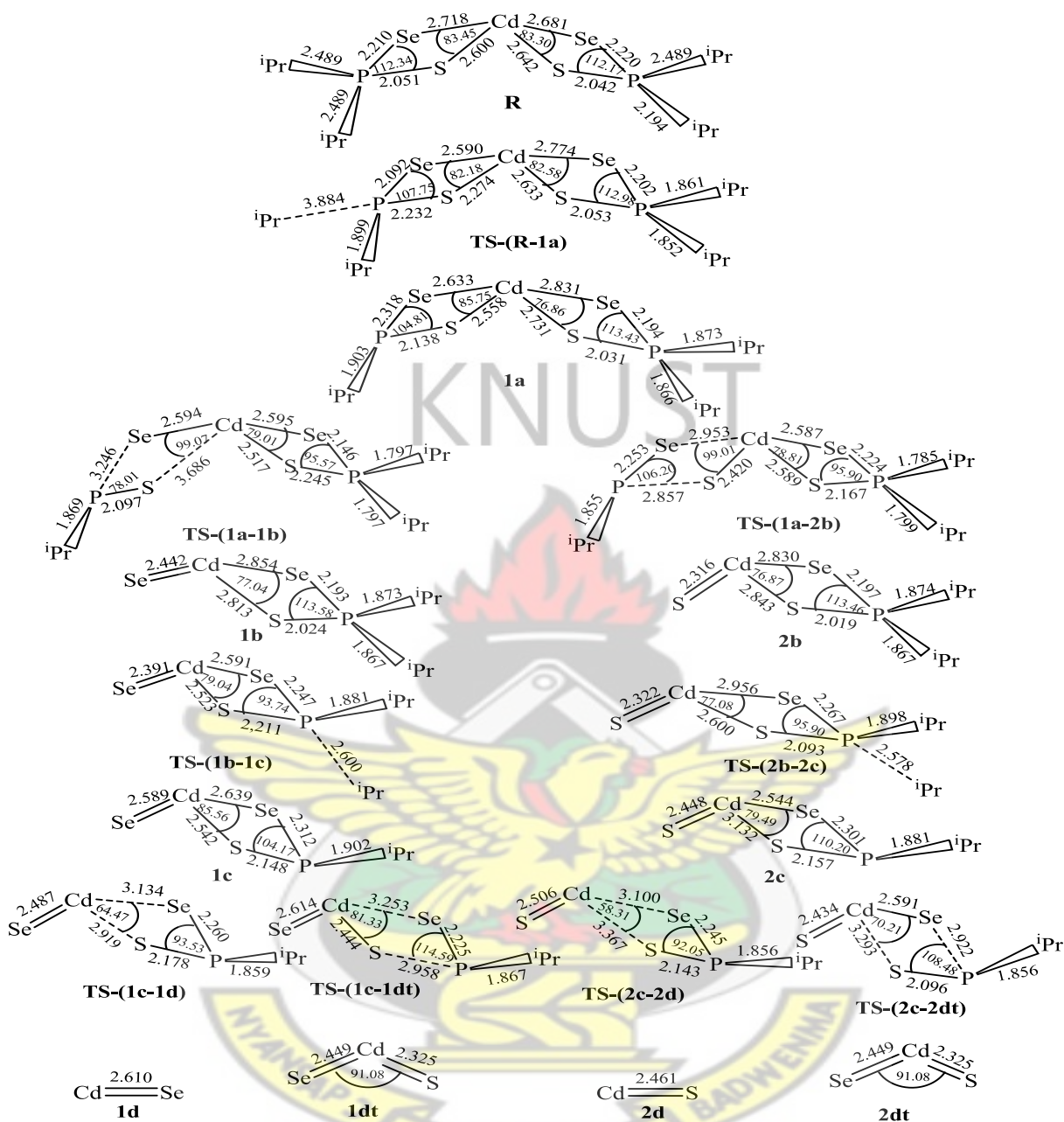


Figure 6.4: Optimized geometrical parameters of the main stationary points involved in the unimolecular decomposition pathway (1, 2). Bond distances in Å and bond angles in degrees

The reaction mechanisms involved in the decomposition of (*i*Pr)<sub>2</sub>PSSe-Cd intermediate were studied by considering the energetics of the reactants, intermediates and products (Scheme 6.2). The computed potential energy surface at 298.15 K and 800 K are given in Figures 6.5 and 6.6.

The initial decomposition of [Cd{(iPr)<sub>2</sub>PSSe}]<sub>2</sub> precursor was further explored by the abstraction of (iPr)<sub>2</sub>PSSe radical to form (iPr)<sub>2</sub>PSSe-Cd **3a** intermediate on the doublet PES. The decomposition of (iPr)<sub>2</sub>PSSe-Cd intermediate **3a** from the reactant **R** through transition state **TS-(R-3a)** has activation free energy barrier of +61.11 kcal/mol (298.15 K) and +61.23 kcal/mol (800 K) and reaction free energy of +53.61 kcal/mol (298.15 K) and +20.36 kcal/mol (800 K).

The (iPr)<sub>2</sub>PSSe-Cd **3a** intermediate decomposes through the transition state **TS-(3a-3b)** to form CdSe **3b** on the doublet PES. The activation barrier along this pathway was -5.66 kcal/mol (298.15 K) and +27.66 kcal/mol (800 K) with a reaction free energy of -38.28 kcal/mol (298.15 K) and -21.56 kcal/mol (800 K). The optimized geometry of **TS-(3a-3b)** further reveals the elongation of Cd-S bond length from 2.570 to 4.573 Å and P-Se bond length from 2.274 to 3.939 Å.

The formation of CdS **4b** through the transition state **TS-(3a-4b)** from (iPr)<sub>2</sub>PSSe-Cd **3a** intermediate has an activation free energy barrier of -3.22 kcal/mol (298.15 K) and +29.90 kcal/mol (800 K) and exergonic by 31.14 kcal/mol (298.15 K) and 14.85 kcal/mol (800 K) on the doublet PES. The optimized geometry of **TS-(3a-4b)** further reveals the elongation of Cd-Se bond length from 2.570 to 2.756 Å and P-S bond length from 2.089 to 2.648 Å.

The transition state energy involved in the decomposition of  $(^i\text{Pr})_2\text{PSSe-Cd}$  intermediate is lower than the free energy of the intermediate molecule. Thus the decomposition of  $(^i\text{Pr})_2\text{PSSe-Cd}$  intermediate leading to the formation of CdSe or CdS in the gas phase, is likely to occur without a barrier at  $T = 298.15 \text{ K}$ .

The Decomposition of  $(^i\text{Pr})_2\text{PSSe-Cd}$  intermediate was further explored to access the ternary nature of the intermediate on the doublet PES. The transition state **TS-(3a-3bt)** linking the  $(^i\text{Pr})_2\text{PSSe-Cd}$  intermediate **3a** to form ternary  $\text{CdSe}_x\text{S}_{1-x}$  **3bt** has an activation barrier of +13.20 kcal/mol (298.15 K) and +46.52 kcal/mol (800 K) and reaction free energy of -41.69 kcal/mol (298.15 K) and -34.27 kcal/mol (800 K). The optimized geometry of **TS-(3a-3bt)** further reveals the elongation of P-Se bond length from 2.274 to 3.673 Å and P-S bond length from 2.089 to 3.963 Å.

Kinetically the most favourable pathway is the [3b] elimination route to form CdSe. The barrier along this pathway is 27.66 kcal/mol lower than the barrier along the [4b] elimination route (29.90 kcal/mol) and the [3bt] elimination route (46.52 kcal/mol). The unimolecular and bimolecular recombination rate constants along the 3b pathway were calculated as  $1.26 \times 10^5 \text{ s}^{-1}$  and  $9.55 \times 10^{11} \text{ s}^{-1}$  at  $T = 800 \text{ K}$  respectively. The ternary  $\text{CdSe}_x\text{S}_{1-x}$  formed from optimization of the  $(^i\text{Pr})_2\text{PSSe-Cd}$  intermediate is the most stable species on the reaction PES (34.27 kcal/mol exergonic).

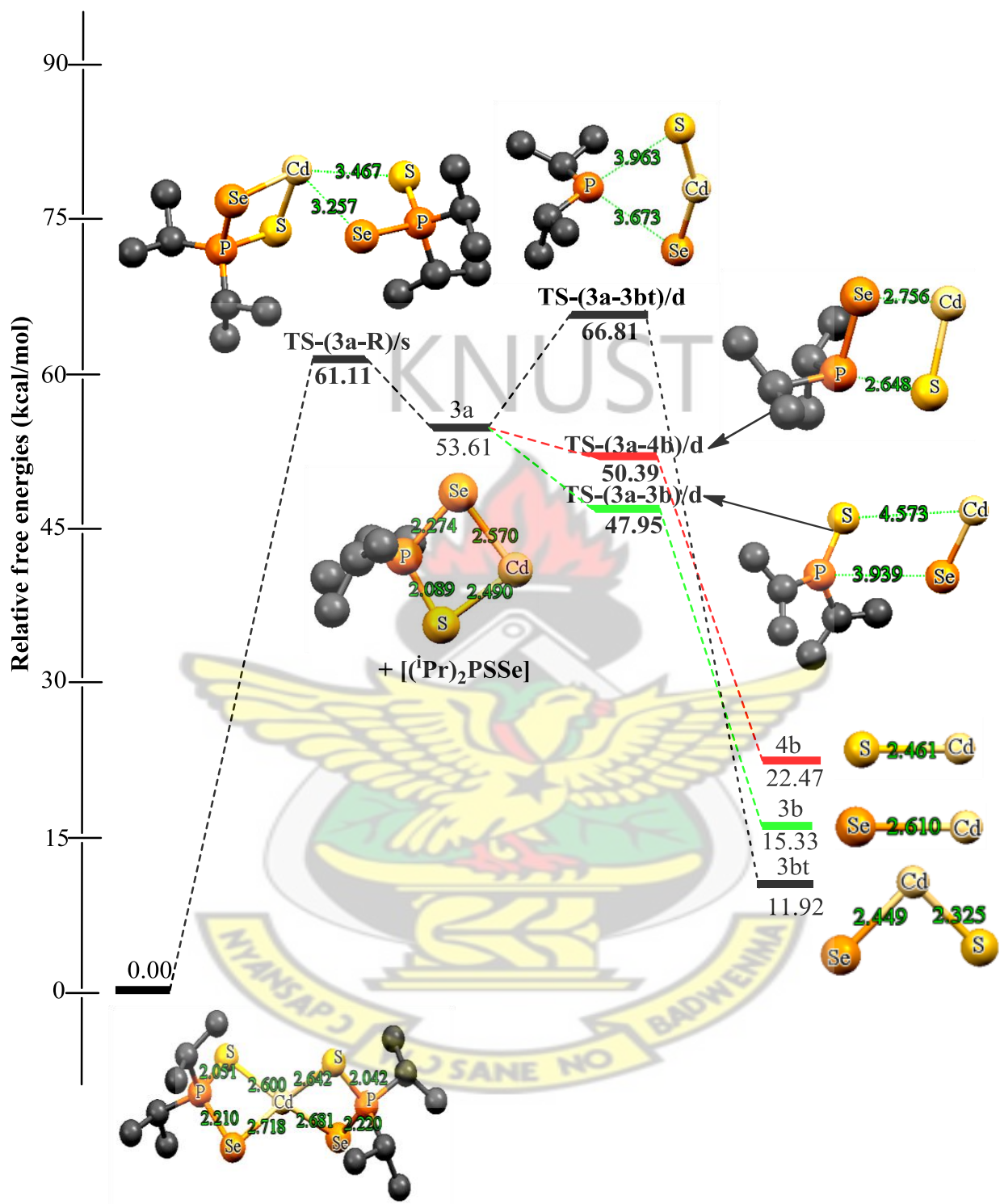


Figure 6.5: Energetics of the unimolecular decomposition pathway (3, 4) at 298.15 K. The relative free energies are in kcal/mol and bond distances in Å

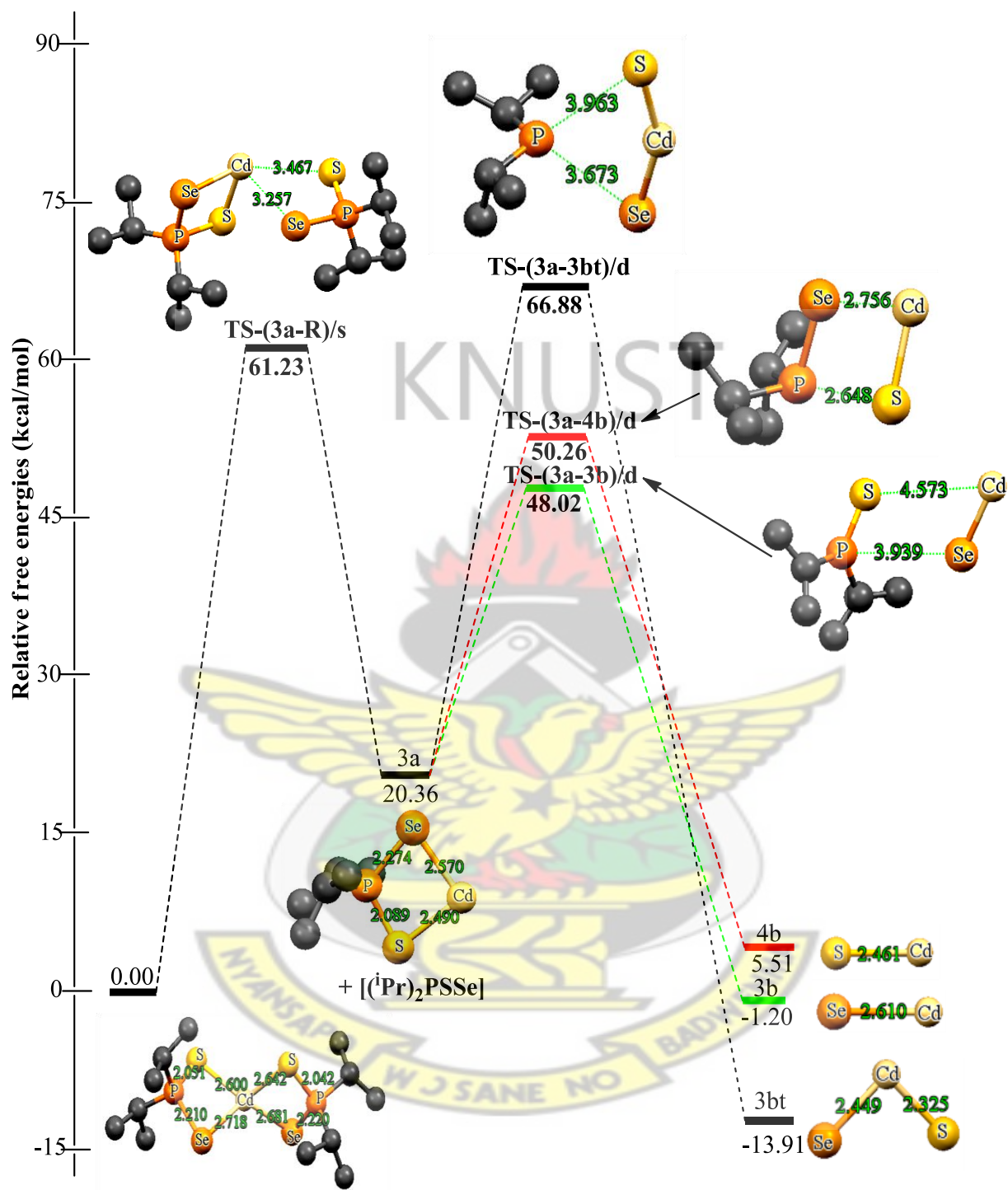


Figure 6.6: Energetics of the unimolecular decomposition pathway (3, 4) at 800 K. The relative free energies are in kcal/mol and bond distances in Å

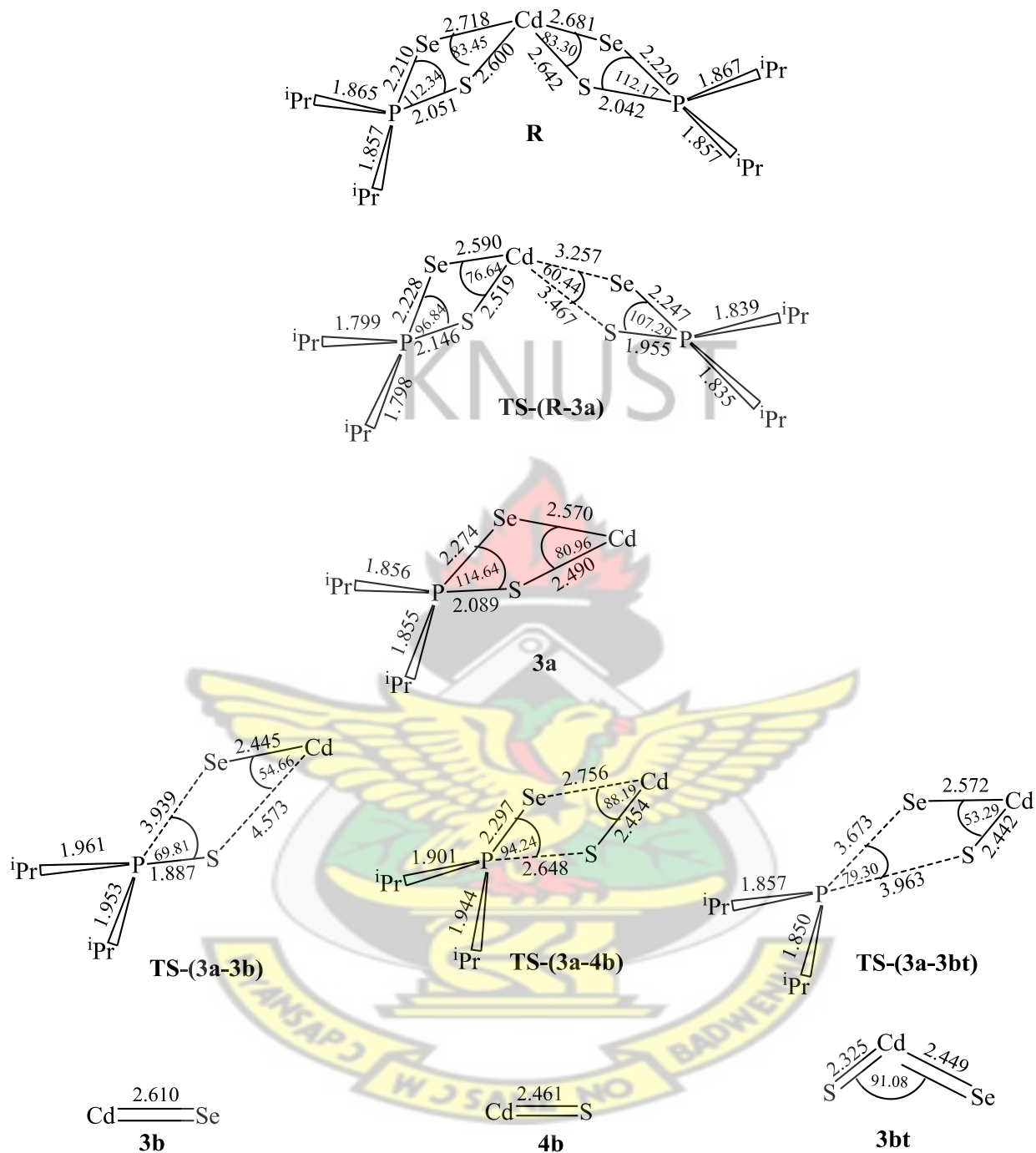


Figure 6.7: Optimized geometrical parameters of the main stationary points involved in the unimolecular decomposition pathway (3, 4). Bond distances in Å and bond angles in degrees

The reaction mechanisms involved in the decomposition of (<sup>i</sup>Pr)PSSe-Cd intermediate were studied by considering the energetics of reactants, intermediates and products (Scheme 6.3). The computed potential energy surfaces at 298.15 K and 800 K are shown in Figures 6.8 and 6.9.

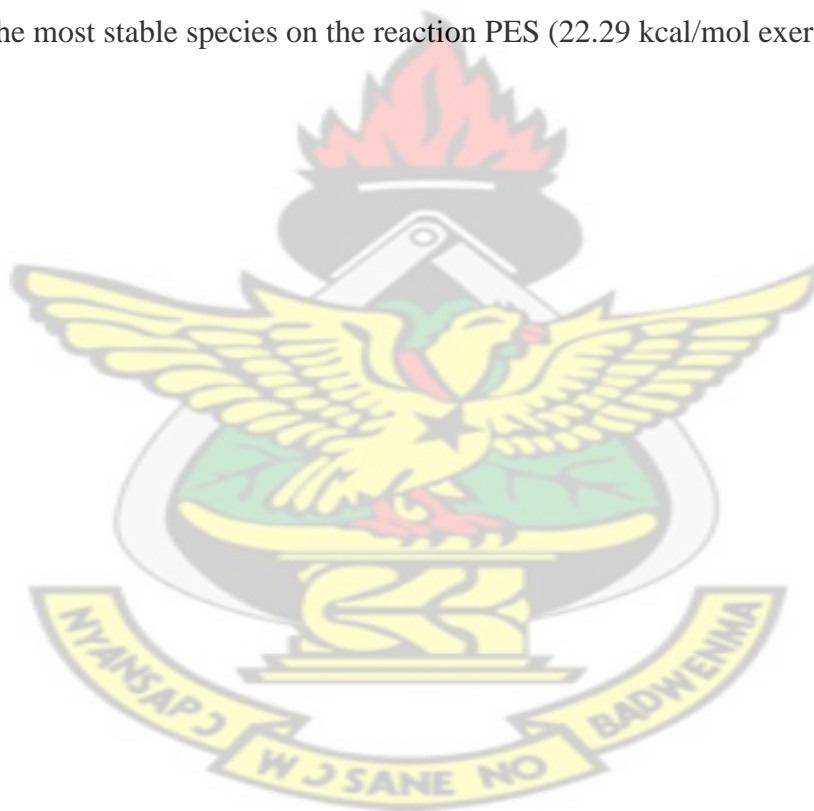
The activation free energy barrier involved in the formation of (<sup>i</sup>Pr)PSSe-Cd **5b** intermediate through a transition state **TS-(3a-5b)** was +7.60 kcal/mol (298.15 K) and +41.12 kcal/mol (800 K) with a reaction free energy of -34.70 kcal/mol (298.15 K) and -10.03 kcal/mol (800 K) on the singlet PES. The (<sup>i</sup>Pr)PSSe-Cd intermediate **5b** decompose through transition state **TS-(5b-5c)** to form CdSe **5c** on the singlet PES. The activation free energy barrier involved in the formation of CdSe **5c** was +4.03 kcal/mol (298.15 K) and +12.83 kcal/mol (800 K) with a reaction free energy of -15.94 kcal/mol (298.15 K) and -22.29 kcal/mol (800 K). The optimized geometrical structure of **TS-(5b-5c)** further reveals the elongation of Cd-S bond length from 2.527 to 3.880 Å and P-Se bond length from 2.262 to 2.950 Å.

The formation of CdS **6c** from the intermediate **5b** through the transition state **TS-(3a-6c)** has been found to have an activation free energy barrier of +26.24 kcal/mol (298.15 K) and +34.94 kcal/mol (800 K), and reaction free energy of -6.94 kcal/mol (298.15 K) and -13.97 kcal/mol (800 K) on the singlet PES. The optimized geometrical structure of **TS-(5b-6c)** reveals the elongation of Cd-Se bond length from 2.622 to 2.886 Å and P-S bond length from 2.099 to 2.831 Å.

The formation of ternary CdSe<sub>x</sub>S<sub>1-x</sub> **5ct** was located on the singlet PES and found to have an activation free energy barrier of +11.90 kcal/mol (298.15 K) and +20.94 kcal/mol (800 K) and exergonic by 7.28 kcal/mol (298.15 K) and 14.84 kcal/mol (800 K). The optimized geometry of

**TS-(5b-5ct)** further reveals the elongation of P-Se bond length from 2.262 to 2.920 Å and P-S bond length from 2.099 to 2.780 Å.

The kinetic parameters revealed that the activation barrier involved in the formation of ternary  $\text{CdSe}_x\text{S}_{1-x}$  [5ct] was higher than CdSe [5c] and CdS [6c]. The activation barrier revealed that CdSe dissociation pathway was kinetically more favourable than the other pathway with unimolecular and recombination rate constants of  $7.86 \times 10^6 \text{ s}^{-1}$  and  $1.59 \times 10^{10} \text{ s}^{-1}$  at  $T = 800 \text{ K}$  respectively. Thermodynamically, the CdSe [5c] formed from optimization of the  ${}^i\text{PrPSSe-Cd}$  intermediate is the most stable species on the reaction PES (22.29 kcal/mol exergonic).



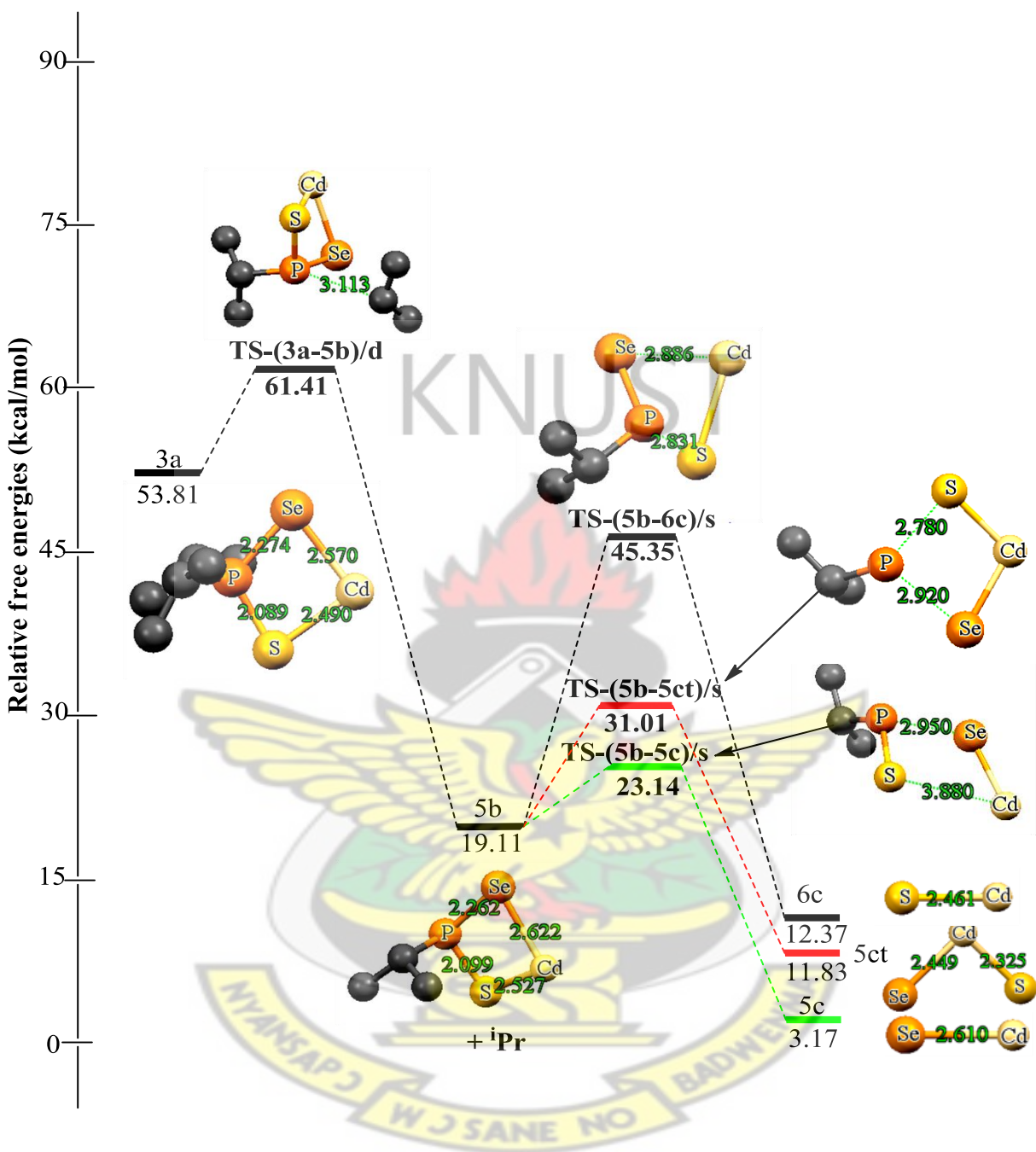


Figure 6.8: Energetics of the unimolecular decomposition pathway (5, 6) at 298.15 K. The relative free energies are in kcal/mol and bond distances in Å

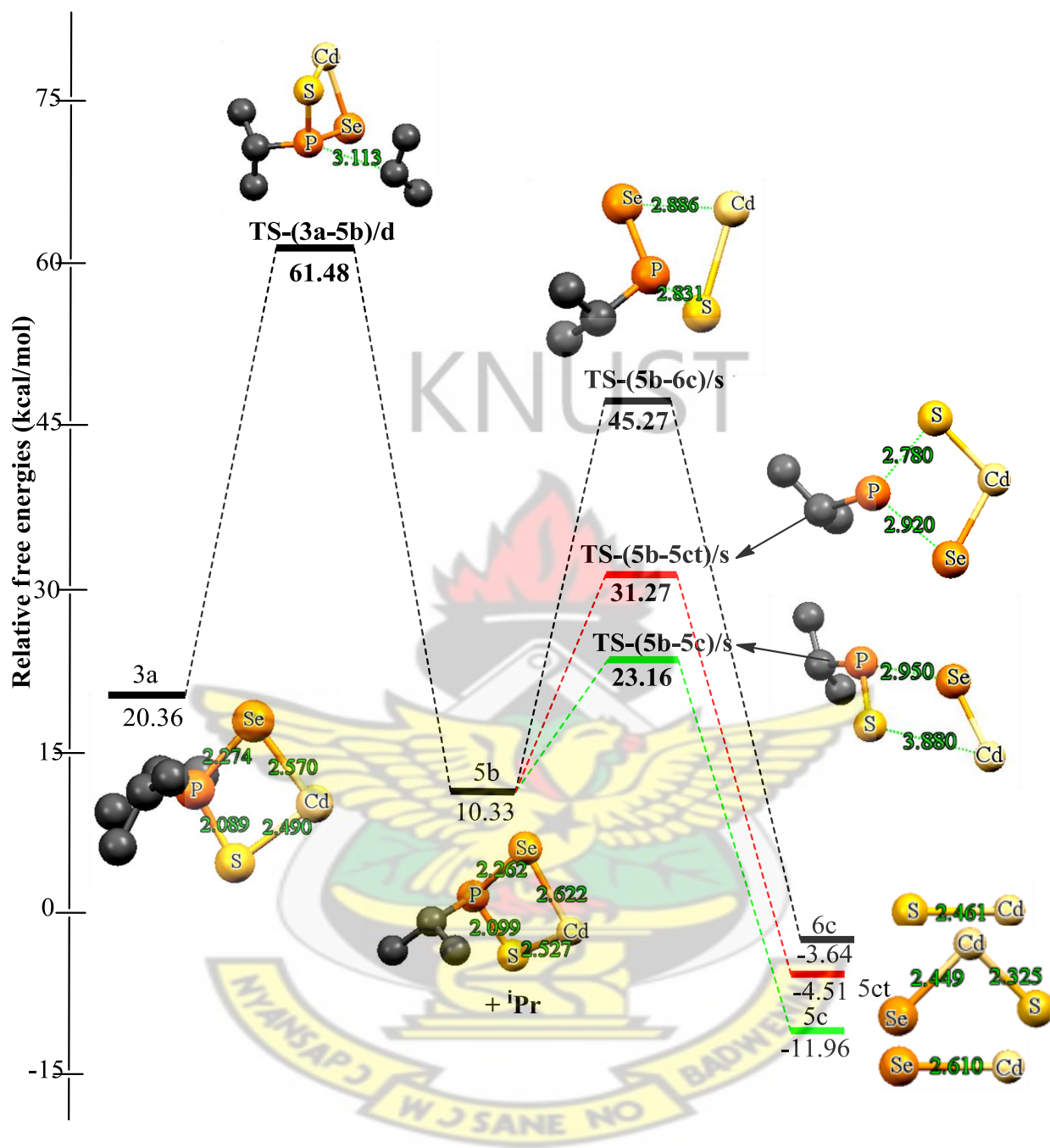


Figure 6.9: Energetics of the unimolecular decomposition pathway (5, 6) at 800 K. The relative free energies are in kcal/mol and bond distances in Å

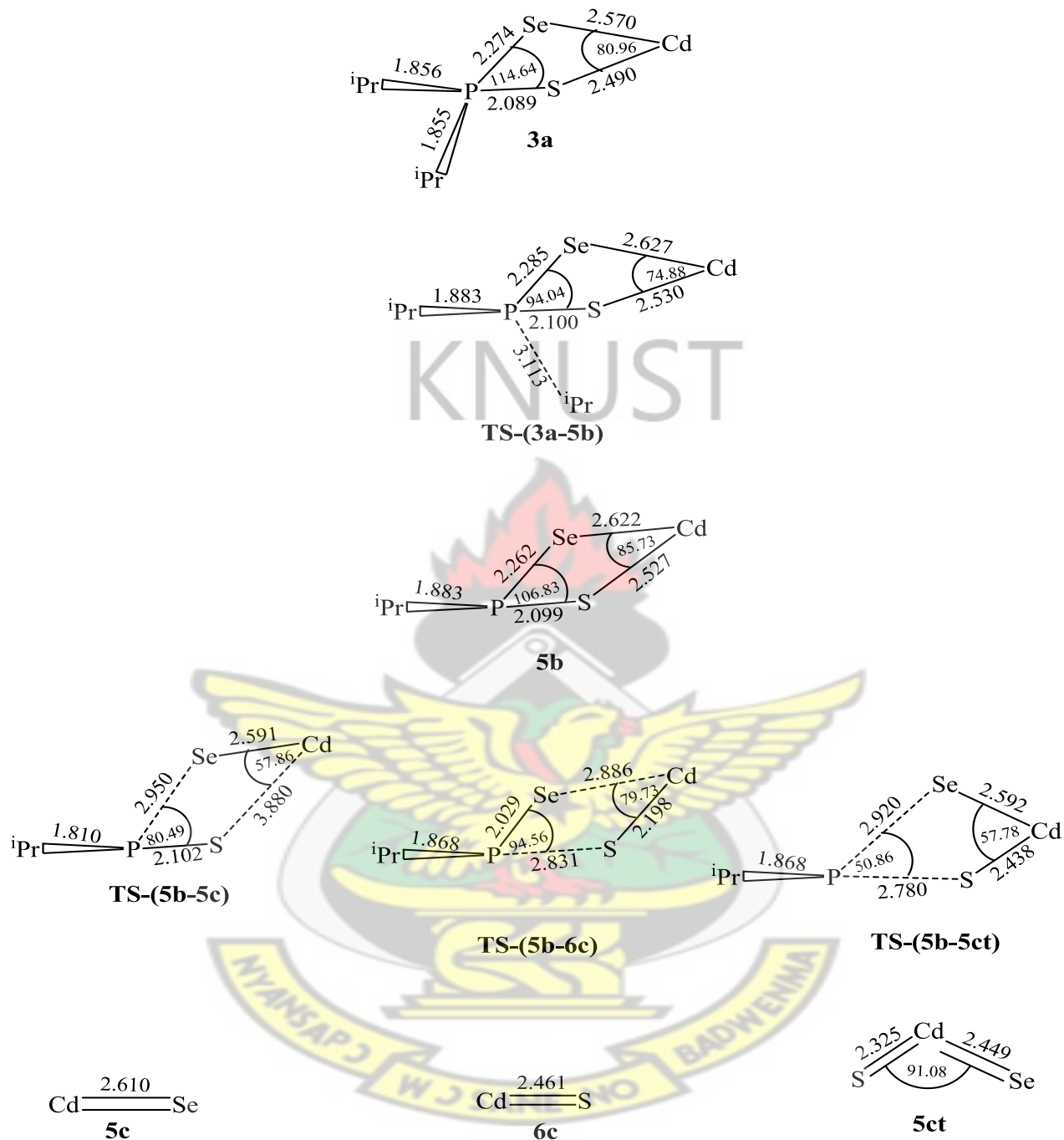


Figure 6.10: Optimized geometrical parameters of the main stationary points involved in the unimolecular decomposition pathway (3, 4). Bond distances in Å and bond angles in degrees

Table 6.2: Calculated rate constants for selected individual steps in the decomposition of Cd[(<sup>i</sup>Pr)<sub>2</sub>PSSe]<sub>2</sub> precursor at room temperature (298.15 K) and at an elevated temperature (800 K)

Reaction	k <sub>uni</sub> (s <sup>-1</sup> )		k <sub>eq</sub>		k <sub>rec</sub> (s <sup>-1</sup> )	
	298.15 K	800 K	298.15 K	800 K	298.15 K	800 K
1c → 1d	2.94 x 10 <sup>-21</sup>	6.44 x 10 <sup>1</sup>	1.09 x 10 <sup>2</sup>	1.05 x 10 <sup>14</sup>	3.20 x 10 <sup>-19</sup>	6.76 x 10 <sup>15</sup>
2c → 2d	1.74 x 10 <sup>-16</sup>	3.47x 10 <sup>2</sup>	2.57 x 10 <sup>5</sup>	2.80 x 10 <sup>12</sup>	4.47 x 10 <sup>-11</sup>	9.72 x 10 <sup>14</sup>
1c → 1dt	7.77 x 10 <sup>-27</sup>	5.07 x 10 <sup>-2</sup>	2.32 x 10 <sup>5</sup>	1.63 x 10 <sup>24</sup>	1.80 x 10 <sup>-21</sup>	8.26 x 10 <sup>22</sup>
2c → 2dt	3.37 x 10 <sup>-38</sup>	2.54 x 10 <sup>-6</sup>	3.04 x 10 <sup>10</sup>	5.44 x 10 <sup>28</sup>	1.02 x 10 <sup>-27</sup>	1.38 x 10 <sup>23</sup>
3a → 3b	4.48 x 10 <sup>-23</sup>	1.26 x 10 <sup>5</sup>	5.79 x 10 <sup>-12</sup>	7.58 x 10 <sup>6</sup>	2.59 x 10 <sup>-34</sup>	9.55 x 10 <sup>11</sup>
3a → 4b	7.16 x 10 <sup>-25</sup>	3.10 x 10 <sup>-1</sup>	3.38 x 10 <sup>-17</sup>	9.14 x 10 <sup>-5</sup>	2.42 x 10 <sup>-41</sup>	2.83 x 10 <sup>-5</sup>
3a → 3bt	6.58 x 10 <sup>-37</sup>	8.94 x 10 <sup>-6</sup>	1.83 x 10 <sup>-9</sup>	1.57 x 10 <sup>10</sup>	1.20 x 10 <sup>-45</sup>	1.40 x 10 <sup>5</sup>
5b → 5c	6.77 x 10 <sup>-5</sup>	7.86 x 10 <sup>6</sup>	4.75 x 10 <sup>-3</sup>	2.02 x 10 <sup>3</sup>	3.22 x 10 <sup>-07</sup>	1.59 x 10 <sup>10</sup>
5b → 6c	3.54 x 10 <sup>-21</sup>	7.16 x 10 <sup>6</sup>	8.56 x 10 <sup>-10</sup>	4.65 x 10 <sup>2</sup>	3.03 x 10 <sup>-30</sup>	3.33 x 10 <sup>9</sup>
5b → 5ct	1.15 x 10 <sup>-10</sup>	4.78 x 10 <sup>5</sup>	2.13 x 10 <sup>-09</sup>	5.85 x 10 <sup>2</sup>	2.45 x 10 <sup>-19</sup>	2.80 x 10 <sup>8</sup>

The values of  $n_T$  for the thermal decomposition of [Cd{(<sup>i</sup>Pr)<sub>2</sub>PSSe}<sub>2</sub>] precursor is shown in Table 6.3. In fact, the similarity between the reactants, intermediates, and products increases with respect to the reaction in the order of 4b > 5ct > 3b > 6c > 3bt > 5c > 2d > 1d > 1dt > 2dt, and 4b > 3b > 6c > 5c-3bt > 5ct-1d-2d > 2dt-1dt at T = 298.15 K and 800 K respectively. These results imply that the transition structures involved in the formation of CdSe **4b** has a larger similarity to the product than the other reactions pathway at both temperatures.

Table 6.3: Position of the transition structures ( $n_T$ ) for selected individual steps

Reaction pathway	298.15 K	800 K
1c → 1d	0.485165	0.413053
2c → 2d	0.496431	0.410801
1c → 1dt	0.467742	0.381451
2c → 2dt	0.452787	0.389241
3a → 3b	0.595158	0.493831
3a → 4b	0.643468	0.528997
3a → 3bt	0.548973	0.452902
5b → 5c	0.536766	0.455636
5b → 6c	0.578961	0.480675
5b → 5ct	0.617852	0.419732

## 6.5 Conclusion

The kinetics and thermodynamics of  $\text{Cd}[(^i\text{Pr})_2\text{PSSe}]_2$  precursor was studied in the gas phase by DFT calculation at the MO6/LACVP\* level of theory. Several possible pathways involved in the thermal decomposition of the precursor have been examined, both at room temperature and elevated temperature. The following conclusions are drawn from the results presented.

1. On the singlet PES, the decomposition of  $(^i\text{Pr})\text{PSSe-Cd-S}$  intermediate leading to the formation of ternary  $\text{CdSe}_x\text{S}_{1-x}$  was thermodynamically favoured, but the reaction is

kinetically blocked by the highest activation barrier. The unimolecular and bimolecular recombination rate constants were calculated as  $2.54 \times 10^{-6} \text{ s}^{-1}$  and  $1.38 \times 10^{23} \text{ s}^{-1}$  at  $T = 800 \text{ K}$  respectively.

2. The calculation indicate that on the singlet PES, the decomposition of  $(^1\text{Pr})\text{PSSe-Cd}$  intermediate leading to CdSe formation, is observed as the most probable decomposition mechanism. The unimolecular and bimolecular recombination rate constants were calculated as  $7.86 \times 10^6 \text{ s}^{-1}$  and  $1.59 \times 10^{10} \text{ s}^{-1}$  at  $T = 800 \text{ K}$  respectively.
3. On the doublet PES, the decomposition of  $(^1\text{Pr})_2\text{PSSe-Cd}$  intermediate leading to the formation of ternary  $\text{CdSe}_x\text{S}_{1-x}$  was thermodynamically favoured, but the reaction is kinetically blocked by the highest activation barrier. However, the pathway leading to formation of CdSe is proposed as the most plausible decomposition pathway. The unimolecular and bimolecular recombination rate constants were calculated as  $1.26 \times 10^5 \text{ s}^{-1}$  and  $9.55 \times 10^{11} \text{ s}^{-1}$  at  $T = 800 \text{ K}$  respectively.
4. The value of  $n_T$  for the decomposition of  $(^1\text{Pr})_2\text{PSSe-Cd}$  reveals that the transition state structure involved in the formation of CdS has a larger similarity to the product than the other reactions pathway at  $T = 800 \text{ K}$ .

## References

- Afzaal, M., Aucott, S. M, Crouch, D., O'Brien, P., Woollins, J. D. and Park, J.-H. (2002). Deposition of MSe (M = Cd, Zn) Films by LP-MOCVD from Novel Single-Source Precursors  $M[(\text{SePPh}_2)_2\text{N}]_2$ . *Chem. Vap. Deposition*, 8: 187-189.
- Akhtar, J., Afzaal, M., Vincent, M., Burton, N., Raftery, J., Hillier, I. and O'Brien, P. (2011). "Understanding the Decomposition Pathways of Mixed Sulphur/Selenium Lead Phosphinato Precursor Explaining the Formation of Lead Selenide". *J. Phys. Chem. C.*, 115(34): 16904-16909.
- Bhattacharyya, P., Novosad, J., Phillips, J., Slawin, A. M. Z., Williams, D. J. and Woollins, J. D. (1995). Bis(bidentate) Complexes of Imidobis(diphenylphosphinochalcogenides)  $[M\{N(XPPh_2)_2 - X, X'\}_2]$  (X = S or Se; M = Ni, Pd or Pt). *Dalton Trans.*, 10: 1607-1613.
- Bruchez, M., Moronne, M., Gin, P., Weiss, S. and Alivisatos, A. P. (1998). "Quantum Dot Cell Labeling". *Science*, 281: 2013-2016.
- Gleizes, A. N. (2000). "MOCVD of chalcogenides, pnictides, and heterometallic compounds from single- source molecule precursors". *Chem. Vap. Deposition*, 6: 155-173.
- Green, M., Wakefield, G. and Dobson, P. J. (2003). "A simple metalorganic route to organically passivated mercury telluride nanocrystals". *J. Mater. Chem.*, 13: 1076-1078.

- Kim, S., B. Fisher, H.-J. Eisler and Bawendi, M. (2003). "Type-II quantum dots: CdTe/CdSe(core/shell) and CdSe/ZnTe(core/shell) heterostructures". *J. Am. Chem. Soc.*, 125: 11466-11667.
- Ma, R. M., Wei, X. L., Dai, L., Huo, H. B. and Qin, G. G. (2007). "Synthesis of CdS nanowire networks and their optical and electrical properties". *Nanotechnology*, 18: 1–5.
- Mahtab, R., Rogers, J. P. and Murphy, C. J. (1995). "Protein-Sized quantum dot luminescence can distinguish between 'Straight', 'Bent', and 'Kinked' oligonucleotides". *J. Am. Chem. Soc.*, 117: 9099-9100.
- Mahtab, R., Rogers, J. P., Singleton, C. P. and Murphy, C. J. (1996). "Preferential adsorption of a 'Kinked' DNA to a neutral curved surface: comparisons to and implications for Nonspecific DNA-Protein interactions". *J. Am. Chem. Soc.*, 118: 7028–7032.
- Tan, L., Liu, L., Xie, Q., Zhang, Y. and Yao, S. (2004). "Fluorescence quenching of bovine serum albumin in reversed micelles by CdS nanoparticles". *Anal. Sci.*, 20: 441-444.
- Xia, Y., Yang, P., Sun, Y., Wu, Y., Mayers, B., Gates, B., Yin, Y., Kim, F. and Yan, H. (2003). "One-Dimensional Nanostructures: Synthesis, Characterization and Applications". *Adv. Mater.*, 15: 353-38.

## CHAPTER SEVEN

### 7. Conclusion and Recommendation

The conclusions drawn from the thermal decomposition of some single-source precursors to deposit Lead, Zinc and cadmium chalcogenide thin films using DFT study have been described in section 7.1

#### 7.1 Conclusion

Density functional study of the decomposition mechanisms of  $\text{Pb}[(\text{C}_6\text{H}_5)_2\text{PSSe}]_2$ ,  $\text{Pb}[(^i\text{Pr})_2\text{PSSe}]_2$ ,  $\text{Zn}[(^i\text{Pr})_2\text{PSSe}]_2$  and  $\text{Cd}[(^i\text{Pr})_2\text{PSSe}]_2$  single-source precursors for the chemical vapour deposition at both room temperature (298.15 K) and elevated temperature (800 K) lead to the following conclusions.

1. In the computational investigation involved in the decomposition of all the single-source precursors, it was found that the formation of metal chalcogenides in CVD may involve more than one mechanism.
2. In the decomposition of  $\text{Pb}[(\text{C}_6\text{H}_5)_2\text{PSSe}]_2$  system, it was found that the steps that lead to PbSe formation are somewhat more favourable on both thermodynamic and kinetic grounds, than those that lead to PbS and ternary  $\text{PbSe}_x\text{S}_{1-x}$  formation on the singlet potential energy surface, PES. On the doublet PES, the steps that lead to PbSe formation are somewhat more favourable on kinetic grounds while the steps that lead to ternary  $\text{PbSe}_x\text{S}_{1-x}$  formation are somewhat more favourable on thermodynamic grounds.
3. In the decomposition of  $\text{Pb}[(^i\text{Pr})_2\text{PSSe}]_2$  system, it was found that the steps that lead to PbS formation are more favourable on kinetic grounds, than those that lead to PbSe and ternary

$\text{PbSe}_x\text{S}_{1-x}$  formation on both the singlet and the doublet potential energy surface. Thermodynamically, the steps that lead to PbSe formation are more favourable than those that lead to PbS and ternary  $\text{PbSe}_x\text{S}_{1-x}$  formation on the singlet PES, while those that lead to  $\text{PbSe}_x\text{S}_{1-x}$  formation are more favourable than those that lead to PbSe and PbS formation on the doublet PES.

4. In the decomposition of  $\text{Zn}[(^i\text{Pr})_2\text{PSSe}]_2$  system, it was found that on the singlet PES the steps that lead to ZnS formation are more favourable on kinetic grounds, than those that lead to ZnSe and ternary  $\text{ZnSe}_x\text{S}_{1-x}$  formation and on the doublet PES, the steps that lead to ZnSe formation are more favourable on kinetic grounds than those that lead to ZnS and ternary  $\text{ZnSe}_x\text{S}_{1-x}$  formation. Thermodynamically, the steps that lead to ternary  $\text{ZnSe}_x\text{S}_{1-x}$  formation are more favourable than those that lead to ZnSe and ZnS formation on both the singlet and the doublet PES.
5. In the decomposition of  $\text{Cd}[(^i\text{Pr})_2\text{PSSe}]_2$  system, it was found that the steps that lead to CdSe formation are more favourable on kinetic grounds, than those that lead to CdS and  $\text{CdSe}_x\text{S}_{1-x}$  formation on both the singlet and the doublet PES. Thermodynamically, the steps that lead to  $\text{CdSe}_x\text{S}_{1-x}$  formation are more favourable than those that lead to CdSe and CdS formation on both the singlet and the doublet PES.

## 7.2 Recommendation

The NBO charges, bond indexes, and synchronicity parameters may also be investigated to access the molecular mechanism of chemical reaction involve in the decomposition process of single-source precursors.

Atomic properties such solvation may also be investigated on the PES for the reaction to determine whether there will be any significant change in the energetics of the reaction involved in the chemical bath deposition process.

